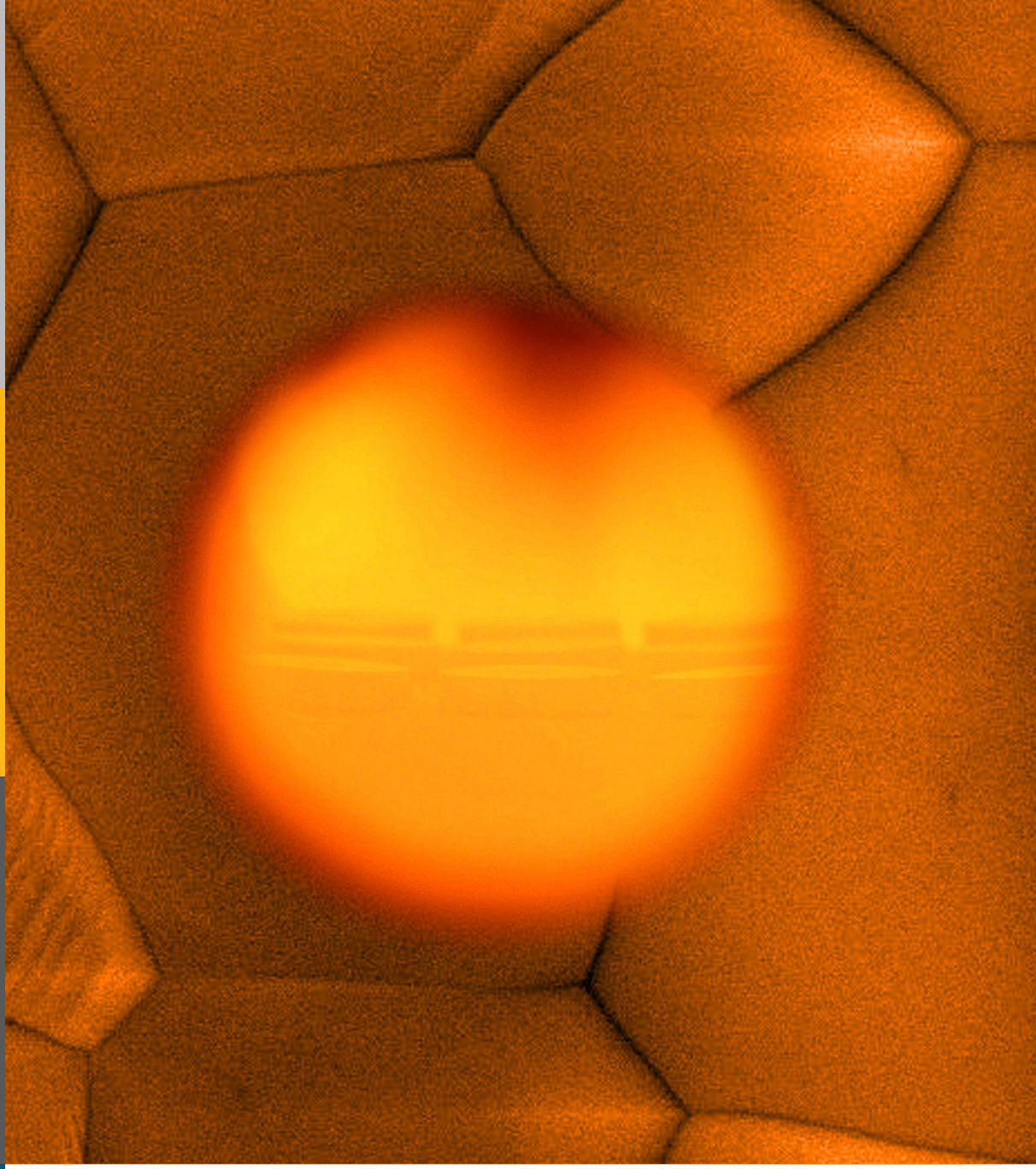

Monazite-type Ceramics for Conditioning of Minor Actinides: Structural Characterization and Properties

Carole Babelot

JÜLICH
FORSCHUNGSZENTRUM

Member of the Helmholtz Association

Monazite-type Ceramics for Conditioning of Minor Actinides: Structural Characterization and Properties

Von der Fakultät für Georessourcen und Materialtechnik der
Rheinisch -Westfälischen Technischen Hochschule Aachen

zur Erlangung des akademischen Grades einer

Doktorin der Ingenieurwissenschaften
genehmigte Dissertation

vorgelegt von

Dipl.-Ing. Carole Babelot

aus Karlsruhe

Berichter: Univ.-Prof. Dr. rer. nat. Dirk Bosbach
Univ.-Prof. Dr. rer. nat. Rainer Telle

Tag der mündlichen Prüfung: 19.11.2012

Forschungszentrum Jülich GmbH
Institut für Energie- und Klimaforschung (IEK)
Nukleare Entsorgung und Reaktorsicherheit (IEK-6)

Monazite-type Ceramics for Conditioning of Minor Actinides: Structural Characterization and Properties

Carole Babelot

Schriften des Forschungszentrums Jülich
Reihe Energie & Umwelt / Energy & Environment Band / Volume 182

ISSN 1866-1793 ISBN 978-3-89336-889-1

Bibliographic information published by the Deutsche Nationalbibliothek.
The Deutsche Nationalbibliothek lists this publication in the Deutsche Nationalbibliografie; detailed bibliographic data are available in the Internet at http://dnb.d-nb.de.

Publisher and Distributor: Forschungszentrum Jülich GmbH
Zentralbibliothek
52425 Jülich
Tel: +49 2461 61-5368
Fax: +49 2461 61-6103
Email: zb-publikation@fz-juelich.de
www.fz-juelich.de/zb

Cover Design: Grafische Medien, Forschungszentrum Jülich GmbH

Printer: Grafische Medien, Forschungszentrum Jülich GmbH

Schriften des Forschungszentrums Jülich
Reihe Energie & Umwelt / Energy & Environment, Band / Volume 182

D 82 (Diss., RWTH Aachen, University, 2012)

ISSN 1866-1793
ISBN 978-3-89336-889-1

À tous ceux qui m'ont aidée au cours de mes études supérieures,
de Strasbourg à Jülich, en passant par Limoges.

« Je sers la science et c’est ma joie. »

Basile, disciple de Léonard.

Content

Table of figures

Abbreviations

a	lattice parameter *a*
An	actinides
ANKA	Angströmquelle Karlsruhe
a.u.	arbritary unit
b	lattice parameter *b*
β	angle $\neq 90°$ in the monoclinic system
BET	Brunauer Emmett Teller: method of specific surface area measurement
c	lattice parameter *c*
c_l	average length of cracks
$\chi(k)$	EXAFS equation
CN	Coordination Number
d	days
D	diameter
d_c	average length of the diagonals of the Vickers indents
DSC	Differential Scanning Calorimetry
E	Young's modulus
EDX	Energy-Dispersive X-ray
ESRF	European Synchrotron Radiation Facility
EXAFS	Extended X-ray Absorption Fine Structure
F	load
FP	Fission Products
FT	Fourier Transformation
h	height
HAW	High Active Waste
HLLW	High Level Liquid Waste
ICP-MS	Inductively Coupled Plasma-Mass Spectrometry
IEK-6	Institut für Energie- und Klimaforschung, Nukleare Entsorgung und Reaktorsicherheit, within the Forschungszentrum Jülich GmbH
ISC	intersystem crossing

k	wave vector
KIT-INE	Institute for Nuclear Waste Disposal (INE) within the Karlsruhe Institute of Technology (KIT)
λ	wavelength
L	mean nanocrystallite size
Ln	lanthanides
LWR	Light Water Reactor
m	mass
MA	Minor Actinides (Np, Am, Cm)
NEA	Nuclear Energy Agency
N_L	normalized weight loss
MCC	Materials Characterization Centre
P	pressure
P&C	Partitioning and Conditioning
PGI-9	Peter Grünberg Institut, Halbleiter-Nanoelektronik, within the Forschungszentrum Jülich GmbH
P_{opt}	optimal pressure
P&T	Partitioning and Transmutation
PWR	Pressurized Water Reactor
ρ_g	green density
ρ_{H2O}	density of water
ρ_p	density of the paraffin
ρ_s	sintered density
r_{At}	atomic radius
R_L	normalized dissolution rate
RE	Rare Earths
RT	Room Temperature
SEM	Scanning Electron Microscope
t	time
T	temperature
T_1 to T_5	temperature of the thermal treatment of La-monazite powder

TG	thermogravimetry
T_c	critical amorphization temperature
T_m	melting point
TRLFS	Time Resolved Laser Fluorescence Spectroscopy
V	volume
XRD	X-Ray Diffraction
Z	atomic number

1. Introduction

In 2011 the world population reached seven billions of humans compared to only one billion in 1800, which corresponds to a 600 % increase within approx. 200 years. This development has an impact on the consumption of energy. Figure 1 shows the energy consumption per year from 1850 to 2000 worldwide in EJ (1 EJ = 10^{18} J) [1]. The energy consumption grew from 25 EJ in 1850 up to 450 EJ in 2000. The worldwide population needs more and more energy.

Over the years, the energy sources varied from gas, oil, coal, nuclear, hydraulic to biomass. However, the following questions are still in the discussion:

- Which energy source is safe? Which one has the best efficiency?
- What are the impacts of the energy sources on the environment?
- What are the impacts of the energy sources with regard to the waste problem?

Energy sources do not only have to be safe and efficient; they also have to be accepted by the citizens. During the first decade of the 21st century, the CO_2 emissions to the atmosphere and their impact on the global warming have increasingly been on the news. These concerns led to the growing consumption of energy sources other than fossil fuels. In this framework, the use of nuclear energy could be perceived as an important climate change mitigation option. The catastrophe at the Fukushima Daiichi nuclear power station on March 11, 2011 had impacts on the perception of nuclear energy and intensified the discussion on the nuclear safety.

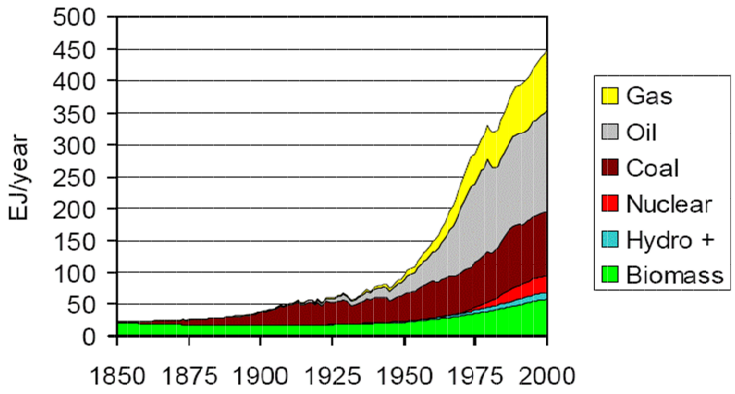

Figure 1: Energy consumption worldwide in EJ per year, from 1850 to 2000 [1].

1. Introduction

The nuclear safety plays an important role in political discussions. The nuclear waste issue can be divided in two main topics: the safety of nuclear power plant and the safe disposal of nuclear waste. The first issue concerns the countries that are currently producing nuclear energy. The second issue concerns the countries which have once made the choice to use nuclear energy. As the radiotoxicity of High Active Waste (HAW) needs about one million years to degenerate, the future generations will also have to deal with the nuclear waste issue.

However, if the minor actinides (MA) are removed from the HAW by partitioning and converted into the shorter-lived or stable elements by transmutation, the final waste loses most of its long-term radiotoxicity. Thus, partitioning and transmutation (P&T strategy) are considered as the attractive options for reducing the burden on deep underground repositories. In addition, these separated MA can also be conditioned (P&C strategy) in specifically adapted ceramics to ensure their safe final disposal over geological times. The highly active liquid waste produced during the reprocessing must be conditioned industrially by using a vitrification process before the final disposal. Although the widely used borosilicate glasses meet the specifications needed, more stable waste forms could considerably improve the long-term safety of nuclear disposal. In the last decades, the focus of the research was directed at the study of the ceramic waste forms. These forms seem to be promising materials in particular for the conditioning of MA which dominate the long-term radiotoxicity of the spent nuclear fuel [2-4].

Waste management in the European countries

The policies introduced by European countries are summarized in Table 1. At the moment the nuclear spent fuels are foreseen either for the direct disposal in deep underground repositories or for reprocessing.

Table 1: Waste management for used fuel and HLW from nuclear power reactors in Europe [5].

Country	Policy	Facilities and progress towards final repositories
Belgium	Reprocessing	Central waste storage at Dessel
		Underground laboratory established 1984 at Mol
		Construction of repository to begin about 2035
Finland	Direct disposal	Program start 1983, two used fuel storages in operation
		Posiva Oy set up 1995 to implement deep geological disposal
		Underground research laboratory Onkalo under construction
		Repository planned from this, near Olkiluoto, open in 2020
France	Reprocessing	Underground rock laboratories in clay and granite
		Parliamentary confirmation in 2006 of deep geological disposal, containers to be retrievable and policy "reversible"
		Bure clay deposit is likely repository site to be licensed 2015, operating 2025
Germany	Reprocessing but moving to direct disposal	Repository planning started 1973
		Used fuel storage at Ahaus and Gorleben salt dome
		Geological repository may be operational at Gorleben after 2025
Spain	Direct disposal	ENRESA established 1984, its plan accepted 1999
		Central interim storage at Villar de Canas from 2016 (volunteered location)
		Research on deep geological disposal, decision after 2010
Sweden	Direct disposal	Central used fuel storage facility (CLAB) in operation since 1985
		Underground research laboratory at Aspo for HLW repository
		Osthammar site selected for repository (volunteered location)
Switzerland	Reprocessing	Central interim storage for HLW used fuel at ZZL Wurenlingen since 2001
		Smaller used fuel storage at Beznau
		Underground research laboratory for HLW repository at Grimsel since 1983
		Deep repository by 2020, containers to be retrievable
United Kingdom	Reprocessing	Low-level waste repository in operation since 1959
		HLW from reprocessing is vitrified and stored at Sellafield
		Repository location to be on basis of community agreement
		New NDA subsidiary to progress geological disposal.

Germany's position regarding the nuclear waste management

The German government decided to begin a phase-out of nuclear power as source of electricity generation. This process will involve the decommissioning of the nuclear reactors and the managing of the large amount of nuclear waste in the coming years. The nuclear waste management strategy has already been discussed within the German government. Up to 2002, the nuclear reprocessing of spent fuel was allowed in Germany. Used fuel was transported to La Hague (France) or Sellafield (England) where the reprocessing took place. The vitrified high level waste that results from this process was transported back to Germany. Since 2005, the reprocessing of spent fuel is not allowed anymore, so that the used fuel is now considered as final waste in Germany. The waste is first stored in ponds, for example at the reactor sites, before being transported to the final repositories [5-7].

Scope of this PhD research project

The present work deals with ceramic waste forms and their role in the conditioning of the nuclear waste, in particular with regard to the MA. Due to their crystallinity, ceramics have more valuable properties than glasses and could therefore procure safer conditions for the disposal of the radioactive waste.

The analysis of the previous research on ceramic waste forms [8-11] shows that the focus should be made on phosphate material, in particular monazite-type ceramics. Once the choice on the material was made, the synthesis of the lanthanum-monazite ($LaPO_4$) will be performed. Several methods are available. However, the wet-chemical ways offer benefits as they are almost dust-free which is safer, if the monazite is doped with radionuclides. Hydrothermal synthesis is chosen due to its ability to procure good crystallinity at low temperature.

Structural and morphological characteristics (applying X-Ray Diffraction (XRD) and Scanning Electron Microscope (SEM)) combined with physical and thermal properties of the samples (using thermogravimetry, Differential Scanning Calorimetry (TG-DSC) and dilatometry) will be realized in order to describe the material. The use of state-of-the-art spectroscopy (Time Resolved Laser Fluorescence Spectroscopy (TRLFS) and Extended X-ray Absorption Fine Structure (EXAFS)) will permit the molecular level process

understanding of ceramic waste form. An essential parameter which describes the stability of the host phases is the dissolution rate under conditions of relevance for final repositories. A set-up and an experimental method will be built in order to obtain the initial rates on lanthanum phosphate and europium-doped lanthanum phosphate samples.

The objectives of this PhD thesis cover:

- the successful synthesis of monazite-type ceramics, including its doping with actinide surrogates, and the formation of a (La, Eu)PO_4 solid solution,
- the advanced characterization of monazite powder and monazite pellets, in particular with TRLFS,
- the development of a set-up for aqueous durability tests, the identification of the best synthesis method for the leached samples, and the discussion of the dissolution rate results.

2. Background

2.1. Nuclear fuel cycle

The nuclear fuel cycle is an industrial process which produces electricity from uranium in nuclear reactors. It starts with the uranium ore extraction and ends with the waste management [12]. Figure 2 shows a flow chart of the nuclear fuel cycle [13]. After the mining of natural uranium from uranium deposit, the raw material has to pass through several steps before being used as a fuel: the conversion of U_3O_8 into UF_6, the enrichment of natural uranium to increase its percentage of ^{235}U from 0.7 wt. % to 3-5 wt. %, and the fabrication of nuclear fuel assemblies containing uranium pellets. These three steps are named the front end [14].

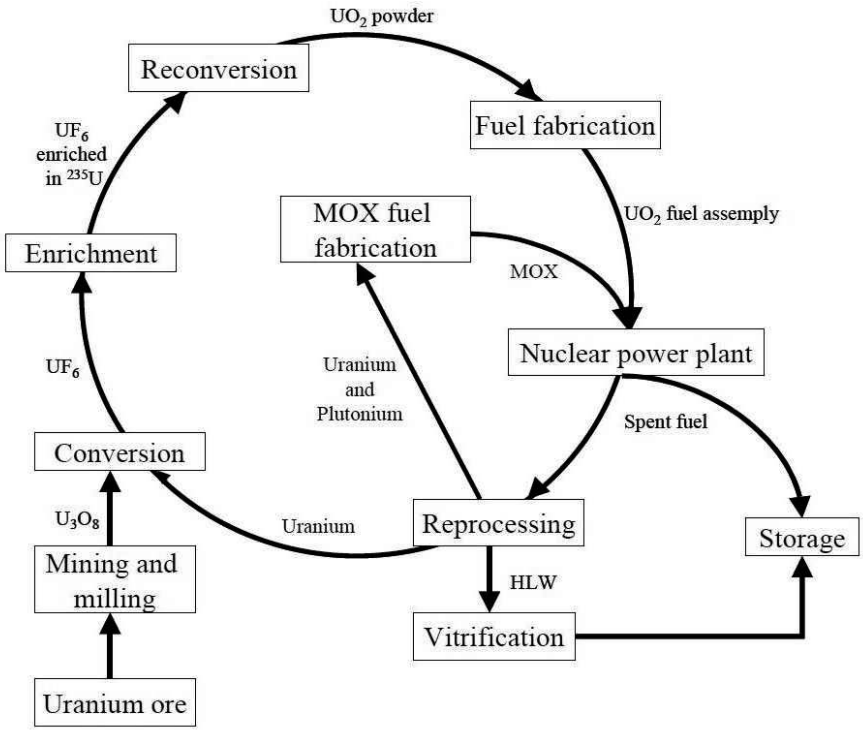

Figure 2: Nuclear fuel cycle [13].

Once the fuel assemblies are produced, they are used in a reactor during approximately three years. Electricity is produced with the heat generated from the nuclear chain reaction. The most operated reactor worldwide is the pressurized water reactor (PWR). It represents 60 % of the total nuclear power plants in operation (265 PWR out of 439 reactors worldwide) [15]. PWR is a type of light water reactor (LWR).

2.1.1. Spent fuel

The management of the irradiated fuel is referred to as the back end. Two options can be distinguished for the management of the used fuel: the open cycle and the closed cycle. In the open cycle the used fuel is a non-reusable waste which has to be stored and kept in places conceived to this end. In the closed cycle the spent fuel is recycled. Uranium and plutonium reprocessed from the final waste represent approx. 96 vol. % of the spent fuel. These elements can serve to produce the so-called MOX fuel which can be used as a new fuel in nuclear power plants [14]. Plutonium and the MA are long-lived radionuclides that are responsible for the long-term radiotoxicity.

Composition of spent fuel

The spent fuel composition four years after its discharge from PWR is shown in Table 2. The used fuel after a burn-up of 33 GWd/tHM is composed of 95.5 wt.% U, 0.97 wt.% Pu, 0.04 wt.% Np, 0.04 wt.% Am, 0.002 wt.% Cm and 3.374 wt.% fission products (FP). The content of Pu and MA (Np, Am, Cm) increases with the burn-up.

Table 2: Spent fuel composition of UOX fuels as a function of burn-up (expressed per ton of initial heavy metal). Four years after discharge from PWR [16].

	Mass of each elements (kg)		
Burn-up (GWd/tHM) / **Elements**	**33**	**41**	**50**
U	955.20	945.00	935.00
Pu	9.73	10.85	12.00
Np	0.42	0.55	0.72
Am	0.37	0.53	0.66
Cm	0.02	0.06	0.11
FP	33.74	42.25	51.30

2.2. Nuclear waste management strategies

Two complementary strategies can be discussed in the framework of the closed cycle approach: the partitioning and transmutation (P&T) and the partitioning and conditioning (P&C) strategies.

2.2.1. Partitioning and transmutation strategy

The aim of the P&T strategy is the reduction of the long-term radiotoxicity of the final waste [17]. The partitioning is the chemical separation of different long-lived elements of the spent fuel. Currently, uranium and plutonium are separated from the spent fuel via the well-known PUREX (Plutonium and Uranium Recovery by EXtraction) process. In this process, the spent fuel is dissolved in nitric acid, and afterwards the separation of uranium and plutonium is achieved by the liquid-liquid extraction using tributyl phosphate (TBP) as an extractant [18; 19]. MA cannot be separated within the PUREX process, so that additional steps are used. The first step is the co-extraction of MA and lanthanides from High Level Liquid Waste (HLLW) (e.g. French DIAMEX process) [18]. The second step is the separation of MA from lanthanides (e.g. SANEX process) [20].

Then, the long-term radiotoxic elements are embedded into a stable matrix. The nuclides are transformed into one or several other nuclides (stable elements or short-term radiotoxic elements) in a reactor. It is the consequence of neutron-induces fission and capture reactions [21]. This process is called transmutation.

Radiotoxicity

Radiotoxicity is the radiation dose [Sv] per ton of spent fuel [22]. Figure 3 shows the ingestion radiotoxicity versus time of LWR fuel at a burn-up of 50 GWd/tHM. The reference level is represented by the horizontal line. It corresponds to the radiotoxicity of the quantity of natural uranium needed to produce one ton of fresh fuel with an enrichment of 4.2 % ^{235}U. In order to analyze different P&T strategies, several cases are compared to the reference level: the open cycle (no P&T), a partial multiple recycling, and full multi-recycling.

In the case of the open cycle (the “Total” curve on Figure 3), the spent fuel is directly sent to a long-term repository. The radiotoxicity reference level will be reached after

130 000 years. In the case of the closed cycle, three red curves on Figure 3 show the P&T strategy:

- Multiple recycling of Pu (99.5 % efficiency) and one single recycling of Am (90 % efficiency) and Cm (90 % efficiency). The radiotoxicity reference level will be crossed after 1 500 years.
- Full multiple recycling of Pu (99.5 % efficiency), Am (95 % efficiency) and Cm (95 % efficiency). The radiotoxicity reference level will be reached after 1 000 years.
- Full multiple recycling of Pu (99.5 % efficiency), Am (99 % efficiency) and Cm (99 % efficiency). The radiotoxicity reference level will be reached after 500 years.

The FP radiotoxicity (black bold curve on Figure 3) shows the theoretical limit to the radiotoxicity if all actinides would be partitioned and transmuted. In this case, the reference level would be achieved after 270 years.

To conclude, the radiotoxicity of the spent fuel can reach the reference level after a time period between 500 and 1 500 years, instead of 130 000 years without P&T. This strategy permits the reduction of the long-term radiotoxicity of the final waste.

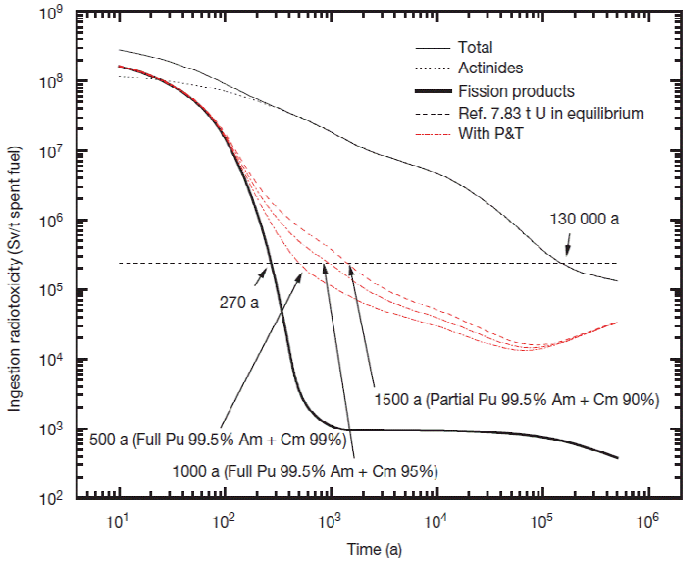

Figure 3: Evolution of ingestion radiotoxicity of one ton of LWR spent nuclear fuel at a burn-up of 50 GWd/tHM versus time. The horizontal line is the reference level: the quantity of natural uranium needed to produce one ton of fresh fuel with an enrichment of 4.2 % ^{235}U, i.e. 7.83 t [21; 23].

2.2.2. Partitioning and conditioning strategy

The P&C strategy is an alternative to the P&T strategy. After the partitioning of the spent fuel, the separated radionuclides are embedded in a suitable matrix and disposed in a deep underground repository. The radiotoxicity of the waste is not reduced by the P&C strategy, but the synthesis of the adapted matrices for the immobilization of the radionuclides increases the safety of the final disposal. Indeed, the host matrix constitutes an additional barrier between the radionuclides and the biosphere. The radionuclides have to be kept within the amorphous or crystal structures over long time periods (up to one million years) [24]. Ceramic matrices are considered to be beneficial for this purpose, thanks to their chemical durability, their tolerance to the radiation, and their natural analogues that show stability.

Safety case

Before a geological disposal for nuclear waste receives an approval for the construction, its safety has to be demonstrated. The safety assessment and the safety case are defined by the Nuclear Energy Agency (NEA) as follows [25]: “Safety assessment is the process of systematically analyzing the hazards associated with the facility and the ability of the site and designs to provide the safety functions and meet technical requirements,” whereas “the safety case is an integration of arguments and evidence that describe, quantify and substantiate the safety, and the level of confidence in the safety, of the geological disposal facility.” The development of a repository has to be discussed and argued between the involved parties, and the issues need to be resolved with technical arguments. The dialogue about each decision is the key of the achievement of the safety [25].

2.3. Nuclear waste forms for the P&C strategy

The P&C strategy requires the development of the host matrices for radionuclides. Glasses and ceramics present the well-known waste forms [2]. This section briefly describes glasses and considers the properties of the ceramic materials as host matrices in more detail. As it was mentioned above (see section 2.1.1), plutonium and the MA mainly govern the long-term radiotoxicity of spent fuel. Whereas the research on the

conditioning of Pu has already been covered in the numerous articles [26-31], the literature on the conditioning of MA is scarcer.

2.3.1. Glasses

Research on glass waste forms was realized in the last decades in the nuclear waste management field [32]. In some countries such as France, borosilicate glasses became the reference host for nuclear waste [33; 34]. Borosilicate glass can incorporate many different chemical elements (high chemical flexibility), has a low surface-to-volume ratio, its fabrication process is simple and feasible at industrial scale [2]. Besides these advantages, the major inconvenience of glass is its metastability. It has to be taken into account for the establishment of a model of a deep geological formation for long periods of time [2]. As crystalline materials are more stable than amorphous materials, ceramics that do not tend to be metamict are considered as promising alternative hosts for high-level waste.

2.3.2. Ceramics

Several reviews outline the benefits of ceramic waste forms compared to glass waste forms [28; 30; 35]. Table 3 summarizes relevant characteristics of different ceramic materials, in relation to the conditioning of radionuclides. Except for the existence of natural analogues, characteristics are rated as low, medium, and high: aqueous durability, radiation tolerance, chemical flexibility, and waste loading [8]. The most relevant properties are aqueous durability and radiation tolerance. Both features will be described in detail (see sub-sections 2.3.2.1 and 2.3.2.2). The chemical flexibility represents the ability of a host phase to incorporate different chemical elements. The analysis of natural analogues gives an approximation of the properties that can be expected from synthetic host phases. The stability over geological times can only be evaluated with natural analogues.

On the basis of these information, Zr- and Ti-based pyrochlores, zirconolite, monazite, apatites and murataite-type ceramics are considered to be serious candidates among the crystalline materials [8; 36].

Table 3: Summary of the performance characteristics of individual phases measured against potential selection criteria and other means of evaluation (e.g. natural samples) [8].

	Aqueous durability	Radiation tolerance	Chemical flexibility	Natural analogues
Perovskite	Low	Medium	Medium	Yes
Pyrochlore	High	Low-high	High	Yes
Zirconolite	High	Low-medium	High	Yes
Zircon	High	Low	Medium	Yes
Monazite	High	High	Medium	Yes
Zirconates	High	High	Medium	No
Zirconia	High	High	Medium	No
Brannerite	Medium	Low	Medium	Yes
Crichtonite	?	Low (?)	High	Yes
Murataite	High	Medium	High	Rare
Garnet	?	Low	High	Yes*
Titanite	Medium	Low	Medium	Yes
Apatite group	Medium	Low	Medium	Yes
Kosnarite	Medium	Low	Medium	Yes

*Natural garnets typically do not contain substantial amounts of Th or U.

However, some statements are also verified for crystalline waste forms in general. Their main advantages over glass are the incorporation of the radionuclides in well-defined atomic positions within the crystal lattice, a higher resistance to self-irradiation and a higher aqueous durability [37]. In addition, ceramics can also incorporate neutron absorbers (e.g. Hf and Gd [38]) to minimize the criticality issue, and the stability of crystalline compounds gives fixed thermodynamic data permitting the establishment of a model for their long-term behavior in a repository [2].

The goal of the P&C strategy is to find the matching matrix for each radionuclide. This goal implies a long-term research agenda, but this research would contribute to the general objective of the improving of the nuclear waste management safety. In the present work, monazite-type ceramics ($REPO_4$, with RE = La - Gd) have been investigated as potential host material (see chapter 2.6).

2.3.2.1. Aqueous durability of ceramics

The chemical durability of a sample can be analyzed with so-called aqueous alteration experiments. These investigations are performed in order to determine the dissolution rate of a sample immersed during a given period of time in a solution relevant for simulating repository conditions. In the framework of these experiments, the elementary concentration in the solution (release of elements in the leachate) [39] or the weight loss of the sample are measured. In addition, microstructural investigations are necessary, e.g. to observe possible formation of secondary phases.

As dissolution rates of most crystalline waste forms are low, the experimental conditions have to be adapted. To this end, powdered samples instead of monolithic ones are favored to increase the surface to mass ratio (measured in $m^2 \cdot g^{-1}$). In addition, the detection of such low concentrations in the solutions can only be detected by remarkable analytical methods having a very low detection limit (e.g. ICP-MS, see section 3.1.11).

Dissolution tests can be performed by static as well as dynamic methods: samples are immersed in a fixed volume of leachant for a static test, and leachant flow or regular replacement of leachant is used during a dynamic test.

The most common methods were classified in five kinds of tests (MCC-1 to MCC-5) by the International Standards Organization's Materials Characterization Centre (MCC, Battelle Pacific Northwest Laboratory, USA), showing the wide difference of leaching test methods used [32]:

- MCC-1: small volume of leachant without any agitation at 40 °C, 70 °C or 90 °C,
- MCC-2: test MCC-1 performed at higher temperature (110 °C, 150 °C and 190 °C),
- MCC-3: powdered samples, fixed ratio of leachant volume to samples mass, at temperature between 40 °C and 190 °C,
- MCC-4: single-pass flowing conditions,
- MCC-5: well-known Soxhlet test [32].

Some of these methods were chosen by the American Society for Testing and Materials (ASTM) as standard tests [40].

Results obtained in this work should be compared with values found in the literature, e.g. with the work of Oelkers and Terra [41; 42]. However, even if interest in the ceramics as host phases has grown in the last decades, data about the corrosion behavior are quite

limited so far. In addition, the existing data are not always directly comparable, due to diverse synthesis routes employed and/or different experimental conditions, for example due to the choice of the MA surrogate.

2.3.2.2. Radiation tolerance of ceramics

Radiation tolerance is required for crystalline materials pretending to be good candidates as nuclear waste forms. Radionuclide-containing ceramics are damaged by the radiation issued from the radioactive decays. This process is referred to as self-irradiation. As shown in Table 3, the radiation tolerance of ceramics is not equal for all host phases: e.g. monazite, zirconates and zirconia are known for their high resistance, whereas zircon, brannerite and apatite are low-resistant.

In order to simulate these damages at a laboratory scale and to define the radiation tolerance of a material with an appropriate technique, two different kinds of methods are used. The first and most realistic method is to dope the ceramic matrix with radionuclides and to study the damages. This approach requires handling these radioactive samples, what can cause problems for some analytical methods [32]. The second method is to simulate the inner irradiation by means of external bombardment of the matrix with ions, neutrons or electrons. In the literature, radiation tolerance tests on monazite-type ceramics are found for both methods. For example: synthesis of Pu-doped monazite [43], or ion bombardment (Au, He, Kr, Ar) at high energies (800 keV to 7 MeV) of natural and synthetic monazite [44-48].

The damage created by the self-irradiation is mainly due to the alpha-decay of actinides. The decay is composed of the alpha particle (He) and the recoil of the nucleus. The alpha particle (4.5 to 5.5 MeV) causes ionization as well as Frenkel defects. These defects result from an ion displaced from its lattice position to an interstitial site, creating a vacancy defect at its original site and an interstitial defect at its new site. Whereas the alpha recoil (70 to 100 keV) creates a collision cascade with the neighboring ions, causing the most localized structural damages. This causes the amorphization process, known as metamictization [49]. The critical amorphization temperature T_c of the material has to be taken into account for the planning of radiation tolerance tests. It represents the temperature above which the material cannot be amorphized anymore [50] and it

corresponds to the temperature at which the material recrystallizes after an amorphization process. Figure 4 shows the critical amorphization dose as a function of temperature for *RE*-orthophosphates in monazite structure or zircon structure.

The critical amorphization temperature T_c equals 60 °C for La-monazite, which is the lowest value among monazite-type crystals [50]. As a result, La-monazite recrystallizes at relatively low temperature (60 °C), which is a good property for a candidate as host matrix for radionuclides. Indeed, self-irradiation in La-monazite may induce damages in the structure, but the recrystallization will occur eventually.

After having induced radiation damages, the next step is their characterization. Several methods are suggested in the literature, for example the transmission electron microscopy (TEM) [51], the nuclear magnetic resonance (NMR) [49], and Raman spectroscopy [45].

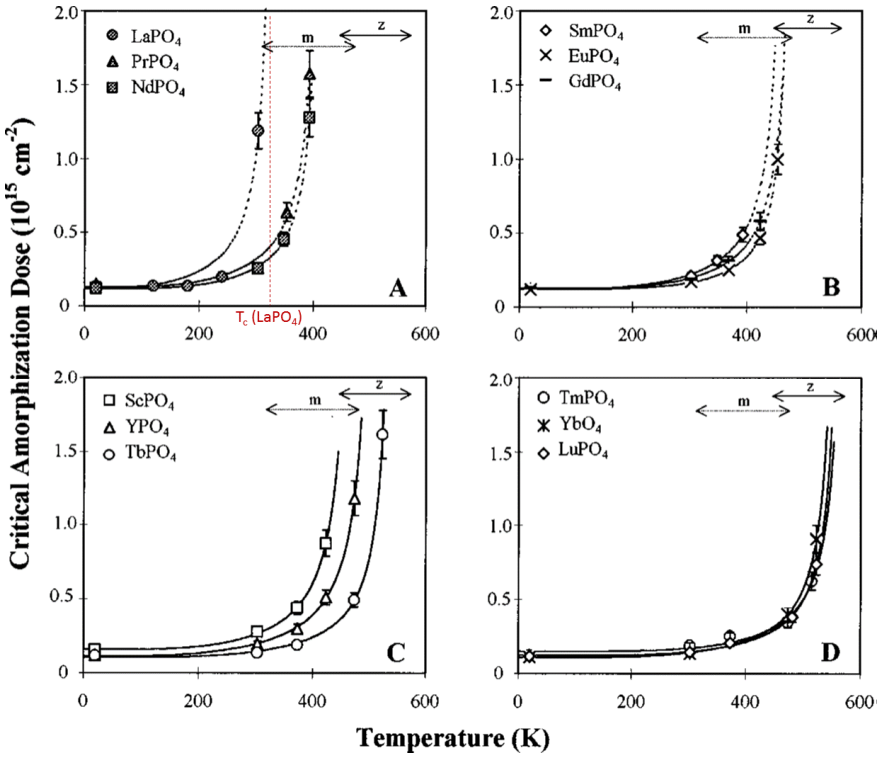

Figure 4: Critical amorphization dose versus temperature of *RE*PO_4 ceramics. The arrows marked with an *m* indicates the range of T_c values for the monazite structure and the ones with a *z* those for the zircon structure [50].

2.4. Lanthanides and actinides chemistry

Lanthanides are often used on a laboratory scale as actinide surrogates. Due to their electronic configurations, trivalent lanthanides have similar properties to trivalent actinides without being radioelements (besides promethium). Furthermore, as monazite is a mineral containing lanthanides (e.g. Ce and La) and actinides (Th, U), their properties are of importance for the understanding of the behavior of this waste form.

With regard to the samples synthesized in this work, the properties of lanthanum, europium and curium will be discussed in detail. The fluorescence properties of europium and curium will be outlined in the section 2.5.1.

2.4.1. Lanthanide chemistry

Lanthanides are found abundantly in the earth's crust. Nevertheless, they have been considered as rare in the past, so that these elements are mentioned as "rare-earth" (RE). As many actinide properties are similar to lanthanide properties, actinides are often referred to as the actinide rare-earths [52].

The lanthanides (*Ln*) are the 14 metals situated after the lanthanum (La, $Z = 57$) in the periodic table, from Ce ($Z = 58$) to Lu ($Z = 71$). They are so-called "4f-metals" as their 4f orbitals are partly or fully filled with electrons (see Table 4). Yttrium ($Z = 39$) and lanthanum ($Z = 57$) are often considered as lanthanides as they are linked to them due to similarities (e.g. the oxidation state). As a matter of fact, these elements usually found together with the lanthanides in nature [52]. In the following, La will be considered as a lanthanide.

Table 4: Electronic configuration of the lanthanides [53].

Atomic Number Z	Name	Symbol	Electronic Configuration Atom	Electronic Configuration Ion Ln^{3+}	Ground state Ion Ln^{3+}
57	Lanthanum	La	$5d^1\ 6s^2$	[Xe]	$^1S_0$
58	Cerium	Ce	$4f^1\ 5d^1\ 6s^2$	$4f^1$	$^2F_{5/2}$
59	Praseodymium	Pr	$4f^3\ 6s^2$	$4f^2$	$^3H_4$
60	Neodymium	Nd	$4f^4\ 6s^2$	$4f^3$	$^4I_{9/2}$
61	Promethium	Pm	$4f^5\ 6s^2$	$4f^4$	$^5I_4$
62	Samarium	Sm	$4f^6\ 6s^2$	$4f^5$	$^6H_{5/2}$
63	Europium	Eu	$4f^7\ 6s^2$	$4f^6$	$^7F_0$
64	Gadolinium	Gd	$4f^7\ 5d^1\ 6s^2$	$4f^7$	$^8S_{7/2}$
65	Terbium	Tb	$4f^9\ 6s^2$	$4f^8$	$^7F_6$
66	Dysprosium	Dy	$4f^{10}\ 6s^2$	$4f^9$	$^6H_{15/2}$
67	Holmium	Ho	$4f^{11}\ 6s^2$	$4f^{10}$	$^5I_8$
68	Erbium	Er	$4f^{12}\ 6s^2$	$4f^{11}$	$^4I_{15/2}$
69	Thulium	Tm	$4f^{13}\ 6s^2$	$4f^{12}$	$^3H_6$
70	Ytterbium	Yb	$4f^{14}\ 6s^2$	$4f^{13}$	$^2F_{7/2}$
71	Lutetium	Lu	$4f^{14}\ 5d^1\ 6s^2$	$4f^{14}$	$^1S_0$

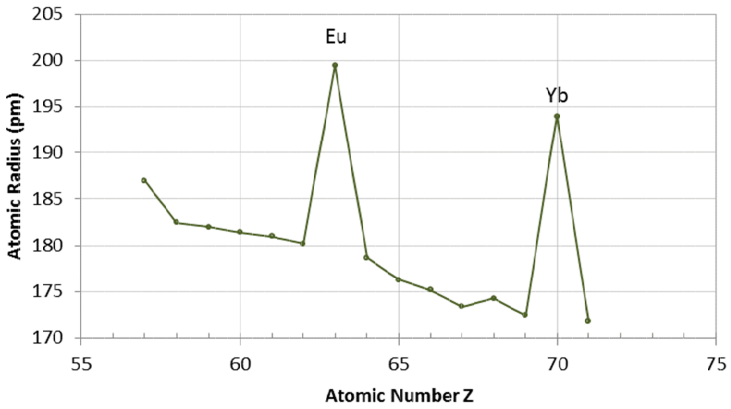

Figure 5: Atomic radius (pm) versus atomic number Z of the lanthanides (data from [53]).

In general, lanthanides show notable differences when they are in metal phases. The plot of the atomic radius versus the atomic number (see Figure 5) shows clearly that the radius values of Eu (r_{At} = 199.5 pm) and Yb (r_{At} = 194.0 pm) are much higher than the others (between r_{At} = 171.8 pm for Lu and r_{At} = 187.0 pm for La). This particularity leads to repercussion on other properties of these lanthanides: Eu and Yb are the two minima in the melting point curve as well as in the density curve of the lanthanides [54]. Another distinction between lanthanides is the high difference of the melting point of cerium (T_m = 798 °C) and lutetium (T_m = 1656 °C) [54].

The oxidation state of lanthanides is generally +III. Nevertheless, some lanthanides can be reduced to +II (Sm, Eu, Tm and Yb) and some can be oxidized to +IV (Ce, Pr, Nd, Tb, Dy). However, all lanthanides are mostly trivalent in aqueous solution, whereas Eu (II) and Ce (IV) are metastable. Contrary to the case of metals, the lanthanide properties are alike in solution and they are difficult to separate from each other. Figure 6 shows the effective ionic radius of Ln^{3+} versus the atomic number of the lanthanides, in case of a coordination number (CN) equals nine (red plot) and equals eight (blue plot). Indeed, non-hydrated lanthanide orthophosphates ($LnPO_4$) can show two different crystal structures, monazite-like and xenotime-like, depending on the size of the cation. For Ln = La - Gd, the cation is surrounded by nine oxygen, whereas for Ln = Tb - Lu, the cation is surrounded by eight oxygen. Nevertheless, Eu, Gd and Tb can actually be found in both structures (see section 2.6.2).

Figure 6 shows that Ln^{3+} ions are getting smaller as Z grows: this is the lanthanide contraction, an aperiodic property of the lanthanides. This contraction is due to the 4f-electrons. As the f orbitals are diffuse, their electrons are less located, which leads to a poor shielding of the nuclear charge. As a result the 6s-electrons are stronger attracted to the nucleus and the radius is decreasing from La^{3+} to Lu^{3+} [53; 55].

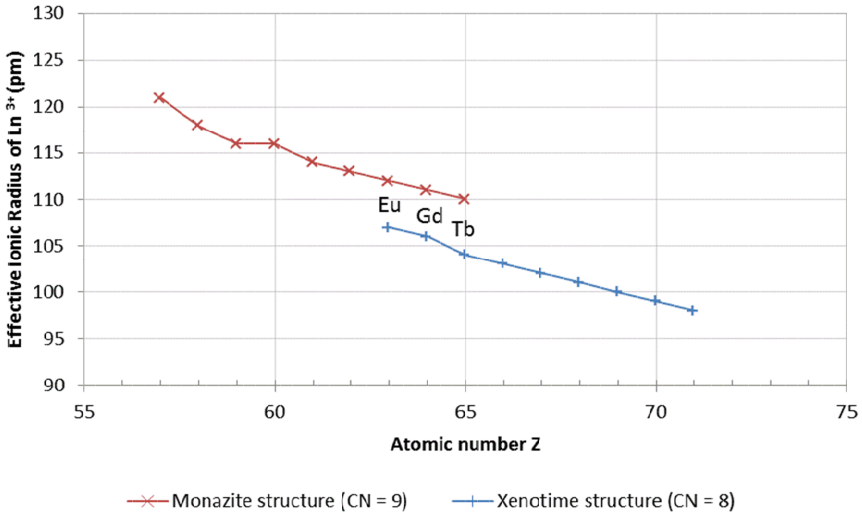

Figure 6: Effective ionic radius of Ln^{3+} (pm) versus atomic number Z of the lanthanides, in case of a CN equals to 9 (red plot) and a CN equals to 8 (blue plot) (data from [56]).

2.4.1.1. Lanthanum chemistry

In nature, La is composed mostly of ^{139}La (99.91 %), the other 0.09 % being ^{138}La. Both isotopes are stable. More than 30 synthetic radioisotopes are referenced (from ^{117}La to ^{154}La) [53]. Lanthanum gave its name to the lanthanides and is also often referred to as part of them, even if its electronic configuration does not correspond to the official definition. As mentioned before, its 4f electronic level is empty, contrary to the other lanthanides (see Table 4). However, La is part of the scandium-group in the periodic table, together with Sc, Y and Ac.

Each element of the group can be easily oxidized, but La is the most reactive element. These elements reduce water and diluted acids. In both cases a H_2 formation is observed [53]. Lanthanum trioxide (La_2O_3) is formed as a white powder with the burn-up of La in air or with the glowing of oxalate, nitrate and other salts. The freshly prepared oxide reacts with water under heat formation and is as soluble as burnt lime (CaO) [53]. Lanthanum nitrate ($La(NO_3)_3$), which is used for the synthesis of $LaPO_4$ in this work (see section 3.1.2), can be obtained by dissolving La_2O_3 in nitric acid.

The preferential CN of La are eight and nine (e.g. CN = 8 in xenotime-type ceramics and CN = 9 in monazite-type ceramics and $[La(H_2O)_9]^{3+}$). Complexes with CN smaller than eight or higher than nine can also occur (e.g. CN = 12 in $La_2(SO_4)_3 \cdot 9H_2O$).

2.4.1.2. Europium chemistry

Eu occurs as two isotopes in nature: ^{151}Eu (47.8 %, unstable) and ^{153}Eu (52.2 %, stable). 29 other synthetic radioisotopes are referenced (from ^{130}Eu to ^{162}Eu) [53; 57].

Eu is the most reactive lanthanide [53]. Just as La, Eu is a strong reducing agent for water and acids. In both reactions a formation of H_2 is observed. At high temperatures, Eu burns under the formation of Eu_2O_3. The sesquioxide is soluble in acids and forms a hydrate ($[Eu(H_2O)_9]^{3+}$).

Like the other lanthanides, Eu ($4f^7\ 6s^2$) is usually trivalent ($4f^6$) but it can also be divalent ($4f^7$), which is not common for the lanthanides. Indeed, Eu_2O_3 can be reduced to the mono-oxide EuO. This is due to the electron configuration $4f^7$ that has a half-filled f-shell procuring more stability than the electron configuration $4f^6$.

2.4.2. Actinide chemistry

The actinides (*An*) are the 14 metals following actinium (Z = 89) from thorium (Z = 90) to lawrencium (Z = 103). Every actinide isotope is radioactive and only U, Th, and primordial ^{244}Pu are found in nature. Like La for the lanthanides, Ac gave its name to the actinides and is also often referred to as an actinide. In the following, Ac will be considered as an actinide.

Their properties are comparable to these of the lanthanides due to the similarity of their electronic levels. Besides the thorium, the 5f level of actinides is partly or completely filled with electrons (see Table 5 [53]). Just as the Ln^{3+} contraction, the An^{3+} contraction is observed for the actinide radii measured until now (from 126 pm for Ac^{3+} down to 109 pm for Cf^{3+}) [53].

Table 5: Electronic configuration and oxidation state (the most stable are bold) of the actinides [53].

Atomic Number Z	Name	Symbol	Electronic Configuration Atom	Oxidation State
89	Actinium	Ac	$6d^1\ 7s^2$	**3**
90	Thorium	Th	$6d^2\ 7s^2$	3, **4**
91	Protactinium	Pa	$5f^2\ 6d^1\ 7s^2$	3, 4, **5**
92	Uran	U	$5f^3\ 6d^1\ 7s^2$	3, 4, 5, **6**
93	Neptunium	Np	$5f^4\ 6d^1\ 7s^2$	3, 4, **5**, 6, 7
94	Plutonium	Pu	$5f^6\ 7s^2$	3, **4**, 5, 6, 7
95	Americium	Am	$5f^7\ 7s^2$	2, **3**, 4, 5, 6
96	Curium	Cm	$5f^7\ 6d^1\ 7s^2$	**3**, 4
97	Berkelium	Bk	$5f^9\ 7s^2$	**3**, 4
98	Californium	Cf	$5f^{10}\ 7s^2$	2, **3**, 4
99	Einsteinium	Es	$5f^{11}\ 7s^2$	2, **3**
100	Fermium	Fm	$5f^{12}\ 7s^2$	2, **3**
101	Mendelevium	Md	$5f^{13}\ 7s^2$	2, **3**
102	Nobelium	No	$5f^{14}\ 7s^2$	2, **3**
103	Lawrencium	Lr	$5f^{14}\ 6d^1\ 7s^2$	2, **3**

Water or alkaline solutions do not attack actinide metals. However, boiling water creates an oxide-coating on the surface of the metal and acids dilute them more or less completely with H_2 and *An*-cations formation [53]. From $Z = 95$ (Am) to $Z = 103$ (Lr), the most stable oxidation state is +3. The An^{3+} fluoride, hydroxide and oxalate are insoluble in water, whereas An^{3+} chloride, bromide, iodide, nitrate and sulfate are soluble in water [53].

As presented in Table 5, Cm can show a valence +III or +IV. Cm valence is mainly +III in solution. Cm (III) can be synthesized by the oxidation of Cm metal (e.g.: dissolution in acid). As Cm (IV) is a very strong oxidizing agent, it oxidizes water to O_2 under the formation of Cm (III). Here, La-monazite was doped with ^{248}Cm, which has a half-life of 3.48×10^5 years [58].

2.5. Spectroscopic methods

Long-range order methods like X-ray diffraction (XRD) are used to define the structure of a crystalline sample. Short-range order methods, like time resolved laser fluorescence spectroscopy (TRLFS) and extended X-ray absorption fine structure (EXAFS), investigate qualitatively and quantitatively the local environment of elements in a given structure within a sample (in solution and solid state).

Short-range order spectroscopy permits the molecular level understanding of ceramic waste forms. TRLFS (emission) and EXAFS (absorption) measurements are complementary methods and contribute to a better understanding of the incorporation mechanism of dopant elements.

2.5.1. Time resolved laser fluorescence spectroscopy

2.5.1.1. Difference between fluorescence and phosphorescence

The luminescence spectroscopy can be used to explore the coordination chemistry of the lanthanides and actinides ions [59].

In some chemical elements, after the absorption of energy (excitation) and due to certain electronic transitions, electrons emit their energy excess as light (relaxation). This is called luminescence. The emanated light is a function of the local environment of the atom, i.e. of the coordinated ligands. In order to interpret the spectrum, knowledge about electronic configuration of the ions and quantum physics selection rules is required [60].

A diagram of electronic transitions, named Jablonski diagram, illustrates the processes that usually happen within a fluorophore, between the absorption and the emission of light (see Figure 7) [61]. S_0 is the singlet ground state, S_1 and S_2 are the first and second singlet excited states, S_n the n^{th} excited state. The vertical arrows represent the electronic transitions occurring during absorption or emission of photons.

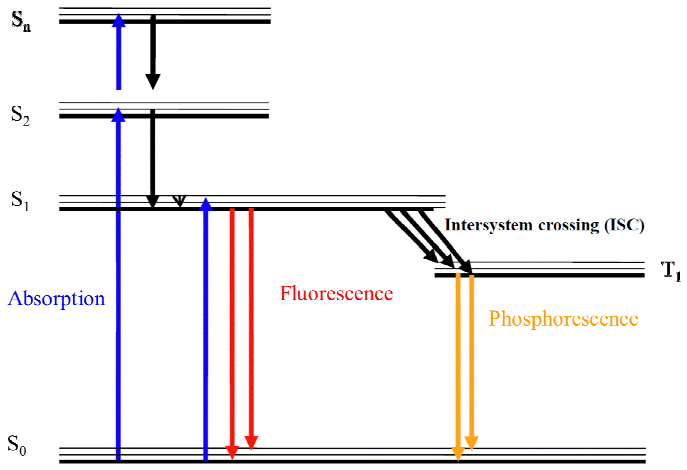

Figure 7: Jablonski diagram (modified from [62]).

Due to light absorption, an electron of a fluorophore is excited to a high vibrational level S_n (blue arrows on Figure 7). Then, it rapidly relaxes to the lowest energy level of the excited state S_1 by dissipating a part of its energy in its environment. This phenomenon is called internal conversion and occurs in 10^{-12} s or less.

Several processes may occur during the relaxation of the electron from S_1 to the ground state S_0, two of them are schematically represented on Figure 7.

The electronic relaxation from the excited state S_1 to the ground state S_0 can occur through emission of a photon. This is called fluorescence (red arrows on Figure 7). The relaxation can also follow a different route. Electrons at the excited state S_1 undergo first a spin conversion to the first triplet state, T_1 (excited state). Conversion of S_1 to T_1 is called intersystem crossing (ISC). The relaxation of the molecules from the lowest energy level of T_1 to the ground state S_0 occurs via emission of a photon (shifted to longer wavelengths relative to fluorescence). This phenomenon is called phosphorescence (yellow arrows on Figure 7) [63].

As a result, the difference between phosphorescence and fluorescence is related to the time needed by the excited electron to return to its ground state. In the case of fluorescence, an almost instant return is observed, whereas in the case of phosphorescence this process can last up to hours [64].

According to the definition of the different luminescence processes, the following work describes phosphorescence processes. However, the luminescence of Eu (III) and Cm (III) is mostly referred to as fluorescence. This convention will also be applied in this work.

2.5.1.2. Elements with fluorescence ability

The electrons of the ions Cm (III), Eu (III), Am (III) and U (VI) are able to relaxate from an excited state into the ground state by fluorescence. Therefore, these elements are suitable dopants for TRLFS measurements.

Here, europium was chosen as surrogate for trivalent actinides and curium as trivalent actinide for doping the monazite-type crystal structure. Two monazite-type samples doped respectively with europium and curium were measured. However, doping a ceramic with one element does not imply that all dopant atoms have the same local atomic environment, even if they are in the same oxidation state. In a sample with a unique doping element, several species, i.e. with different atomic neighbors, can be found. For a good comprehension of the results, the most simple case will be explained: the case of an ion surrounded just by water molecules, an aquo ion called free ion.

The chemical properties of both europium and curium have already been discussed in the previous chapter (2.4). Their fluorescence characteristics will be given in the subsequent section.

Curium

The sensitivity of TRLFS for Cm (III) is very high and it is a major advantage for the experiments. The detection limit was determined experimentally in 0.1 $mol \cdot L^{-1}$ $HClO_4$ to be $5.5 \cdot 10^{-12}$ $mol \cdot L^{-1}$ [65]. Speciation information can be obtained below 1 ppm, as a concentration only about 10^{-9} to 10^{-7} $mol \cdot L^{-1}$ is needed [65].

Figure 8 represents the energy levels of a free Cm ion excited by UV light (λ = 396.6 nm). There is a non radiative relaxation to level $^6D_{7/2}$. The electrons relaxing from level $^6D_{7/2}$ to the ground state $^8S_{7/2}$ emit photons, with a wavelength λ = 593.8 nm.

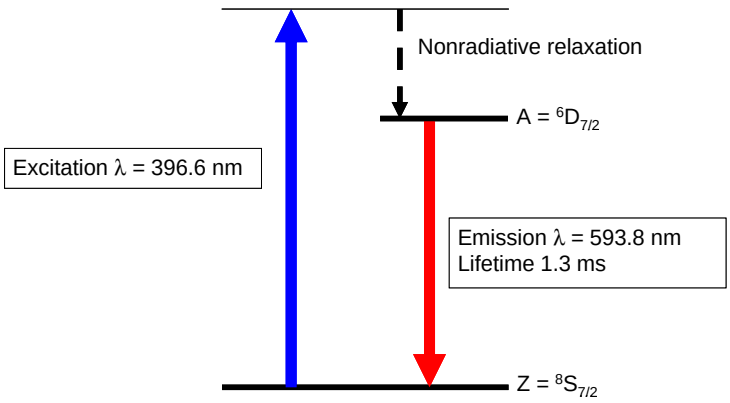

Figure 8: UV excitation of a free curium ion [66].

As mentioned above (see sub-section 2.5.1.2), different local environments can lead to different Cm species in the same compound. With UV excitation (λ = 396.6 nm), all Cm species are simultaneously excited.

Figure 9 is a graph of the curium fluorescence emission versus the wavelength λ (nm) of three Cm species. The first peak corresponds to a Cm (III) aquo ion, showing its emission maximum at λ = 593.8 nm (transition from $^6D_{7/2}$ level to $^8S_{7/2}$ level). According to [67], the second and third peaks correspond to two Cm (III) species sorbed onto a calcite sample, showing emission maxima respectively at λ = 607.5 nm and λ = 618.0 nm. Compared with the aquo ion, the peaks are shifted to higher wavelength, this is called a red shift.

The neighbors of the ion strongly influence the spectroscopic properties. The stronger the complexation, the longer the wavelength of the emitted light. Figure 9 shows that the Cm (III) species sorbed onto calcite have a stronger complexation with the neighbor ligands than the free Cm (III) ion with the water molecules.

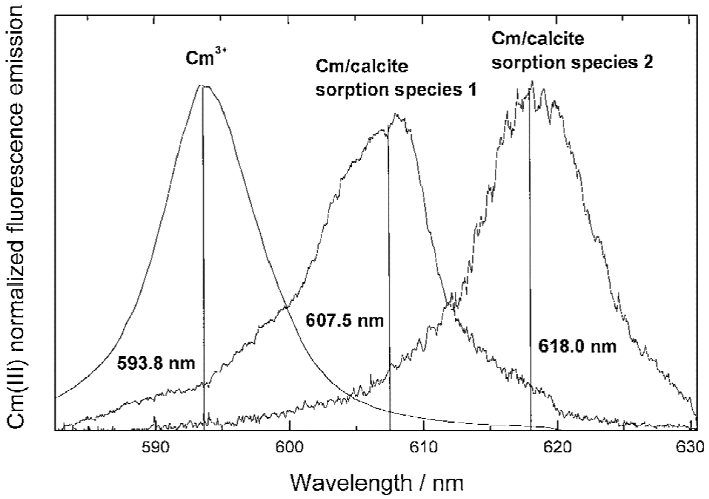

Figure 9: Fluorescence emission spectra of Cm (III) aquo ion, Cm (III)/calcite sorption species 1 and Cm (III)/calcite sorption species 2 [67].

Europium

Europium was chosen as surrogate for trivalent actinides. The ground state is split in seven levels: ^7F_J with $J \in [0, 6]$ (see Figure 10) and each level ($^7F_{0\text{-}6}$) can be splitted in $2J+1$ levels, according to the surrounding ligands.

The fluorescence of Eu (III) almost always occurs from the first excited level $^5D_0$ to the ground state. The peaks observed in the spectra correspond to the transitions from $^5D_0 \rightarrow {}^7F_J$. The most interesting transitions are from $^5D_0$ to $^7F_0$, $^7F_1$ and $^7F_2$ [60]. The transition $^7F_0 \rightarrow {}^5D_0$ is particularly useful for the interpretation of the excitation spectrum of Eu (III) ions. The ground state ($^7F_0$) and the excited state ($^5D_0$) are both non-degenerate, as a consequence each Eu (III) specie presents a single peak in the excitation spectrum. The total number of Eu (III) species in a sample can be identified accordingly.

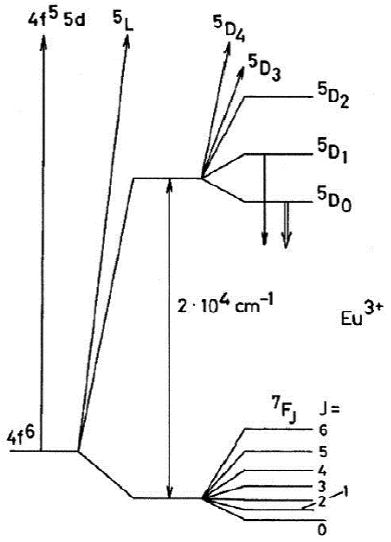

Figure 10: Energy levels of Eu (III) in the visible spectrum [68].

This transition has a low intensity. Indeed, the 0-0 transition is forbidden by electronic rules and even by symmetry selection rules if a Eu (III) ion has a high symmetry environment or a center of inversion is present. As a result, the intensity of the 0-0 transition can be used to estimate the grade of the symmetry of Eu (III) [59; 60].

The energy levels of a free Eu (III) ion excited by UV light (λ = 394 nm) are shown on Figure 11. After the absorption of light ($^7F_0 \rightarrow {}^5L_6$ transition), a non-radiative relaxation to level $^5D_0$ occurs. The electrons relaxing from level $^5D_0$ to the ground state emit photons at different wavelengths due to the splitting of the ground state.

Figure 12 shows a graph of the Eu (III) fluorescence emission versus the wavelength (nm) of a free Eu (III) ion. The sample is excited by UV light and the peaks of the first four levels ($^7F_0$ to $^7F_3$) are shown. Compared to the spectrum of a free Cm (III) ion (Figure 9), the spectrum of a free Eu (III) ion is less trivial as it has several peaks. In the case of a non-free ion, Eu (III) as well as Cm (III), all species would be excited simultaneously with UV light.

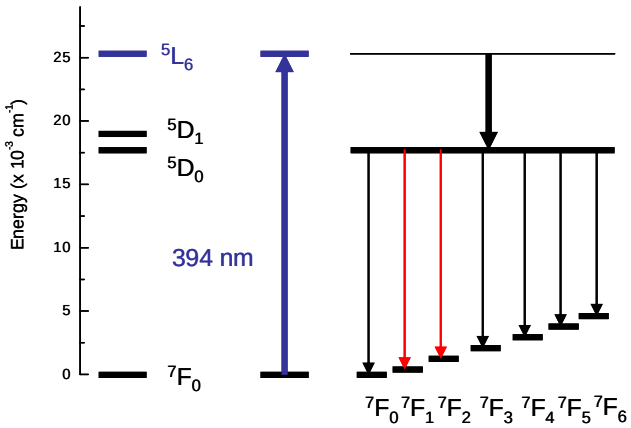

Figure 11: Energy levels of a free Eu (III) ion excited by UV light [66].

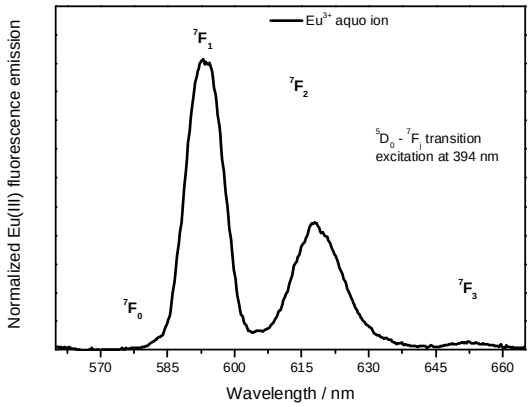

Figure 12: Eu (III) fluorescence emission versus the wavelength (nm) of a free Eu ion (partly [60]).

Figure 13 shows the energy levels of a Eu (III) species. Different species can be excited individually in an energy range between 577 nm and 583 nm, because the energy gap between $^7F_0$ and $^5D_0$ is different for each species. This is called a direct excitation. The seven levels of the ground state will occur in the spectrum of a measurement realized by direct excitation, as they are inherent in Eu.

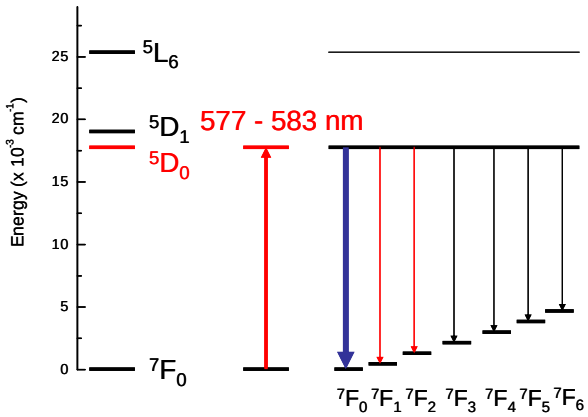

Figure 13: Energy levels of a free Eu ion excited by direct excitation [66].

2.5.1.3. Fluorescence lifetime

As mentioned above (see sub-section 2.5.1.1), after the absorption of photons, a fluorophore remains in an excited state during a given time before the relaxation. The mean time spent by the molecules in the excited state is called fluorescence lifetime. Graphs representing lifetime measurements show fluorescence emission versus time (µs) [63].

As an example, Figure 14 shows a scheme of lifetime measurements of two Cm (III) samples, a free Cm (III) ion (black) and a Cm (III) ion incorporated in calcite (red). These plots can be analyzed qualitatively. Both are decreasing because of the relaxation of the electrons from the excited state to the ground state. The plot of the free Cm (III) ion shows one slope, meaning the sample is composed of a single species. Whereas the plot of the Cm (III) ion in calcite shows two different slopes, meaning the sample is here composed of two species.

These graphs (Figure 14) can also be analyzed quantitatively as the lifetime is influenced by quenching. The main quenching effect observed in aqueous systems is the relaxation due to the OH oscillation bands. The process is shown Figure 15. During the relaxation of the excited electron, the OH-molecules absorb energy (energy transfer) which induces a faster return of the electron to the ground state.

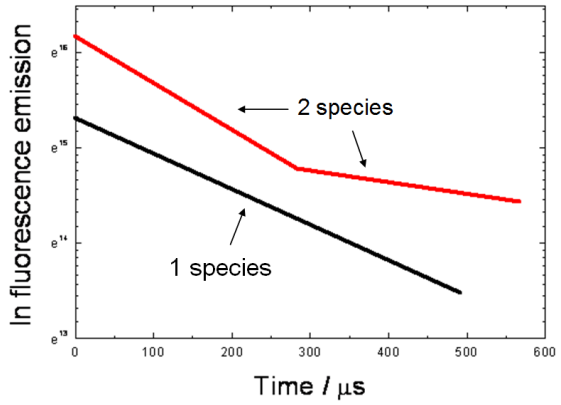

Figure 14: Lifetime measurements: Cm (III) fluorescence emission versus the time (µs) of a free Cm (III) ion (black) and a Cm (III) ion in calcite (red) [66].

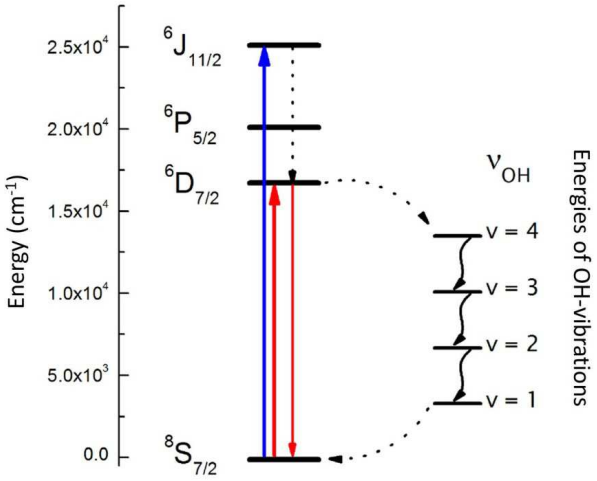

Figure 15: Scheme of the radiationless relaxation of Cm (III) via OH-vibration (modified from [60]).

The effectiveness of the quenching is related to the distance between the ions: if this distance is too long, the quenching effect is insignificant. The impact of the second coordination sphere can then be assumed to be negligible. On the basis of this assumption, Horrocks Jr. developed an empirical equation in 1979, by correlating the number of water molecules (*n* (H_2O)) in the first coordination sphere of a europium ion

and the fluorescence lifetime (see equation (1)). Fifteen years later, Kimura developed a similar equation by correlating the number of water molecules in the first coordination sphere of a curium ion and the fluorescence lifetime (see equation (2)). The typical error of both the Horrocks and the Kimura equations is ± 0.5 (H_2O).

[69] $$n\,(H_2O) = 1.07\,k_{obs} - 0.62 \quad (1)$$

[70] $$n\,(H_2O) = 0.65\,k_{obs} - 0.88 \quad (2)$$

Where k_{obs} is the decay constant ($m \cdot s^{-1}$).

2.6. Monazite

2.6.1. Structure, composition and occurrence

Monazite is a phosphate discovered by Johann August Friedrich Breithaupt. In 1829 he reported on monazite for the first time [71]. Breithaupt claimed that this mineral was found in a zircon- and iron-ore in Siberia and described it in German as *"ein ausgezeichnetes Einzelwesen"*. The term "monazite" has its etymological origins from the Greek *μονάζειν* (meaning "to be alone") because of its crystals standing alone in the rock [71].

Monazite (*RE*PO_4) is a monoclinic orthophosphate composed of *RE*O_9 polyhedra and PO_4 tetrahedra (see Figure 16). *RE* is surrounded by nine oxygen. Each oxygen is positioned at a different distance (between 2.484 Å and 2.813 Å) [72].

Its quantitative chemical composition is given in Table 6 [55]. The mineral is composed of different rare-earths: Ce, Y, La, Nd, Th and Pr. Furthermore, natural monazite discovered in Piona (Italy) contained a very high amount of actinides: 11.34 wt.% of ThO_2 and even 15.65 wt.% of UO_2 [73]. These high contents make monazite one of the principal sources of rare-earth metals together with bastnaesite [55]. Besides Italy, the mineral occurs in beach sands from Brazil, India and Australia [74].

The stability domains regarding the temperature of the system La_2O_3-P_2O_5 is described on the phase diagram on Figure 17. It contains the following compounds: La_5PO_{10}, La_3PO_7, $LaPO_4$, $La(PO_3)_3$ and La_5PO_{14} [75]. According to Kropiwnicka, $LaPO_4$ has a melting point higher than 2200 °C. However, in the work of Hikichi, the melting temperature of La-monazite is found to be 2072 °C ± 20 °C [76], which is a higher value

than the one of Al_2O_3 (2050 °C) [77]. $LaPO_4$ has no “domain” of stability on its own. However, at 30.35 wt.% of P_2O_5 (corresponding to 1:1 molar ratio), $LaPO_4$ is the only stable component. At a La-richer molar ratio, $LaPO_4$ has a stability domain together with La_3PO_7 up to 1580 °C (marked in red on the diagram). The structure of La_3PO_7 is like a stack of La_2O_3 and $LaPO_4$ structures [78].

Table 6: Chemical composition of natural monazite [79].

Wt.%	Ce_2O_3	Y_2O_3	$(La,Nd)_2O_3$	Fe_2O_3	ThO_2	P_2O_5	$(Pr,Y)_2O_3$
Min.	21.1	1.15	27.9	0.1	5.65	24.9	0.5
Max.	34.0	4.66	41.8	1.5	12.0	29.7	2.2

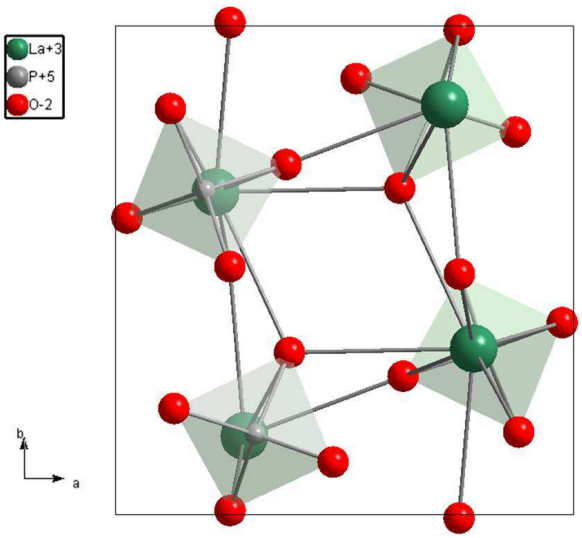

Figure 16: Crystal structure of $LaPO_4$.

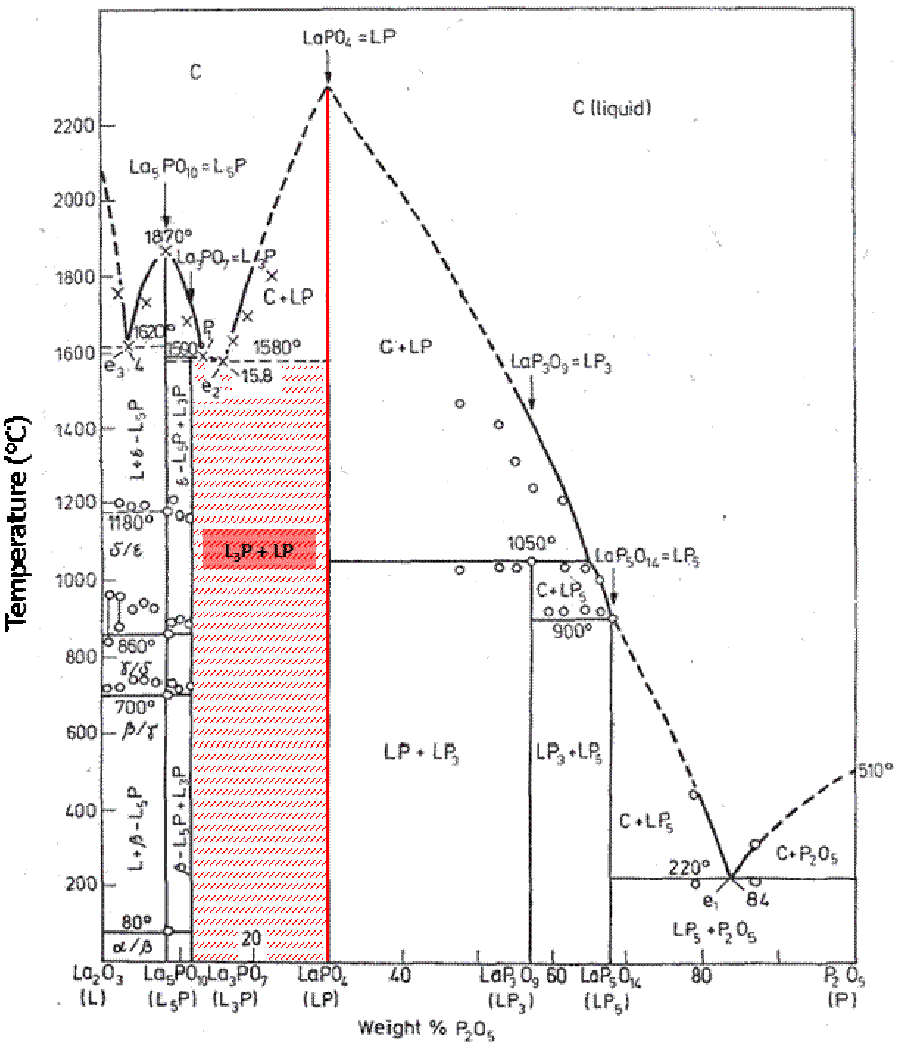

Figure 17: Phase diagram of La_2O_3 – P_2O_5 [75]. The red part corresponds to the composition of the La-monazite synthesized here.

2.6.2. Monazite versus xenotime

As shown in Table 6, the monazite mineral is composed mainly of light rare earths. If composed by heavy rare earths, which are smaller ions, the symmetry within the *RE*PO_4 mineral is different. The mineral is named a xenotime and its crystal structure shows a tetragonal symmetry [79], isostructural to the mineral zircon ($ZrSiO_4$) [80]. Figure 18 shows which structure preponderates in natural phosphates with regard to the rare earths. Minerals with lanthanides between La and Eu show principally a monazite structure, whereas minerals with lanthanides from Gd up to Lu show a xenotime structure.

In the continuation of the work, synthetic *RE*PO_4 ceramics will be named after their natural mineral analogues: monazite for *RE* = La - Gd (monoclinic structure) and xenotime for *RE* = Tb - Lu and Y (tetragonal structure). Both monazite and xenotime have hydrated forms: rhabdophane and weinschenkite respectively.

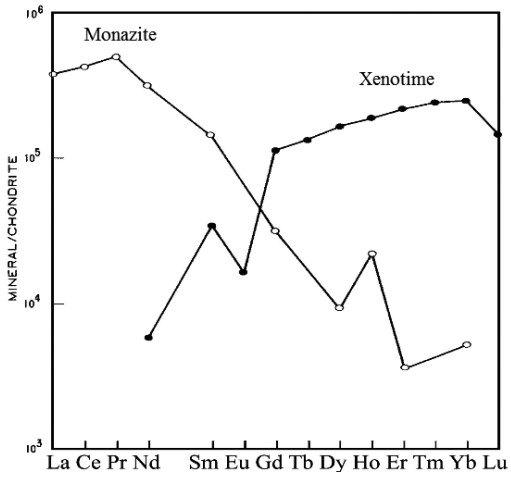

Figure 18: Rare earth abundances in coexisting monazite and xenotime, normalized to average chondrite mineral [79].

2.6.3. Synthesis methods

Several methods can be used to synthesize monazite samples. The most common methods are the solid state reaction [81], the hydrothermal synthesis [82], the precipitation [83] and the sol-gel method [84].

In the present work hydrothermal synthesis was chosen as synthesis method, as it is an almost dust-free route. This is of great interest when handling radioelements. Another advantage of this method is the very low temperature applied for the hydrothermal synthesis (200 °C). The method will be outlined in the section 3.1.2.

Once the synthesis route is adopted, tests have to be performed with surrogates before doping the matrix with radioactive elements. Here, the surrogates are lanthanides, as their properties are similar to the properties of the actinides (see chapter 2.4). Doped *RE*PO_4 ceramics can contain up to 100 mol% of actinide in the *RE*-position, for *RE* = Pu - Es [85].

2.6.4. Monazite as a host phase for actinides

The concept adopted in this work is the biomimicry. The functioning of natural processes is observed and mimicked, as these processes already demonstrated their advantages in nature. This concept already shows advantages in many scientific areas [86-88].

In long-term repositories for HAW, an intrusion of water over the years is the worst-case scenario. Optimal host matrices have to be stable while being in contact with aqueous solutions. As already mentioned (section 2.6.1), monazite is a mineral found in beach sands from different countries (Brazil, India, Australia, etc.), thus it is chemically durable with regard to aqueous alteration processes [37]. Table 7 gives the dissolution rates of Manangotry monazite found by Oelkers [41]. The chemical formula of this natural monazite is as follows:

$(Ca_{0.04}La_{0.21}Ce_{0.43}Pr_{0.05}Nd_{0.15}Sm_{0.02}Gd_{0.01}Th_{0.13})P_{0.90}Si_{0.09}O_4$.

The dissolution rates *r* (Ce) given in Table 7 correspond to the release of Ce into leachate at pH = 2. The concentration of Ce was determined by ICP-MS. The dissolution rate is comprises between $5.23 \cdot 10^{-6}$ $g \cdot m^{-2} \cdot d^{-1}$ at 50 °C and $1.49 \cdot 10^{-3}$ $g \cdot m^{-2} \cdot d^{-1}$ at 200 °C, thus it increases with the temperature.

The lanthanide orthophosphates exist in nature and contain usually a significant amount of thorium and uranium, but have been found to be weakly metamict [37; 89]. This suggests that the structure is resistant to radiation damage and allow the incorporation of

radionuclides. A more than three-billion-years old monazite mineral was discovered in Australia, which proves its stability over time [90].

Because of these characteristics, monazite appears to be a perfect candidate for further research concerning its ability to serve as host matrix for the conditioning of MA.

Table 7: Steady state natural Manangotry monazite dissolution rates obtained by Oelkers [41].

pH	Temperature (°C)	r (Ce) ($g \cdot m^{-2} \cdot d^{-1}$)
2.03	50	$5.23 \cdot 10^{-6}$
2.02	70	$1.33 \cdot 10^{-5}$
1.97	150	$1.28 \cdot 10^{-4}$
2.00	200	$1.49 \cdot 10^{-3}$

3. Experimental part

3.1. Chemicals, methods and apparatuses

3.1.1. Chemicals

Lanthanum nitrate:	$La(NO_3)_3 \cdot 6H_2O$, Sigma-Aldrich, 99.99 % pure
Europium nitrate:	$Eu(NO_3)_3 \cdot 6H_2O$, Alfa Aesar, 99.9 % pure
Lanthanum oxide:	La_2O_3, Alpha Aesar, 99.99% pure
Europium oxide:	Eu_2O_3, Alpha Aesar, 99.99% pure
Sodium hydroxide:	NaOH, Merck, ≥ 98 % pure
Diammonium hydrogen phosphate:	$(NH_4)_2HPO_4$, Merck, ≥ 99 % pure
Nitric acid:	HNO_3, Merck, 65 % pure
Magnesium dichloride:	$MgCl_2 \cdot 6H_2O$, Merck ≥ 99.0 pure
Hydrochloric acid:	HCl, Fluka, 32 %
Sodium chloride:	NaCl, Merck, ≥ 99.5 %

3.1.2. Synthesis of monazite-type powder

Monazite-type ceramic samples *RE*PO_4 were prepared by hydrothermal synthesis at 200 °C. This synthesis route partly followed the route described by Meyssamy et al. [82]. The proportions in mmol and mL are given for a total of 250 mL solution.

$La(NO_3)_3 \cdot 6H_2O$ (30 mmol) was dissolved in water (50 mL, solution #1) and poured into NaOH (100 mL, 1 mol·L^{-1}, solution #2). Afterwards, an aqueous solution of $(NH_4)_2HPO_4$ (27 mmol or 30 mmol in 100 mL water, solution #3) was added. The mixture was adjusted to pH = 12.5 using NaOH (4 mol·L^{-1}) and poured into a Teflon beaker. The sample was heated up to 200 °C and this temperature was kept for two hours.

For technical reasons, the heat treatment at 200 °C was carried out within three different apparatuses: in a 35 mL Teflon beaker of a simple stainless steel autoclave (see Figure 19 left), in a 220 mL Teflon beaker of a PARR Instrument GmbH autoclave (see Figure 19 right) or in a 120 mL Teflon beaker of a MLS GmbH microwave.

Table 8: Comparison of the working conditions of the PARR autoclave and the MLS microwave

PARR autoclave	MLS microwave
- From RT to 200 °C in 50 min	- From RT to 100°C in 5 min
- 120 min-stay at 200 °C	- From 100 to 200°C in 7 min
Pressure: 10 to 15 bar	- 120 min-stay at 200 °C
- From 200 °C to 75 °C in 120 min	- 25 min cooling

The resulting suspension was centrifuged. In order to dissolve lanthanum hydroxide formed by the excess lanthanum ions under the hydrothermal treatment, the precipitate was suspended in HNO_3 (100 mL, 0.1 $mol \cdot L^{-1}$) and stirred for three days. $LaPO_4$ is not soluble in dilute acids. The pH value of the suspension was readjusted to 1.0 with HNO_3 (1 $mol \cdot L^{-1}$). The white suspension was centrifuged. Next, the precipitate was washed with distilled water and dried at 95 °C over night. The reaction during the synthesis is as follows:

$$La(NO_3)_3 \cdot 6H_2O + (NH_4)_2HPO_4 \rightarrow LaPO_4 + HNO_3 + 2NH_4NO_3 + 6H_2O \quad (3)$$

Figure 19: Simple autoclave composed of four components and the Teflon beaker with its top (left) and PARR autoclave with the pressure gage, the heater and the controller (right).

Doping

La-monazite samples were doped with a few ppm of Cm (III) and with Eu (III), respectively. The Eu content was 5 mol%, 20 mol%, 35 mol%, 50 mol%, 65 mol%, 80 mol% or 100 mol%. During the hydrothermal synthesis, $La(NO_3)_3 \cdot 6H_2O$ and $Eu(NO_3)_3 \cdot 6H_2O$ are added at the mol%-ratio desired in solution #1.

Samples synthesized for TRLFS measurements

La-monazite samples measured by TRLFS were synthesized following a slightly different route. La- and Eu-nitrate were synthesized by dissolving La- and Eu-oxide in 10 $mol \cdot L^{-1}$ HNO_3, and diluting the solution with supra-pure water.

Cm-doped $LaPO_4$ was synthesized by adding Cm solution ($2 \cdot 10^{-5}$ $mol \cdot L^{-1}$) to the La solution. The composition of the Cm (III) solution (20.0 µmol·L^{-1}) is 97.3 % ^{248}Cm, 2.6 % ^{246}Cm, 0.04 % ^{245}Cm, 0.02 % ^{247}Cm and 0.009 % ^{244}Cm in 1.0 $mol \cdot L^{-1}$ $HClO_4$.

3.1.3. Pressing and sintering of *RE*PO_4 pellets

In order to synthesize pellets, monazite powder was first calcinated at 350 °C, 500 °C or 950 °C for two hours. Powder (400 - 500 mg) was then pressed into cylindrical pellets of 10 mm diameter by cold uniaxial pressing at 64 - 765 MPa. The apparatus used here is an Oehlgass, Hahn & Kolb press. The $LaPO_4$ green pellets were sintered three hours at 1400 °C, and $La_{(1-x)}Eu_xPO_4$ (x = 0.2, 0.35, 0.5, 0.65, 0.80, and 1.0) green pellets were sintered for three hours at 1500 °C.

3.1.4. Physical properties of pellets

3.1.4.1. Density measurements

The green density ρ_g of the pellets was determined by the geometrical method:

$$\rho_g = \frac{4m}{\pi h D^2} \qquad (4)$$

Where m is the mass of the sample, D is the diameter of the sample, and h is the height of the sample.

The sintered density ρ_s was determined by hydrostatic weighing in water (Archimedes method):

$$\rho_s = \frac{m_1 \cdot \rho_p \cdot \rho_{H_2O}}{\rho_p \cdot (m_2 - m_3) - \rho_{H_2O}(m_2 - m_1)} \quad (5)$$

Where m_1 is the mass of the pellet, m_2 is the mass of the pellet covered with paraffin, m_3 is the mass of the pellet immersed in water, ρ_s is the sintered density of the sample, ρ_p is the density of the paraffin ($\rho_p = 0.9$), and ρ_{H_2O} is the density of water at room temperature ($\rho_{H_2O} = 0.9982$).

3.1.4.2. Vickers microhardness and fracture toughness

The microhardness of sintered pellets was measured by a diamond Vickers indenter. The apparatus is an Anton Paar MHT 10. The microhardness (H_V (GPa)) was determined by the following expression [91]:

$$H_v = 1852 \frac{F}{d_c^2} \quad (6)$$

Where F (N) is the load, and d_c (µm) is the average length of the diagonals of the Vickers indents.

The fracture toughness K_{Ic} (MPa·m$^{1/2}$) was determined with the indentation crack length method using the Anstis equation [91]:

$$K_{Ic} = 0.032\, H_v \cdot \sqrt{\frac{d_c}{2}} \sqrt{\frac{E}{H_v}} \left(2\frac{c_l}{d_c}\right)^{-1.5} \quad (7)$$

Where c_l (µm) is the average length of cracks, and E (GPa) is the Young modulus. The Young modulus of $LaPO_4$ was measured to be 133 GPa [92].

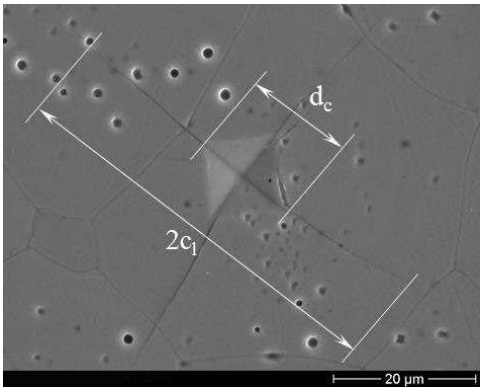

Figure 20: SEM-photography showing an indent and cracks on a ceramic due to the Vickers microhardness measurements. The average length of the diagonals d_c and the average length of the cracks c_l can be determined

3.1.5. Thermogravimetry coupled with differential scanning calorimetry

The thermal behavior of the dried powder was investigated from room temperature up to 1000 °C or 1300 °C by Thermogravimetry (TG) coupled with Differential Scanning Calorimetry (DSC) analysis in air atmosphere at a heating rate of 10 °C·min^{-1}. The measurements were performed with an apparatus from the company Netzsch, model STA 449C Jupiter.

3.1.6. Powder X-ray diffraction analysis

Powder X-ray diffraction is a long-range order method used to define the structure of a crystalline sample. The XRD patterns typically show the intensity of the Bragg reflections versus 2θ (diffraction angle). The structure analyses are carried out at room temperature. The analyses are performed with the D8 Advance, the D4 Endeavor from Bruker AXS GmbH, and the Stadi Transmissions Diffractometer from Stoe & Cie GmbH. The data were analyzed with the software “Match!” from Crystal Impact (version 1.106).

The program Topas was used for pattern indexing [93]. The lattice parameters (*a*, *b*, *c*) and the volume of the unit cell *V* are measured on $La_{(1-x)}Eu_xPO_4$ (x = 0.0, 0.2, 0.35, 0.5,

0.65, 0.8, 1.0). As the estimated standard deviations are underevaluated by Topas [93], these standard deviations have to be corrected by being multiplied by three [94].

The mean nanocrystallite size (L) and the lattice distortions (ε) were determined with XRD data (β, θ) by using the Hall-Williamson method [95]:

$$\frac{\beta \cdot cos(\theta)}{\lambda} = \frac{1}{L} + 4\varepsilon \cdot \frac{sin(\theta)}{\lambda} \qquad (8)$$

Where θ is the Bragg angle, λ is the wavelength of incident X-rays, and β is the peak half-width corrected to instrumental widening.

The values of the Bragg angle and the half-width of each Bragg peak are determined for each reflex. The values of $\beta \cdot \cos(\theta)$ are plotted versus $\sin(\theta)$. The experimental points were described by a linear dependence. The values of the interception point of the line with the ordinate and its slope serve to calculate L and ε respectively.

3.1.7. Raman spectroscopy

Raman spectroscopy is a short-range order method. It gives information about vibrational, rotational and other low frequency transitions between atoms [96]. The spectra are recorded with a Horiba Scientific LabRam HR Vis spectrometer. Here, Raman spectra were excited with a He-Ne laser (λ = 632.81 nm). The spectra are fit using Gaussian-Lorentzian profiles in order to determine the Raman peaks.

3.1.8. Scanning electron microscope

The morphology of the powders was investigated using a scanning electron microscope (SEM) (FEI model Quanta 200F). The SEM is coupled with an Energy-Dispersive X-ray Spectroscopy (EDS) equipment (EDAX model Genesis 4000), that permits to characterize the element distribution in a sample. The pellets were mirror polished and thermally etched at 1000 °C for investigations on the SEM.

3.1.9. Specific surface area measurements

The Brunauer, Emmett and Teller method (BET) is used for the measurement of the specific surface area of powder. Here, the calculation was realized with the adsorption of nitrogen molecules on the particles. The measurements were performed with a Quantachrome Autosorb apparatus.

3.1.10. Dilatometer

The shrinkage of the pellets occurring during the sintering was investigated by dilatometry (DIL 402C, Netzsch). The measurements were performed from room temperature up to 1400 °C with a heating rate of 5 °C·min^{-1}. The final density after the sintering in the dilatometer was determined by hydrostatic weighing in water (see sub-section 3.1.4.1). The relative density of the pellets during dilatometric experiments was calculated from:

[97] $$\rho(t) = \frac{(1+\frac{L_f - L_0}{L_0})(1+\frac{D_f - D_0}{D_0})^2}{(1+\frac{\Delta L(t)}{L_0})(1+\alpha\frac{\Delta L(t)}{L_0})^2}\rho_f \quad and \quad \alpha = \frac{(D_f - D_0)}{(L_f - L_0)}\frac{L_0}{D_0} \qquad (9)$$

Where L_0 is the initial thickness of the pellet, L_f is the final thickness of the pellet, D_0 is the initial mean diameter, D_f is the final mean diameter, $\Delta L(t)$ is the change in thickness of the sample, ρ_f is the final relative density, and α is the anisotropic shrinkage factor.

3.1.11. Inductive coupled plasma mass spectrometry

The Inductive Coupled Plasma Mass Spectrometry (ICP-MS) measurements were realized with the Elan 6100 DRC apparatus, developed by Perkin Elmer and SCIEX. The 10 mL samples are composed of 10 µL of solution to be analyzed, 100 µL of suprapure HNO_3, and the rest of suprapure H_2O.

The ICP-MS is a chemical analysis that counts the number of ions at a certain mass of the element. First of all the sample is introduced in the nebulizer and is converted into small droplets. They are carried through the spray chamber, the tube and then into the plasma, which ionizes the elements present in the droplets. These ions pass through the interface and are focused by the ions lens. The ions are separated by their mass-to-charge ratio in

the mass spectrometer and finally measured by the detector. The measured signal intensities are converted into concentrations of each element (by the computerized data system). A calibration curve is generated from the measurements of standards in order to compare them with the signals from unknown samples and to determine the concentration of each metal in the sample.

3.1.12. Aqueous durability tests

The resistance of monazite samples to corrosion was determined with static dissolution tests. Dissolution rates are determined on $La_{(1-x)}Eu_xPO_4$ samples (with x = 0.0, 0.2, 0.5, 0.8 or 1.0), synthesized with a molar ratio of (La, Eu):P = 1:1. Grain size was from 100 µm to 200 µm. The leached samples are prepared as shown on Figure 21.

For each of the five compositions, seven Teflon PFA beakers are filled in with ~ 10 mg of ceramic together with 25 ml leachate. The solubility of $LaPO_4$ and $EuPO_4$ were calculated with the GEMS program [98]. They are $1.84 \cdot 10^{-5}$ mol·L^{-1} and $1.19 \cdot 10^{-5}$ mol·L^{-1} respectively, so that the experiments start in under saturation. The tests are realized in acidic media, due to the high resistance of monazite ceramics to leaching. The leachate is a NaCl solution (0.1 mol·L^{-1}) acidified with HCl up to pH = 2. The ionic strength is of 0.1. The Teflon PFA beakers are placed in a shaking oil bath at 90 °C (see Figure 22).

The tests run over a period of one month (28 days). At given intervals, a small amount of leachate is pipetted and filtered with Anotop 25-Plus filter, which have a pore size of 0.02 µm and a diameter of 25 mm. Neither La nor Eu are adsorbed by these Anatop filters. After the filtration, the leachates are analyzed by ICP-MS (see section 3.1.11) to determine the concentration (mg·L^{-1}) of La and Eu, respectively. Considering the error due to ICP-MS and the pipetting, the minimum marge of error is of 10 %.

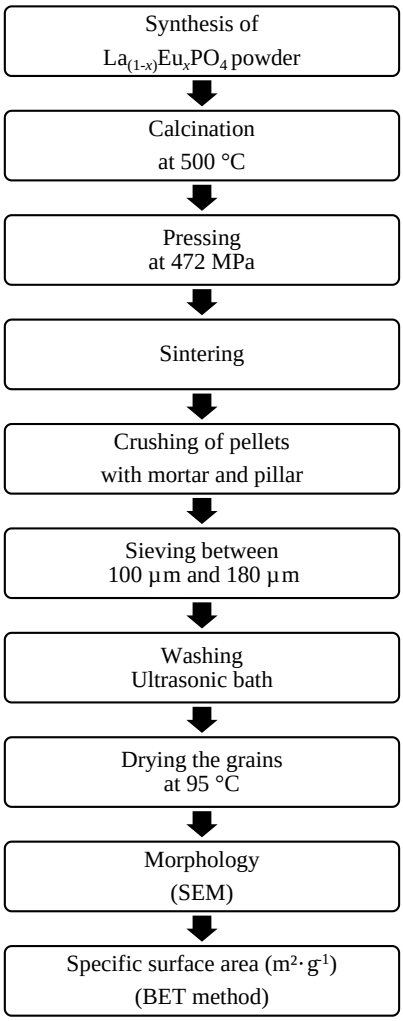

Figure 21: Flow chart representing the synthesis of $La_{(1-x)}Eu_xPO_4$ for aqueous durability tests.

In order to compare the aqueous durability of La and Eu within the monazite matrix, the normalized weight loss $N_L(i)$ ($g \cdot m^{-2}$) is calculated with the measured concentrations ($mg \cdot L^{-1}$). It is assumed that during the time of the experiment, the mass and the surface of the sample stay the same [99]. In the case of static experiments, the normalized weight loss is determined as follows:

[100] $$N_L(i) = \frac{m_i}{f_i \cdot S} \quad and \quad f_i = \frac{mol\%\ of\ i \cdot molar\ mass\ of\ i}{total\ molar\ mass\ of\ La_{(1-x)}Eu_xPO_4}$$ (10)

Where i is the measured element (La or Eu), m_i is the total amount of i measured in solution (g), S is the effective surface area of the sample in contact with the solution, and f_i is the mass ratio of the element i in the solid.

The normalized dissolution rate R_L ($g \cdot m^{-2} \cdot d^{-1}$) is the mass loss of the dissolved solid per time and surface units. It is the derivative of the normalized weight loss N_L ($g \cdot m^{-2}$) with respect to time:

[100] $$R_L(i) = \frac{dN_L(i)}{dt} = \frac{1}{f_i \cdot S} \cdot \frac{dm_i}{dt}$$ (11)

Where i is the measured element (La or Eu), m_i is the total amount of i measured in solution (g), S is the effective surface area (m^2) of the sample in contact with the solution, f_i is the mass ratio of the element i in the solid, and t is the time.

Figure 22: Shaking oil bath at 90 °C used for aqueous durability tests. Closed (left) and open (right).

3.1.13. Radiation tolerance tests by ion implantation

In accordance with the physical properties of La-monazite-type pellets (see section 3.1.4), $LaPO_4$ powder was synthesized by hydrothermal synthesis, calcined at 500 °C, pressed, and sintered during three hours at 1400 °C. The ion bombardment on ten La-monazite-type pellets simulating radiation damages was carried out with an Eaton NV 3204 ion implanter at the PGI-9 institute (Forschungszentrum Jülich GmbH). Three pellets were bombarded with Kr^{2+} ions at an energy of 400 keV.

La-monazite type ceramics have a very low critical amorphization temperature (see sub-section 2.3.2.2). In order to be able to observe the damages, $LaPO_4$ pellets have to stay at the temperature lower than T_c = 60 °C during and after the ion bombardment. The sample chamber of the ion implantation system at which the experiment was carried out has a cooling modulus working with liquid nitrogen. The temperature achieved was around -100 °C. After the experiments, samples were conserved in a freezer at a temperature lower than 0 °C. The damages were analyzed by Raman spectroscopy. During the Raman measurements, the sample was put on a copper plate cooled down by a cooling bath. The cooling bath was composed of 21.25 g magnesium dichloride hexahydrate and 25 g ice [101].

3.1.14. Time resolved laser fluorescence spectroscopy

The experiments were performed in the Institute for Nuclear Waste Disposal (INE) of the Karlsruhe Institute of Technology (KIT). Pictures taken in the TRLFS laboratory show the optical set-up and the sample emitting light on Figure 23.

Figure 24 schematically shows the experimental set-up used for TRLFS measurements. In practice, the experimental set-up is composed of an excimer laser, dye cuvettes, polarizers, the sample chamber, a camera and a computer system. The measurement occurs with a pulse of laser, the exposure time being shorter than the decay time of the material [61]. The laser has a given wavelength, which can be adjusted by a dye. The dye Qui is utilized to obtain UV light [61]. Rhodamine 6G is used for direct excitation of Eu, and Rhodamine B for direct excitation of Cm [61]. While the emitted light from the dye cuvettes passes through the polarizer, the power can be adjusted. Afterwards the light is focused on the sample. The sample is kept in a sample chamber under vacuum and cooled to achieve temperatures under 20 K for a high resolution of the spectra. The camera catches the light emitted by the sample starting from a certain time after the pulse of light was sent from the laser. The delay until the camera opens is called “step”. These measurements are repeated more than hundred times. The signals caught by the camera are transmitted to the computer.

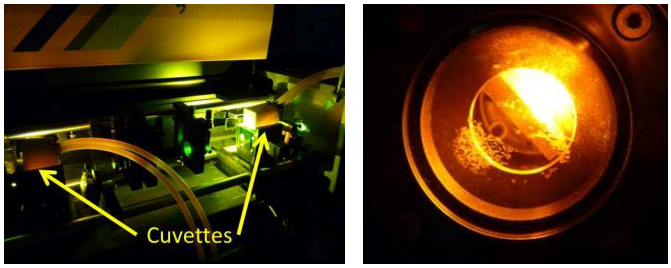

Figure 23: TRLFS experimental set-up: optical set-up with the dye cuvettes (left), and a sample emitting light (right).

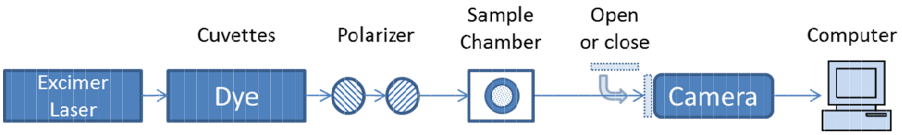

Figure 24: Schema of a TRLFS experimental set-up.

The Eu- and Cm-doped La-monazite powder for the samples was synthesized as explained before (see section 3.1.2). Samples were analyzed before (as prepared) and after 48 hours calcination at 1000 °C to obtain a better crystallinity of the samples and better signals.

3.1.15. Extended X-ray absorption fine structure

X-ray Absorption Fine Structure (XAFS) is an element specific short-range order spectroscopic method based on the absorption of X-rays by matter through the photo-electric effect. In this process, an X-ray photon is absorbed by an electron in a tightly bound core level of an atom. The change in the absorption coefficient is recorded as a function of the incident radiation and permits to give information about the local chemical environment (up to 6 Å) of a probed atom. The X-ray absorption spectrum is typically divided into two regimes: the X-ray Absorption Near Edge Structure (XANES) and the Extended X-ray Absorption Fine Structure (EXAFS) domains.

As the material is irradiated with X-rays, an absorption edge is induced when the incident energy matches the binding energy of core-level electrons. At higher energies, this absorption causes the ejection of a photoelectron into the continuum, which will interact

with the neighbor atoms causing interference signals [102]. The effects observed in the edge region correspond to the XANES domain, from which information about valence and coordination geometry can be obtained. The EXAFS part of the spectrum is related to the interferences at higher energies (from 70 eV to 1000 eV above the edge) and is used to give information about interatomic distances as well as number and type of nearest neighbors.

XAFS is applicable to almost all elements of the periodic table, except the lightest ones, in condensed matter (solids, liquids, interfaces, etc.). Unlike XRD, crystallinity of the sample is not required for XAFS measurements. The source is often a synchrotron particle accelerator, because it generates high-quality (flux and brilliance) X-ray radiation. Several synchrotron light sources are available in Europe, e.g. ANKA in Karlsruhe (Germany) [103] and ESRF in Grenoble (France) [104]. In this work, measurements were performed at the INE-Beamline for actinide research at ANKA [105] (Karlsruhe Institute of Technology, campus north), which is operated by the Institute of Nuclear Waste Disposal (INE).

Eu (III) L_3-edge EXAFS spectra were recorded for the $La_{0.95}Eu_{0.05}PO_4$ powder in fluorescence yield detection mode. The energy calibration was carried out by setting the K-edge of a Fe foil at 7112 eV. Several scans were merged to improve the signal to noise ratio by using the Athena interface [106] to the Ifeffit software, and the Fourier transform was obtained from the $k_3 \cdot \chi(k)$ function. The spectrum was fit in R-space by using phase and amplitude function calculated with feff 6 [107] with the Artemis interface [106] to the Ifeffit software.

4. Results and discussion

The aim of this study is to define the ability of La-monazite as host matrix for the immobilization of minor actinides. The main properties required for this purpose are the incorporation of doping elements on regular atomic positions within the crystal structure, and the stability of the doped ceramic.

Chapter 4.1, Characterization of monazite-type powder (p. 53), analyzes the thermal behavior, the structure, and the morphology of La-monazite powder synthesized by hydrothermal route. Then, the incorporation of the Eu or Cm as dopant in La-monazite is analyzed by spectroscopic methods. TRLFS and EXAFS serve the understanding of the sample structure at a molecular level. TRLFS is used to explore the local structural environment of Eu and Cm. EXAFS quantifies the distances between Eu and its neighbors, in terms of distance and coordination number.

Chapter 4.2, Characterization of monazite-type pellets (p. 81), investigates the physical properties of monazite pellets. The optimal pressure corresponding to the highest density is obtained via the study of compressibility and sinterability. Dilatometric results permit to analyze the material behavior during sintering.

Finally, chapter 4.3, Resistance to corrosion and to irradiation (p. 92), evaluates the stability of monazite samples by applying aqueous durability tests and radiation tolerance tests. Here, leaching tests are done in an acidic media at 90 °C on Eu-doped $LaPO_4$. Radiation tolerance is tested on La-monazite pellets. The samples are subjected to ion bombardment and measured by Raman spectroscopy before and after the implantation.

4.1. Characterization of monazite-type powder

4.1.1. Thermal behavior of La-monazite-type powder by means of TG-DSC measurements

The thermal behavior of $LaPO_4$ powder is investigated from room temperature up to 1300 °C by TG coupled with DSC. Figure 25 shows the weight loss (%) of a sample (left axis, blue curve) and the DSC signal (right axis, green curve). Figure 26 shows the comparison of TG (left axis, blue curve) and the derivative of TG with respect to temperature (right axis, light blue curve).

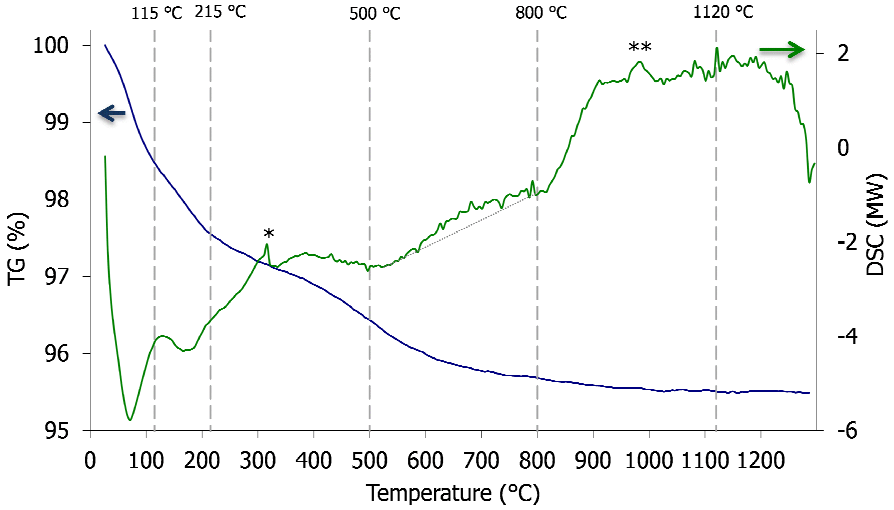

Figure 25: TG-DSC measurement on La-monazite powder.

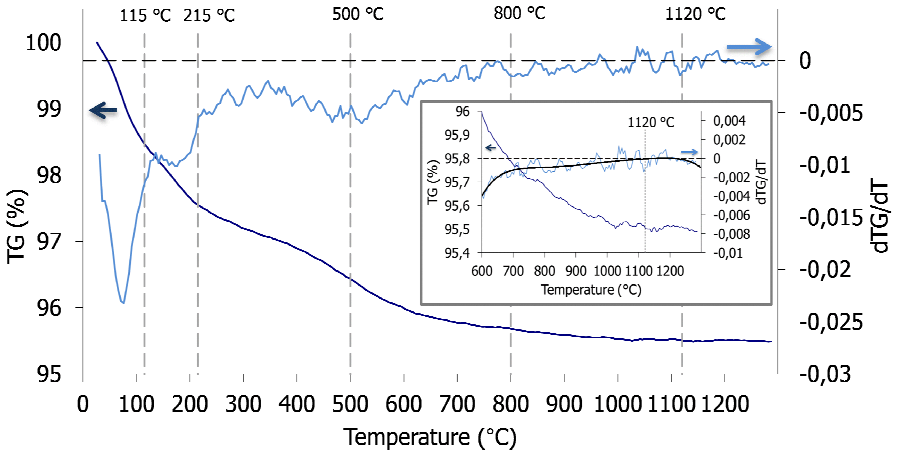

Figure 26: TG and dTG/dT curves of La-monazite powder. Inset: zoom-in of the graph from 600 °C to 1300 °C.

The total mass loss of approx. 4.5 % shown by the TG curve as well as the exothermic and endothermic peaks shown by the DSC curve result from the reactions occurring within the sample during thermal treatment. The behavior of the sample was compared with La-monazite-type samples found in the literature [35; 108-110]. Five distinct temperatures are shown on Figure 25 and Figure 26 defining zones of interest: 115 °C, 215 °C, 500 °C, 800 °C, and 1120 °C.

A broad endothermic peak is observed from room temperature up to 900 °C. It is likely to be related to the main release of water.

The hygroscopic properties of phosphates lead to adsorption of water from air. Between room temperature and 115 °C, an endothermic peak is observed at 65 °C. It reveals the evaporation of adsorbed water, associated with a weight loss of approx. 1.5 %.

At temperatures between 115 °C and 215 °C, the endothermic peak observed at 160 °C is related to the elimination of NH_4 impurities, yielding a weight loss of approx. 0.9 %. It corresponds to the following endothermic transformation:

[111] $$NH_4NO_3 \rightarrow NH_3 + HNO_3 \quad (12)$$

At temperatures between 215 °C and 480 °C, a weight loss of approx. 0.9 % as well as an exothermic peak at 315 °C (*) are observed. These phenomena are related to the following exothermic reaction occurring in the sample:

[111] $$NH_4NO_3 \rightarrow N_2 + 2\,H_2O + \tfrac{1}{2}\,O_2 \quad (13)$$

After the hydrothermal synthesis the sample is mainly composed of La-monazite and its hydrated form La-rhabdophane ($LaPO_4 \cdot 0.5H_2O$), which is likely to be included as secondary phase. At temperatures between 500 °C and 800 °C, a low and broad exothermic peak is associated with the irreversible phase transformation from hexagonal to monoclinic structure (from rhabdophane to monazite) [109].

At temperatures between 800 °C and 1120 °C, the cause of the exothermic peak at 971 °C (**) is more questionable. In the work of Lucas and co-workers [109; 110], an endothermic peak at about the same temperature was observed during the study of thermal behavior of $LaPO_4 \cdot H_2O$. The peak is observed either at 1000 °C or at 950 °C in

[109] and [110], respectively. In both articles, the exothermic peak is attributed to the formation of $La(PO_3)_3$ as secondary phase.

Here, the La:P ratio (53:47) corresponds to 28 wt.% of P_2O_5 on the La_2O_3-P_2O_5 phase diagram (Figure 17). If a secondary phase should occur, it would be a La-richer phase than $LaPO_4$. La_3PO_7 could be a secondary phase. Park described the phase transformation at 935 °C of α-La_3PO_7 (low-temperature phase) into β-La_3PO_7 (high-temperature phase) [112]. Therefore, the exothermic peak at 971 °C (**) is assumed to be due to this α-β phase transformation. Nevertheless this phase transformation is not reported in any other publications. There is a lack of recent studies about the La_2O_3-P_2O_5 phase diagram in general and about La_3PO_7 in particular. Further investigations are necessary in order to confirm the hypothesis of presence of La_3PO_7 in the material. Another hypothesis for the exothermic peak (**) could be the start of the crystallization of $LaPO_4$ from 950 °C on.

The value of the fifth remarkable temperature was estimated at approx. 1120 °C by the first derivative of the TG curve (see inset on Figure 26). At temperatures above 1120 °C, the last OH-groups are eliminated thus leading to the end of the weight loss. The DSC curve shows instability, which is likely to be related to the acceleration of crystallization up to 1300 °C.

4.1.2. Structure analysis of monazite-type powder by means of X-ray diffraction

The aim of the monazite-type powder analysis by means of XRD is to verify that the synthesized samples have the monoclinic structure of La-monazite and to analyze the purity of the phase. As assumed in the previous section, traces of La_3PO_7 may be present.

Five La-monazite powders were also analyzed after a thermal treatment at five different temperatures (T_1 to T_5 respectively, see Table 8) from drying temperature (95 °C) up to sintering temperature (1400 °C). The sizes of the nanocrystallite as well as the microstrain are investigated.

Moreover, lattice parameters of Eu-doped $LaPO_4$ ($La_{1-x}Eu_xPO_4$, with $x = 0$ to 1) were calculated and the values obtained are compared to the Gd-doped $LaPO_4$ ($La_{1-x}Gd_xPO_4$ with $x = 0$ to 1) values found in the literature [42]. The correlation between the lattice parameters and the percentage of dopant within the crystal structure is discussed.

4.1.2.1. Structure analysis of La-monazite-type powder sintered at 1300 °C

The diffraction data of La-monazite powder sintered at 1300 °C, together with the $LaPO_4$ and La_3PO_7 reference data are shown on Figure 27 (a) and (b) (intensity versus 2θ). The sample (black curve) matches with the indexed Bragg reflections of the reference (blue peaks, data PDF 2, reference n° 00-032-0493). Hence it confirms that the sample mainly contains $LaPO_4$. However, on Figure 27 (b), Bragg peaks can be referred as La_3PO_7 phase (red peaks, data PDF 2, reference n° 00-049-1023), in particular at $2\theta = 12.9°$, at $2\theta = 22.4°$ and at $2\theta = 43.7°$. Thus, this oxyphosphate phase is present as impurity within the La-monazite sample. As assumed before, the exothermic peak (**) seen at 971 °C on Figure 25 is due to the La_3PO_7 phase transformation.

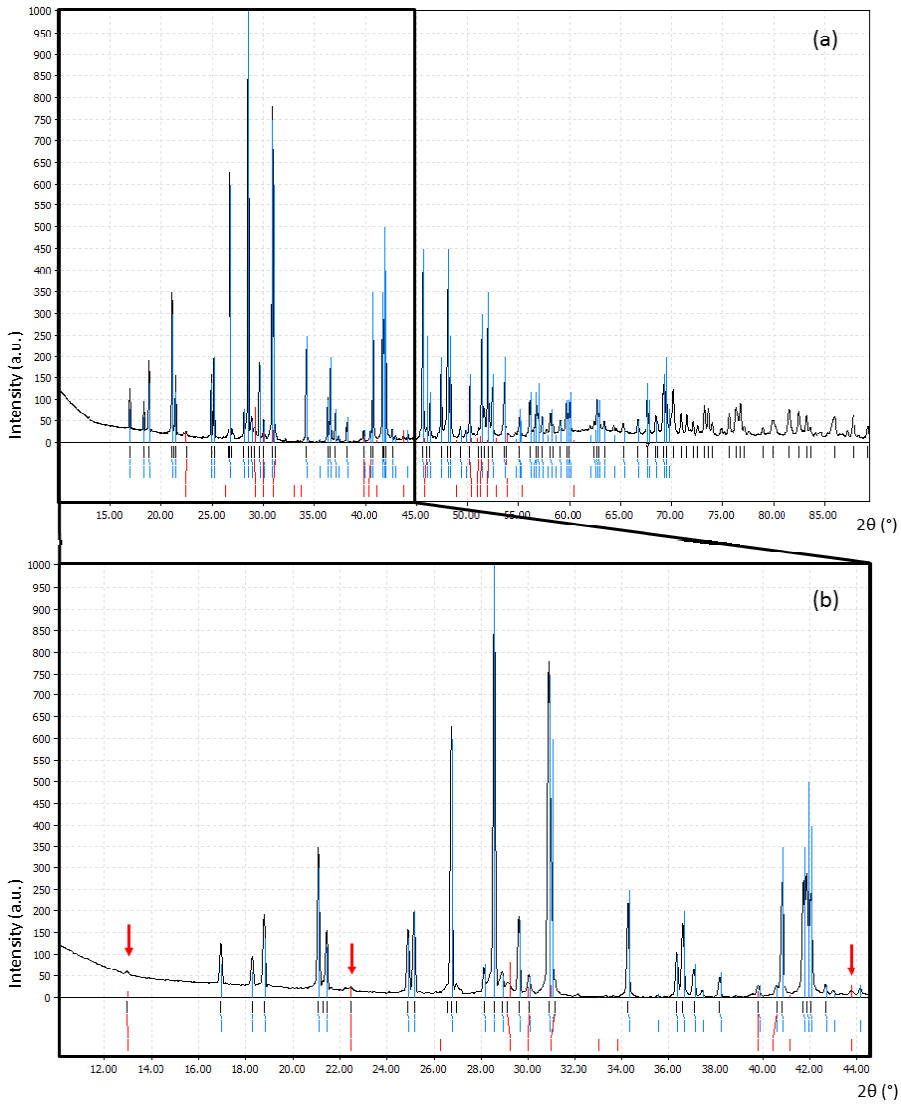

Figure 27: XRD pattern (from 0° to 90°) of $LaPO_4$ sintered at 1300 °C (black) together with reference data of $LaPO_4$ (blue) and La_3PO_7 (red) (a), and its zoom in (from 0° to 44°) (b).

4.1.2.2. Effects of a thermal treatment on La-monazite samples

In order to study the evolution of the structure with the temperature, La-monazite samples were subjected to a thermal treatment at five different temperatures, given in Table 9:

Table 9: Calcination temperatures of $LaPO_4$ powder being measured by XRD.

T_1	T_2	T_3	T_4	T_5
95 °C	350 °C	500 °C	950 °C	1400 °C

The powders are analyzed by XRD and the sizes of the nanocrystallite (L) as well as the microstrain of crystal lattice (ε) are investigated. The calcination temperatures were chosen based on the thermal behavior of the La-monazite sample (see section 4.1.1):

- T_1 corresponds to the drying temperature within the synthesis method of $LaPO_4$.
- At $T = T_2$: adsorbed water and impurities are eliminated.
- At $T = T_3$: the hexagonal to monoclinic transformation has not taken place yet.
- At $T = T_4$: the hexagonal to monoclinic transformation has taken place already.
- T_5 is the sintering temperature of La-monazite pellets (see section 3.1.3).

X-ray diffraction pattern

Figure 28 (a), (b) and (c) show the XRD patterns of $LaPO_4$ powder calcined at T_1 to T_5 respectively. No significant differences are observed between the patterns of the T_1, T_2 and T_3 samples (Figure 28 (a)). Figure 28 (b) shows the results after calcination at T_3 and T_4. The peaks are sharper after calcination at 950 °C than calcination at 500 °C, i.e. the peak half-width has decreased. It is likely to be related to the beginning of the crystallization of the sample. Figure 28 (c) shows the results after calcination at T_4 and T_5. The peaks are even sharper at 1400 °C than at 950 °C, since the crystallinity increases with temperature.

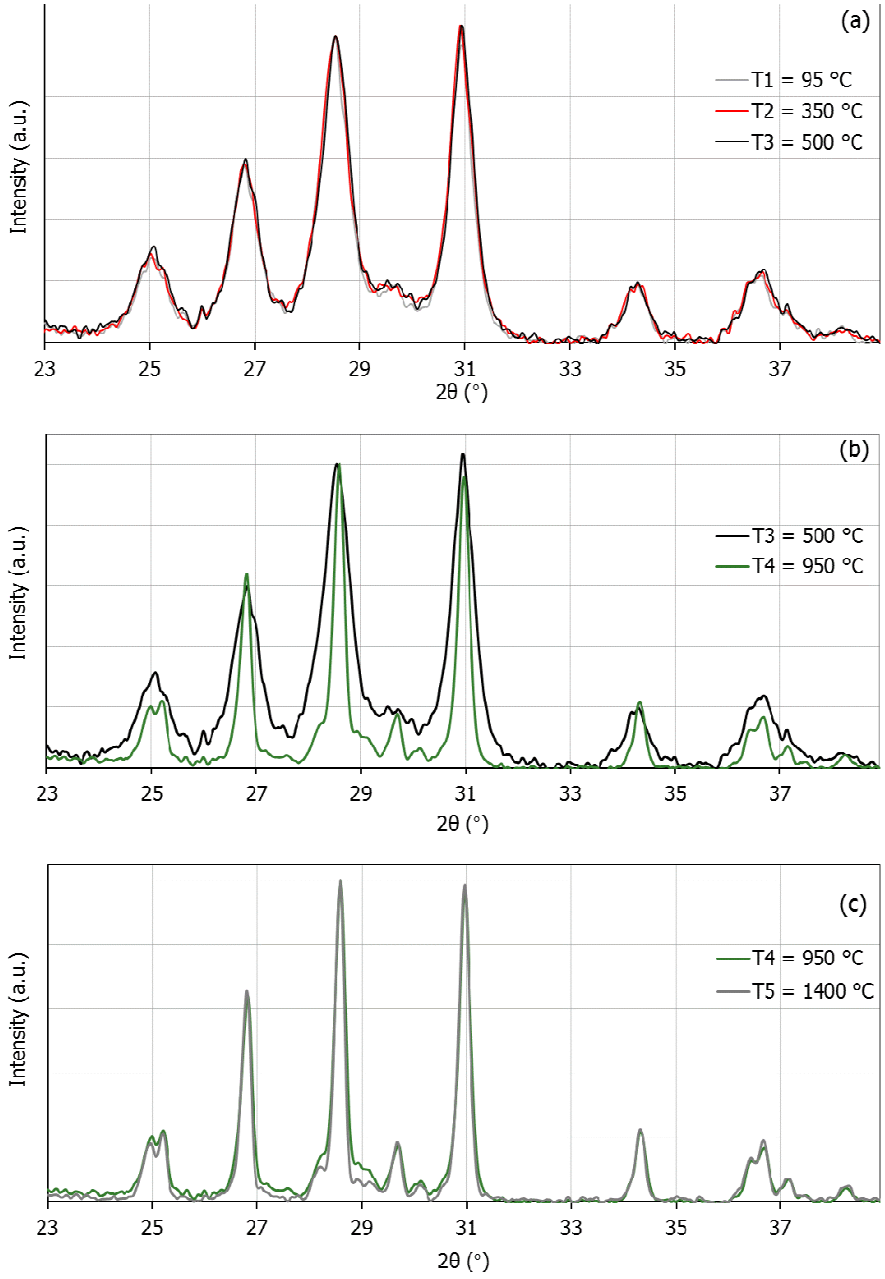

Figure 28: XRD patterns of La-monazite powder after a thermal treatment at T_1, T_2, T_3 (a), T_3, T_4 (b), and T_4, T_5 (c).

Evolution of the crystal structure with the calcination temperature of La-monazite

The mean nanocrystallite size L and the distortions of the lattice ε were calculated by the Hall-Williamson method. Figure 29 shows the representation of $\beta \cdot \cos(\theta)/\lambda$ versus $\sin(\theta)/\lambda$, calculated with the XRD data (i.e. the Bragg angle θ and the corrected peak half-width β) of La-monazite calcined at T_1 to T_5 respectively. Afterwards, a simple linear regression permits to deduce the mean nanocrystallite size as well as the lattice distortion (see equation (8)). The results are shown on Table 10 and Figure 30.

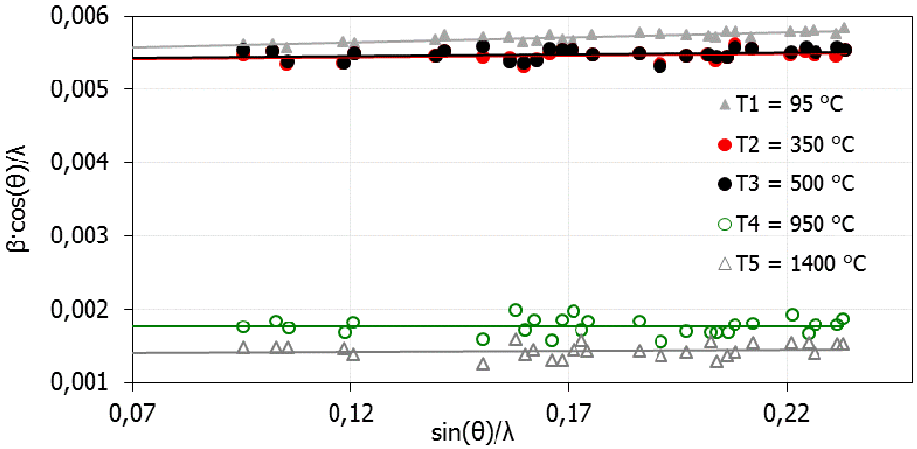

Figure 29: Representation of the Hall-Williamson method applied on La-monazite calcined at T_1 to T_5, respectively.

After the drying at 95 °C as well as the calcination at 350 °C or 500 °C of the powder, the nanocrystallite size is about 18.5 nm (Table 10), which is likely to be the size of primary particles. The mean nanocrystallite size L largely increases with the temperature, from 18.5 nm up to 57.0 nm after calcination at 950 °C, which leads to the assumption that the crystallization process begins at T > 500 °C. Then, the sintering of the material at 1400 °C results in an increase of the nanocrystallite size up to 73 nm.

The lattice distortions have a large standard deviation, so that the evolution tendency is not as precise. However, a decrease trend of the lattice distortion is noticed on Figure 30, from 0.03 % at 95 °C to 0.01 % at 1400 °C. The higher value at 95 °C is due to the presence of OH-groups in the matrix before thermal treatment (water of crystallization of

La-rhabdophane). At high temperature, the crystallization of the ceramic reduces the lattice distortion to approximately zero.

The mean size of the nanocrystallite *L* obtained with the Hall-Williamson method is compared to the particle size *D* obtained on the same sample from BET measurements (see Figure 31 and Table 10). Assuming that the particles are spherical, the mean particle size *D* is calculated as follows:

$$D[nm] = 1000\frac{6}{S \cdot \rho} \qquad (14)$$

Where ρ is the density of $LaPO_4$ (5.11 $g \cdot cm^{-3}$ [database PDF 2, n° 00-084-0600]), and *S* is the specific surface area [$m^2 \cdot g^{-1}$].

Table 10: Distortion (ε) and mean nanocrystallite size (*L*) determined by the Hall-Williamson method and the mean particle size (*D*) determined by BET measurements of La-monazite powder calcined at T_1 to T_5, respectively.

Temperature	ε (%)	*L* (nm)	*D* (nm)
T_1 = 95 °C	0.03	18.3	14.9
T_2 = 350 °C	0.01	18.6	16.3
T_3 = 500 °C	0.01	18.5	18.6
T_4 = 950 °C	0.00	57.0	241.6
T_5 = 1400 °C	0.01	72.7	346.4

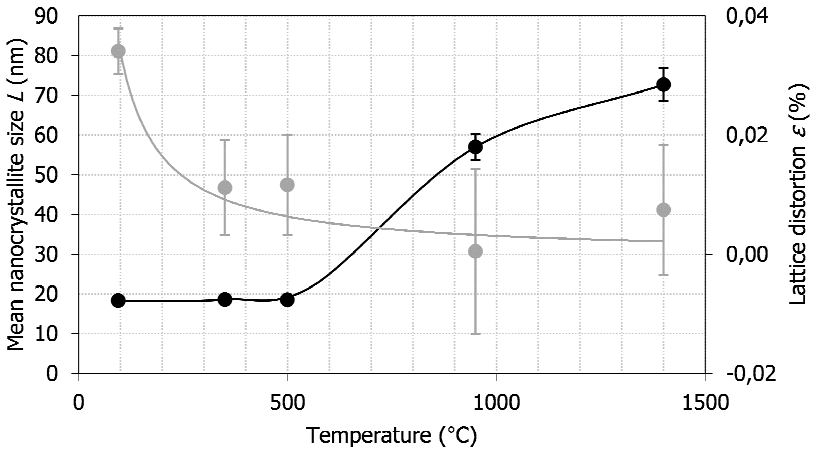

Figure 30: Mean nanocrystallite size *L* (black) and lattice distortion ε (grey) of La-monazite powder versus thermal treatment temperature (T_1 to T_5).

From room temperature up to 500 °C, the particle size coincides with the nanocrystallite size. At temperatures above 500 °C, the process of material crystallisation begins and leads to an increase of both the nanocrystallite and the particle sizes. At 950 °C, *D* (241.6 nm) is more than four times higher than *L* (57.0 nm). At 1400 °C, *D* (346.3 nm) is even almost five times higher than *L* (72.7 nm). After a sintering at 1400 °C it is assumed that the particles have a size of approx. 400 nm and consists of nanocrystallites of approx. 70 nm.

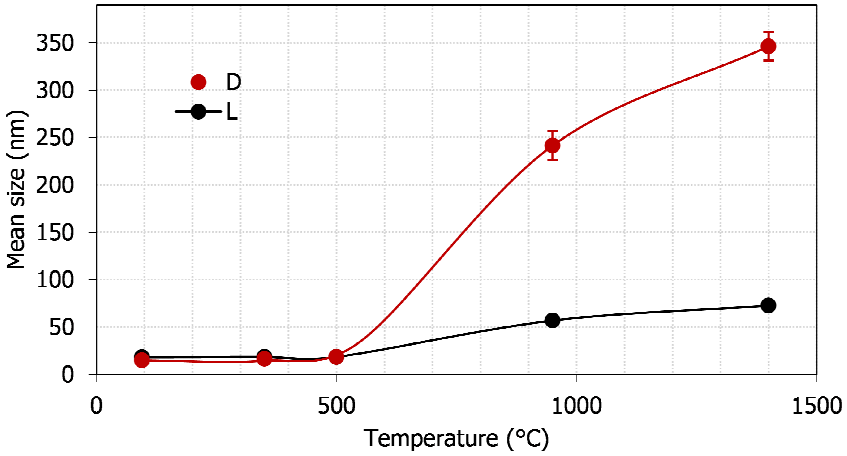

Figure 31: Evolution with the temperature of the size of the nanocrystallites measured by the Hall-Williamson method (*L*, black) and of the particles measured by BET method (*D*, red).

Morphology of La-monazite powder

The morphology of La-monazite particles dried at 95 °C was investigated by SEM. The size of the particles shown on Figure 32 variates from 1 to 20 µm. Figure 33 shows a photography at higher magnification, where round-shaped particles are observed. They are likely to be primary particles of 20 to 30 nm. This size is of the same order of magnitude as the values calculated by using both the Hall-Williamson and the BET methods after drying at 95 °C (see Table 10). It can be observed on Figure 33 that the particles tend to form aggregates of approx. 100 nm.

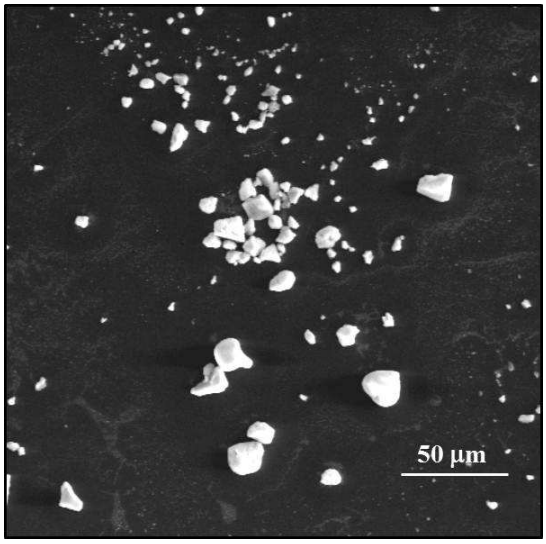

Figure 32: SEM-photography of La-monazite particles synthesized by hydrothermal route after drying at 95 °C.

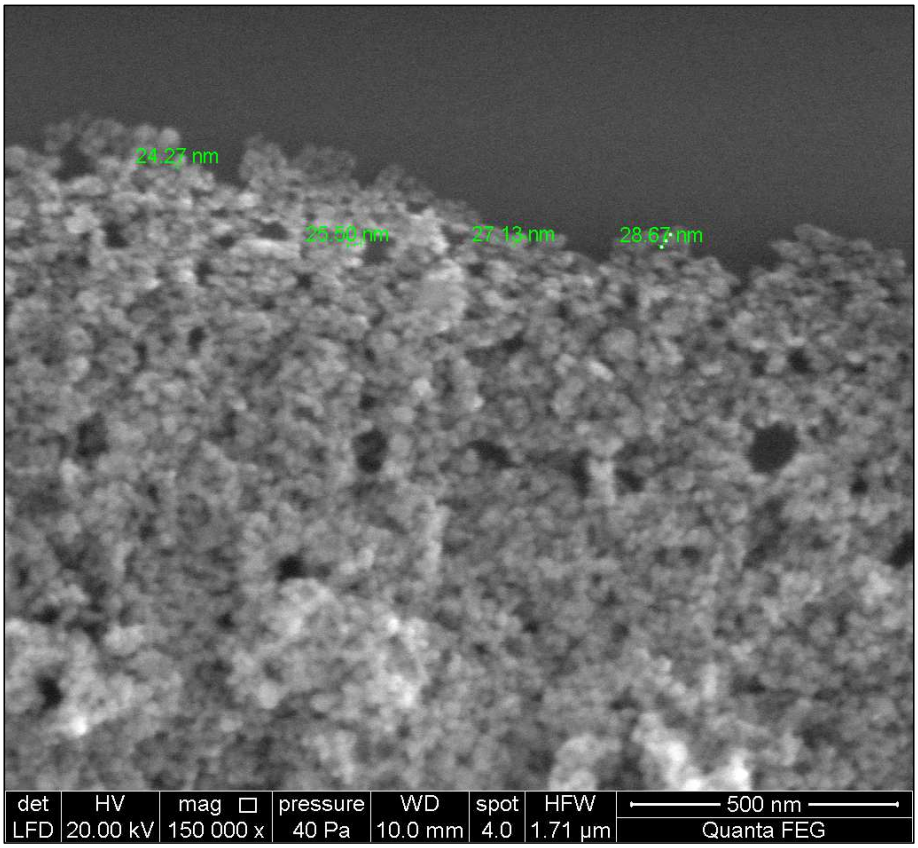

Figure 33: SEM-photography of La-monazite particles synthesized by hydrothermal route (drying at 95 °C), at a magnification of 150 000.

4.1.2.3. Effect of a dopant incorporated in the La-monazite crystal structure

Table 11 shows the lattice parameters (*a*, *b*, *c*) and the volume of the unit cell (*V*) of seven compositions of Eu-doped $LaPO_4$ samples measured with the Topas software [93]. There has been no data about the lattice parameters of Eu-doped $LaPO_4$ in the literature so far. In the context of the study, the data will be compared to Gd-doped $LaPO_4$.

The parameter difference of $LaPO_4$ and $EuPO_4$ is about 2.53 %, 2.93 %, 2.42 % and 7.94 % for *a*, *b*, *c*, and *V*, respectively. The decrease of the lattice parameters *a*, *b*, *c*, and *V* is likely to be related to the progressive replacement of La by Eu in the crystal

structure. It suggests the existence of a regular solid solution (La, Eu)PO_4 between the end members $LaPO_4$ and $EuPO_4$.

Table 11: Lattice parameters (*a*, *b*, *c*, ß) and volume *V* of the unit cell of $La_{(1-x)}Eu_xPO_4$. The error is given in parenthesis.

x	*a* (Å)	*b* (Å)	*c* (Å)	*β* (°)	*V* (Å³)
0.00	6.8408(2)	7.0753(2)	6.5120(2)	103.285(2)	306.75(1)
0.20	6.8072(2)	7.0364(2)	6.4838(1)	103.437(1)	302.06(1)
0.35	6.7907(3)	7.0163(3)	6.4690(3)	103.488(3)	299.72(2)
0.50	6.7560(3)	6.9761(3)	6.4379(3)	103.630(3)	294.87(2)
0.65	6.7348(3)	6.9477(3)	6.4186(3)	103.703(3)	291.79(2)
0.80	6.7034(4)	6.9119(4)	6.3885(4)	103.823(4)	287.43(3)
1.00	6.6677(4)	6.8679(4)	6.3544(4)	103.953(4)	282.40(3)

Comparison with the literature

The lattice parameters of $LaPO_4$ and $EuPO_4$ obtained here are compared with the works of Ni [113] and Terra [42] (see Table 12). For $LaPO_4$, the difference between this work and the work of Ni is about 0.14 %, 0.07 %, 0.13 %, and 0.01 % for *a*, *b*, *c*, and *β*. And for $EuPO_4$, the difference is about 0.10 %, 0.09 %, 0.08 %, and 0.007 % for *a*, *b*, *c*, and *β*. The values calculated in this work are in good agreement with the values found in the literature. The difference between the $GdPO_4$ lattice parameters published by Ni and Terra respectively (see Table 12) are not within the marge of error. The parameters show a difference of 0.14 %, 0.08 %, 0.05 %, and 0.02 % for *a*, *b*, *c*, and *β*. These relative errors are about the same order of magnitude than the difference between this work and the work of Ni.

The lattice parameters (*a*, *b*, *c*) and the volume of the unit cell *V* of Eu-doped $LaPO_4$ are compared with the values of Gd-doped $LaPO_4$ [42] on Figure 34 to Figure 37. Due to the lanthanide contraction (see section 2.4.1), Gd ($Z = 64$) has a smaller radius than Eu ($Z = 63$). The three cell parameters (*a*, *b*, *c*) of $GdPO_4$ are smaller than the ones of $EuPO_4$, thus, the unit cell of $GdPO_4$ is also smaller.

The results for the end members ($LaPO_4$ and $EuPO_4$) presented here are in good agreement with the literature, and the good incorporation of the dopant (here Eu) in the crystal structure can be assumed. The incorporation of Eu in the $LaPO_4$ lattice was investigated with TRLFS and will be discussed in the next section as well.

Table 12: Lattice parameters (*a*, *b*, *c*, *β*) of synthetic monoclinic $LaPO_4$, $EuPO_4$ and $GdPO_4$. The error is given in parenthesis.

Phases	*a* (Å)	*b* (Å)	*c* (Å)	*β* (°)	References
$LaPO_4$	6.8313(10)	7.0705(9)	6.5034(9)	103.27(1)	[113]
$LaPO_4$	6.837(1)	7.078(2)	6.507(2)	103.28(2)	[42]
$LaPO_4$	6.8408(2)	7.0753(2)	6.5120(2)	103.285(2)	This work
$EuPO_4$	6.6613(10)	6.8618(9)	6.3491(8)	103.96(1)	[113]
$EuPO_4$	6.6677(4)	6.8679(4)	6.3544(4)	103.953(4)	This work
$GdPO_4$	6.6435(9)	6.8414(10)	6.3281(6)	103.976(9)	[113]
$GdPO_4$	6.653(2)	6.847(2)	6.331(2)	103.96(2)	[42]

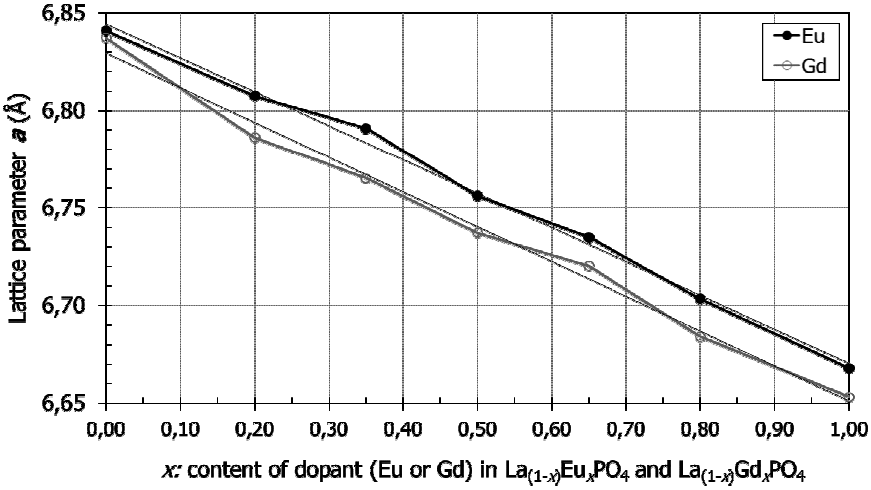

Figure 34: Lattice parameter a of $La_{(1-x)}Eu_xPO_4$ (x = 0.00, 0.20, 0.35, 0.50, 0.65, 0.80 and 1.00) compared with $La_{(1-x)}Gd_xPO_4$ (x = 0.00, 0.20, 0.35, 0.50, 0.65, 0.80 and 1.00) [42].

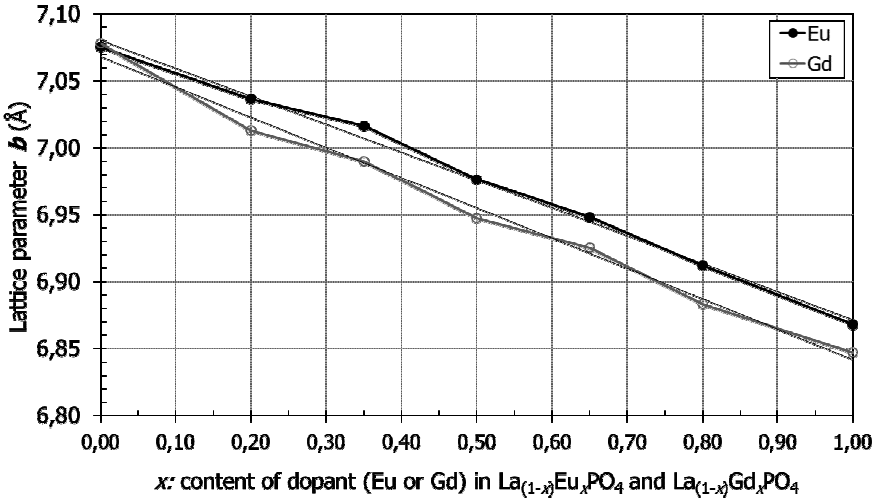

Figure 35: Lattice parameter b of $La_{(1-x)}Eu_xPO_4$ (x = 0.00, 0.20, 0.35, 0.50, 0.65, 0.80 and 1.00) compared with $La_{(1-x)}Gd_xPO_4$ (x = 0.00, 0.20, 0.35, 0.50, 0.65, 0.80 and 1.00) [42].

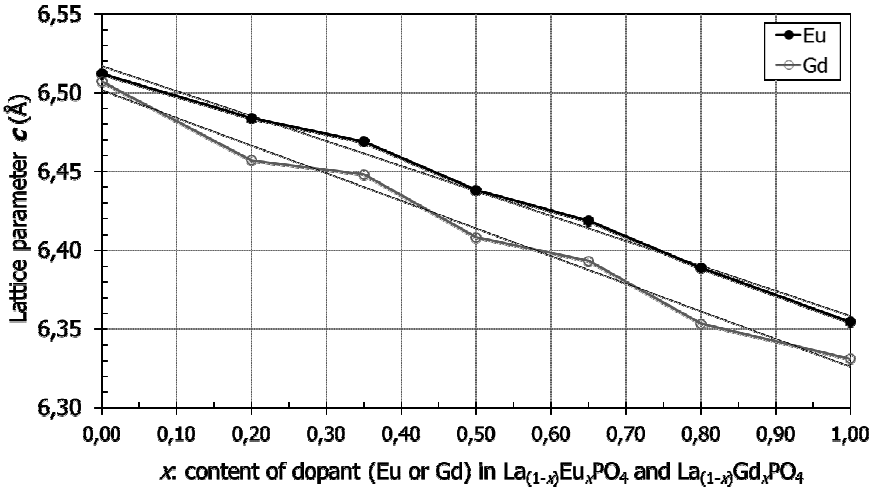

Figure 36: Lattice parameter c of $La_{(1-x)}Eu_xPO_4$ (x = 0.00, 0.20, 0.35, 0.50, 0.65, 0.80 and 1.00) compared with $La_{(1-x)}Gd_xPO_4$ (x = 0.00, 0.20, 0.35, 0.50, 0.65, 0.80 and 1.00) [42].

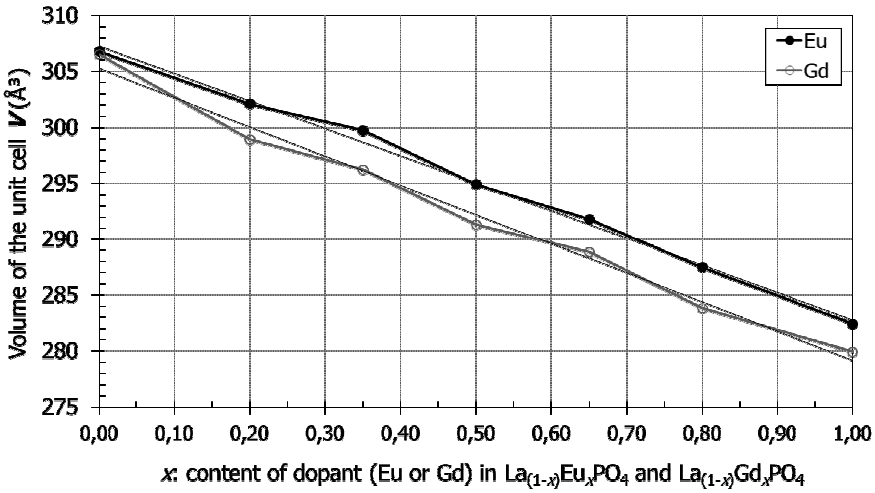

Figure 37: Volume of the unit cell of $La_{(1-x)}Eu_xPO_4$ (x = 0.00, 0.20, 0.35, 0.50, 0.65, 0.80 and 1.00) compared with $La_{(1-x)}Gd_xPO_4$ (x = 0.00, 0.20, 0.35, 0.50, 0.65, 0.80 and 1.00) [42].

4.1.3. Time resolved laser fluorescence spectroscopy

La-monazite is studied as potential host matrix for MA disposed in a long-term nuclear waste repository. The formation of a solid solution can be investigated at a molecular level with short-range order methods.

Here, Eu- and Cm-doped La-monazite were measured by TRLFS in order to analyze the incorporation mechanisms of a dopant in the crystal structure of La-monazite. Several authors have written about the luminescent properties of synthetic monazite when it is doped with Eu [82; 114]. However, there has been no data about Cm-doped $LaPO_4$ so far. The results discussed in this section are published by Holliday, Babelot et al. [115].

4.1.3.1. TRLFS measurements on Eu-doped $LaPO_4$ powder

Eu-doped $LaPO_4$ powder was analyzed by direct excitation. The $^7F_0 \rightarrow {}^5D_0$ transition was investigated directly while varying the excitation wavelength from 575 to 582 nm. As mentioned in the background (see sub-section 2.5.1.2), this transition is non-degenerate. As a consequence each Eu (III) environment presents a single peak in the excitation spectrum. The total number of Eu (III) species in a sample can be identified by these means.

Figure 38 shows the integrated fluorescence intensity versus the excitation wavelength (from 575 to 582 nm). At least two species can be identified: a major species excited at 578.4 nm and a minor species at 577.5 nm (shown with arrows on Figure 38). After the thermal treatment of the sample, the major species is still seen at 578.4 nm, whereas the minor species changes from 577.5 to 578.9 nm.

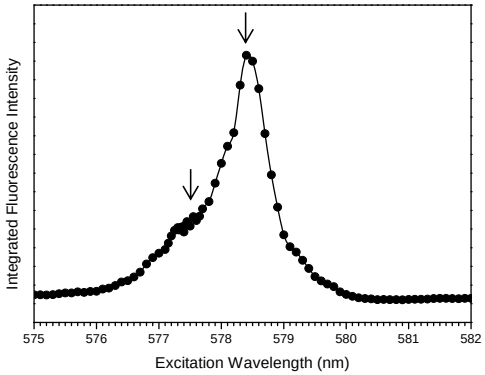

Figure 38: Excitation spectrum of Eu-doped $LaPO_4$ before thermal treatment. The $^5D_0 \rightarrow {}^7F_0$ transitions of both the major and minor species are indicated with arrows.

The lanthanide within the monazite-type structure is surrounded by nine oxygen elements positioned at nine different distances, respectively (see section 2.6.1),. As a result, the La site within La-monazite has a low symmetry (site symmetry C_1, i.e. identity).

Figure 39 shows a flow chart indicating the Eu luminescent transition and the corresponding peak number as well as the crystallographic point groups in Schoenflies notation. A Eu (III) ion showing a point group C_1 will show a three-fold splitting for the $^7F_0 \rightarrow {}^5D_1$ transition and a five-fold splitting for the $^7F_0 \rightarrow {}^5D_2$ transition.

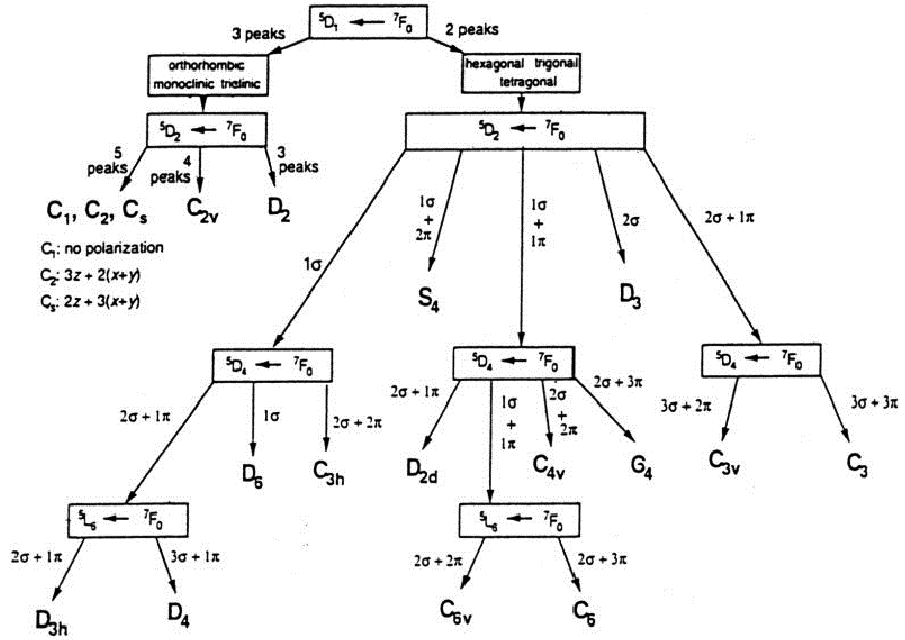

Figure 39: Flow chart for point group determination in single crystals, based on selected transitions in the Eu (III) ion [116].

As mentioned before (see sub-section 2.5.1.2), measurements carried out by direct excitation excite the species individually. Figure 40 shows the emission spectra of the major Eu species of Eu-doped $LaPO_4$ from direct excitation (before and after thermal treatment). The data published by Meyssamy et al. are indicated as vertical lines on Figure 40 (between 605 and 625 nm) and matches with the peaks of the sample after thermal treatment very well. The $^5D_0 \rightarrow {}^7F_0$ transition is measured at $\lambda = 578.4$ nm. As expected of an element that shows C_1 symmetry, (Figure 39), the $^5D_0 \rightarrow {}^7F_1$ shows a 3-fold degenerate splitting, and the $^5D_0 \rightarrow {}^7F_1$ transition a 5-fold splitting. Eu occupies the La site within the $LaPO_4$ crystal structure.

The spectra before and after thermal treatment show the same shape and no significant change. Eu is situated on the La site in both cases, even synthesized at a temperature as low as 200 °C.

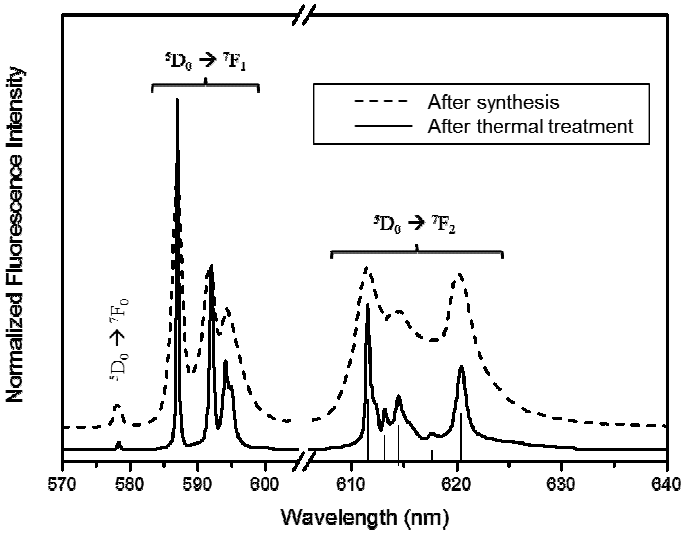

Figure 40: Emission spectra of the major Eu species of Eu-doped $LaPO_4$ from direct excitation (before and after thermal treatment). The contributions of the three main transitions are indicated.

A minor Eu species is also identified before and after the treatment at 1000 °C. Its excitation wavelength shifted from 577.5 nm to 578.9 nm, before and after thermal treatment, respectively. It shows a change of the Eu local environment. However, both emission spectra shows a 3-fold splitting of the $^5D_0 \rightarrow {}^7F_1$ transition from 585–605 nm and a 5-fold splitting of the $^5D_0 \rightarrow {}^7F_2$ transition from 605–635 nm in Figure 41. This indicates a low site symmetry of Eu (C_1), similar to the major Eu species. Nevertheless, the spectra are only clearly resolved after thermal treatment.

The presence of a minor Eu species could be caused by hydroxide interstitials in the La-monazite crystal structure, despite the acid treatment involved for the dissolution of $La(OH)_3$ during the synthesis process (see section 3.1.2). This hypothesis can be verified by the measurements of fluorescence lifetime of the minor Eu species. This approach allows determining the number of waters in the first coordination sphere of Eu.

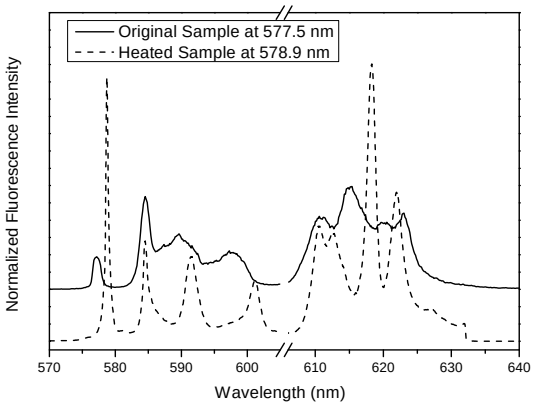

Figure 41: Emission spectra of the minor Eu species in Eu-doped $LaPO_4$ from direct excitation (before and after thermal treatment).

All Eu species are excited simultaneously by the normal UV excitation at 394.0 nm ($^7F_0 \rightarrow {}^5L_6$ transition). The fluorescence lifetimes for Eu were measured and the decay of the fluorescence was fitted for a bi-exponential decay with equation (15):

$$I_t = A_1 \exp(-k_1 t) + A_2 \exp(-k_2 t) \qquad (15)$$

Where I_t is the integrated fluorescence intensity at time t, A_1 is the quantity of species 1, A_2 is the quantity of species 2, k_1 (ms^{-1}) is the decay constant (or reciprocal observed lifetime) of species 1, and k_2 (ms^{-1}) is the decay constant (or reciprocal observed lifetime) of species 2.

If both Eu species are excited simultaneously, and if equal fluorescence intensity is assumed from both species, a relative abundance for each species can be calculated. The value corresponds to the ratio between the quantities A_1 and A_2. Direct excitation allows measuring the lifetime of each species separately. The decay constant is used in equation (1) to calculate the number of waters in the first coordination sphere of Eu. The data obtained from fluorescence decay measurements on Eu-doped $LaPO_4$, and the corresponding number of waters is summarized in Table 13. The major Eu species shows a long fluorescence lifetime before (5.2 ms) as well as after the treatment at 1000 °C (3.6 ms). The Horrocks equation indicates that no water is found in the first coordination sphere. The minor Eu species shows a shorter fluorescence lifetime than the major Eu

species. It is 0.95 ms before and 1.4 ms after the heat treatment. These lifetimes indicate that 0.5 and 0.1 waters are present in the first coordination sphere of Eu. The presence of a hydroxide interstitial is assumed. The number of waters decreased after the thermal treatment. It is supposed that water is lost during annealing. However, instead of OH-groups, O-atoms remain in the crystal structure.

Table 13: Relative abundance, fluorescence lifetime, and number of waters in the first coordination sphere, for both Eu species, before and after thermal treatment.

Eu-doped $LaPO_4$	Species	Relative Abundance (%)	Lifetime (ms)	n (H_2O)
Before thermal treatment	Major Eu site	70	5.2	0.0
	Minor Eu site	30	0.95	0.5
After thermal treatment	Major Eu site	70	3.6	0.0
	Minor Eu site	30	1.4	0.1

4.1.3.2. TRLFS measurements on Cm-doped $LaPO_4$ powder

In order to study the incorporation of a minor actinide within the crystal structure of La-monazite, $LaPO_4$ was doped with ^{248}Cm and measured by direct excitation, similarly as Eu-doped $LaPO_4$. The results for both samples will be compared. In the following, the $^8S_{7/2}$ - $^6D_{7/2}$ transition will be discussed.

The excitation spectrum of Cm-doped $LaPO_4$ before thermal treatment is shown on Figure 42. The ground state splitting that can be observed on the spectrum is not clearly resolved. Nevertheless, the major Cm species is found at 602.5 nm, and a shoulder indicates a minor Cm species at 601.7 nm.

The results are similar to the ones obtained for Eu-doped $LaPO_4$: the major species is at slightly lower energy than the minor species. As mentioned above (see sub-section 2.5.1.2), a free Cm ion shows an emission maximum at λ = 593.8 nm. Here, the strong complexation of Cm within the $LaPO_4$ crystal structure induces a red shift (higher wavelength) for the major Cm species (λ = 602.5 nm).

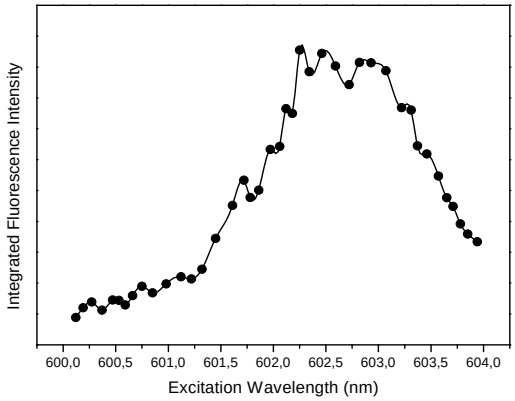

Figure 42: Excitation spectrum of Cm-doped $LaPO_4$ before thermal treatment.

As already measured for Eu-doped $LaPO_4$, the lifetimes were measured for Cm-doped $LaPO_4$. Cm was also excited by UV light (λ = 396.6 nm) in order to excite all species simultaneously. The Kimura's equation (see (2))) permits to relate linearly the decay constant to the number of waters in the first coordination sphere.

The data obtained from fluorescence lifetime measurements on Cm-doped $LaPO_4$, and the corresponding number of waters are summarized in Table 14. As in the case of Eu-doped $LaPO_4$, the major species in Cm-doped $LaPO_4$ shows a long fluorescence lifetime (1.7 ms), which corresponds to an absence of water in the first coordination sphere of Cm. Based on a comparison with the case of Eu-doped $LaPO_4$, the major Cm species is supposed to be on a La site of $LaPO_4$. The minor Cm species has a 0.52 ms lifetime, and shows the presence of 0.4 waters in the first coordination sphere of Cm. This value is similar to the one of minor Eu species.

Table 14: Relative abundance, fluorescence lifetime, and number of waters in the first coordination sphere, for both Cm species, before and after thermal treatment.

Cm-doped $LaPO_4$	Species	Relative Abundance (%)	Lifetime (ms)	n (H_2O)
Before thermal treatment	Major Cm site	70	1.7	0.0
	Minor Cm site	30	0.52	0.4
After thermal treatment	Major Cm site	100	1.2	0.0

After the thermal treatment, the minor Cm species has disappeared, showing a single species in the sample. This difference with the Eu-doped $LaPO_4$ is probably due to the concentration difference between Eu and Cm in $LaPO_4$ (5 mol% and 7 ppm respectively). The major Cm species stays at 602.5 nm. Figure 43 shows the comparison of three spectra: the excitation spectrum, the UV emission spectrum and the direct excitation emission spectrum, of Cm-doped $LaPO_4$ after thermal treatment. The spectra show several peaks, due to consistent energy splitting of the ground state ($^8S_{7/2}$) after thermal treatment. It can be noticed that the direct excitation emission spectrum corresponds both to the profile of the excitation spectrum and to the UV emission spectrum. It shows that the peaks belong to a single Cm site.

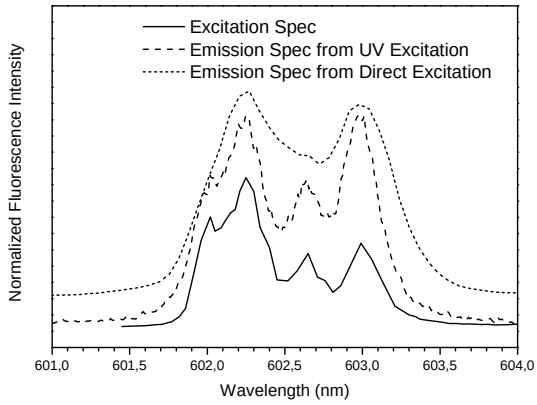

Figure 43: A comparison of the excitation spectrum, emission spectrum from UV excitation, and low resolution emission spectrum from direct excitation at 602.5 nm of Cm-doped $LaPO_4$ after thermal treatment.

The fluorescence decay lifetimes of Cm are measured, with UV excitation and direct excitation at four wavelengths, between 602.0 and 603.0 nm. All the decays are mono-exponential, which proves clearly the presence of a single Cm site. At each wavelength, the lifetime is 1.2 ms. This corresponds to an absence of water in the first coordination sphere of Cm.

The ground state splitting of a Cm (III) ion within La-monazite can be resolved with a high resolution emission spectrum taken under direct excitation. Figure 44 shows four

different species excited by systematically stepping through excitation wavelengths (601.5 to 603.5 nm). Each species shows a four-fold splitting. Cm within the Cm-doped $LaPO_4$ structure has a single Cm site, but shows four species. The slight difference between the four species can only be seen by a precise method such as Cm TRLFS.

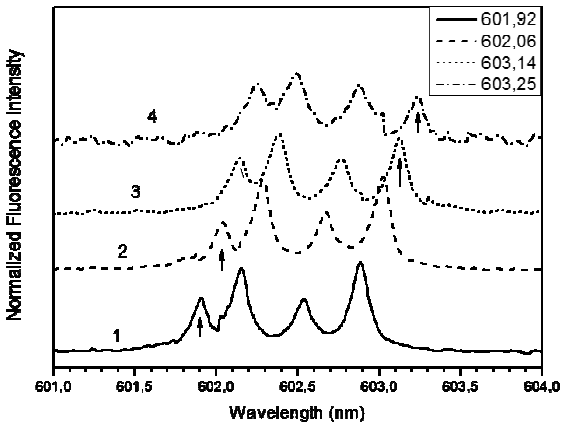

Figure 44: High resolution emission spectra from direct excitation of Cm-doped $LaPO_4$ after thermal treatment. The arrows show the wavelengths mentioned in the legend.

As this is the first time that such a sample is measured by TRLFS, no explanation for this phenomenon can be found in the literature. Nevertheless, a similar behavior of Cm within xenotime crystal structure was observed by Murdoch [117]. The four species found in their work are called “satellites”. Murdoch explained this phenomenon by the presence of impurities or defects in the crystal structure of Cm-doped $LuPO_4$ [117]. The individual spectra could not be resolved in this case, because the excitation energies are overlapped.
Here, the Cm environment of each four satellites is almost identical: similar degree of splitting, ratio of peak heights, proximity to each other, and an unique lifetime. The hypothesis proposed is that a difference in the four La sites within a $LaPO_4$ unit cell exists. Indeed, as shown in the background (see Figure 16), the unit cell of $LaPO_4$ is composed of four La atoms. The Cm species has a single site, as La in $LaPO_4$, but the Cm site has four environments. This is supposed to be due to a deviation from the ideal structure of La-monazite.

4.1.4. Extended X-ray absorption fine structure

The incorporation of Eu in La-monazite was studied by TRLFS. Two Eu species were found in the crystal structure of $La_{0.95}Eu_{0.05}PO_4$. The study suggested that Eu species incorporate on the La site [115]. X-ray absorption fine structure (XAFS) measurements are also performed on the same $La_{0.95}Eu_{0.05}PO_4$ sample, as complement of the information gained with TRLFS. The Eu L_3-edge measurements enable to probe the local chemical environment.

4.1.4.1. Fit of the Fourier transformation of L_3-edge k^3-weighted EXAFS spectra

Figure 45 shows the experimental data and the fit of the Fourier transformation (FT) of L_3-edge k^3-weighted EXAFS spectrum of $La_{0.95}Eu_{0.05}PO_4$. The fits results are given in Table 15. The FT of the $k^3 \cdot \chi(k)$ spectrum shows two peaks between 1.4 and 3.0 Å, two further peaks can be seen between 3.0 and 4.1 Å, and one small peak between 4.1. and 4.5 Å.

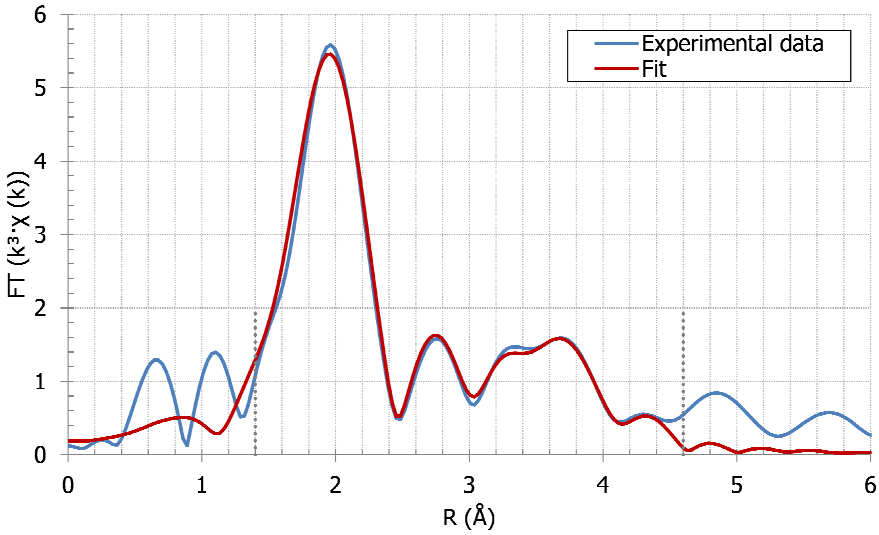

Figure 45: Experimental data and fit of the FT data of Eu (5 mol%)-doped $LaPO_4$. The fit results are presented in Table 15.

Table 15: Parameters of the fit between 1.4 Å and 4.6 Å of the $La_{0.95}Eu_{0.95}PO_4$ EXAFS data. The R-factor [a] is 0.00085.

Shell	N [b]	*r* (Å) [c]	σ^2 (10^{-3} Å^2) [d]	ΔE_0 (eV) [e]
O1	4*	2.37	7	3.3
O2	4*	2.53	7	
O3	1.5*	2.83*	7.5	
P1	1.0*	3.17*	6.8	
O4	1.1*	3.65	6.5	
P2	2.5 ± 0.4	3.76*	6.9	
La	2.1 ±0.5	4.06*	9	
O5	2.7 ± 1.0	4.61	8	

*Held fix during the fitting procedure. [a] The R-factor represents the goodness of the fit. [b] N represents the coordination number. [c] The value *r* represents the distance between Eu and the backscatterer atoms. [d] The σ^2 factor is the full width at half maximum of the peak, and corresponds to the mean square displacement but is often called Debye-Waller factor. It gives information on the structural and thermal order/disorder. If the sample has a high crystallinity around the probed atom, the Debye-Waller factor is low. [e] ΔE_0 is the difference in ionisation energy E_0 of Eu between the energy used to run the calculation (theory) and the energy obtained from the fit. This difference should not exceed ± 10 eV.

4.1.4.2. Interpretation of the results

The two peaks between 1.4 and 3.0 Å are modeled as three oxygen shells (N_{O1} = 4 at *r*(Eu-O1) = 2.37 Å, N_{O2} = 4 at *r*(Eu-O2) = 2.53 Å, and N_{O3} = 1.5 at *r*(Eu-O3) = 2.83 Å). Thus, the fit results of $La_{0.95}Eu_{0.05}PO_4$ suggest the presence of 9.5 oxygen atoms surrounding Eu(III).

Table 16 shows the distances between La and O, within an ideal $LaPO_4$ crystal structure. As already mentioned (section 2.6.1), La is 9-fold coordinate (monoclinic crystal structure) in $LaPO_4$ and the nine oxygen atoms in the first coordinate sphere of La are located at nine different distances (between 2.40 and 2.81 Å). The distances between Eu and the oxygen atoms found here are in good agreement with the La-O distances described in the literature.

Table 16: La-O distances in an ideal $LaPO_4$ crystal structure [72].

	La-O_n distance (Å)								
O_n	O_1	O_2	O_3	O_4	O_5	O_6	O_7	O_8	O_9
Å	2.40	2.48	2.49	2.55	2.58	2.60	2.62	2.68	2.81

The 9.5 oxygen atoms in the first coordination sphere are within the measurement uncertainties similar to 9.0. Europium is 9-fold coordinated by oxygen atoms, thus showing that Eu is incorporated in the La-monazite matrix at a La site. This result is consistent with the conclusion gained from the TRLFS measurements, i.e. that the Eu species incorporate on the La site.

At higher distances (from 3 Å up to 4.5 Å), two phosphor shells are detected at a distance of 3.17 (N_{P1} = 1.0) and 3.76 Å (N_{P2} = 2.5 ± 0.4), with an oxygen shell in-between at 3.65 Å (N_{O4} = 1.1). A lanthanum shell (N_{La} = 2.1 ± 0.5) is located at 4.06 Å and another oxygen shell (N_{O5} = 2.7 ± 1.0) is observed at 4.61 Å. These values are comparable with the values found in the literature for an ideal $LaPO_4$ crystal structure (see Table 17). Indeed, up to four phosphor atoms surround La between 3.17 and 3.77 Å, and, two lanthanum atoms are observed around 4.1 Å in the ideal $LaPO_4$ crystal structure. It confirms the incorporation of Eu at a La position.

Table 17: La-X_n distances in an ideal $LaPO_4$ crystal structure [72].

	La-X_n distance (Å)					
X_n	P_1	P_2	P_3	P_4	La_1	La_2
Å	3.19	3.29	3.59	3.77	4.11	4.11

The EXAFS data are in good agreement with the information found in the literature and with the TRLFS measurements. Eu (III) TRLFS and EXAFS measurements of Eu-doped La-monazite show that Eu is incorporated in the La-monazite crystal structure.

4.2. Characterization of monazite-type pellets

4.2.1. Sintering process

The synthesis process of ceramic materials is divided into three steps: the synthesis of the powder, the forming of the powder, and the sintering. The first two steps can be of several types: e.g. the wet or solid-state route for the synthesis, and the slip casting or the pressing for the forming. The sintering process of ceramics is mainly influenced by temperature and dwell time. In this chapter dedicated to pellet characterization, the sintering process is the key in understanding the microstructure evolution, the density measurements, and the dilatometric behavior.

The sintering is the organization and the consolidation of powder particles to form a polycrystalline material. This process is composed of simultaneous phenomena: the consolidation, the densification and the granular growth (grains and particles). The consolidation happens with the development of necks between particles, by means of transport of matter by diffusion. The densification happens with the decrease of the porosity, resulting in the global shrinkage of the ceramic [77]. Through the sintering, powder becomes a mechanically cohesive material with a given microstructure.

Most of the sintering mechanisms are thermally activated. The atomic diffusion leading to the consolidation happens at temperatures 60 – 80 % of the melting temperature T_m (K) [77]. As the melting point of La-monazite is of 2072 °C ± 20 °C [76], its sintering temperature ideally is between 1134 °C and 1603 °C. Here, the sintering temperature was chosen to be 1400 °C, following the work of Bregiroux [118].

4.2.2. Microstructure study of La-monazite pellet by means of SEM

In this work, La-monazite green pellets were sintered during three hours at 1400 °C. The microstructure is presented on Figure 46 and shows polygonal grain boundaries that are typical for sintered grains. The grain size is from 0.5 µm to 5 µm, and the average grain size was estimated by the linear intercept method to be 1.7 ± 0.2 µm [119]. The convex grains marked with red arrows are typical grains that would gradually disappear under further heat treatment, because of diffusion mechanism and grain growth.

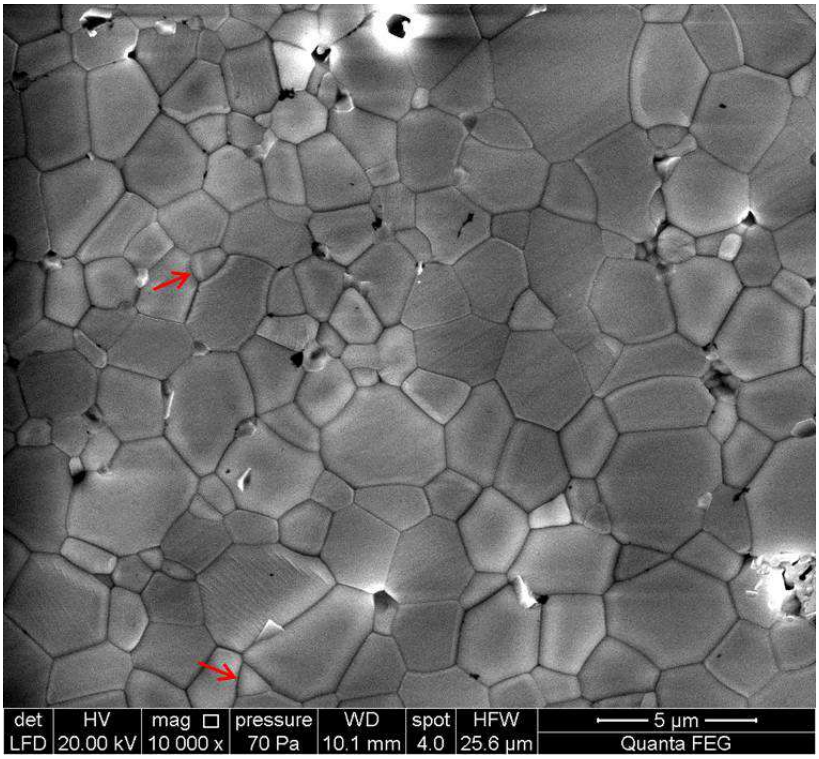

Figure 46: SEM-photography at a magnification of 10 000, of La-monazite pellets sintered at 1400 °C.

4.2.3. Optimization of the density of the pellets depending on the calcination temperature

In order to obtain a mechanically stable matrix, La-monazite pellet properties have to be improved. For example, the mechanical strength of ceramic matrices can be improved with the increase of the sintering density [120]. In this work, the compaction efficiency or compressibility, and the sinterability are studied. Figure 47 shows a typical compressibility behavior of ceramic materials [121]. The green density ρ_g is plotted versus the logarithm of pressure *P* and is characterized by three linear regions and two break points at pressures P_1 and P_2. The intersection point of regions 1 and 2 forms the first break point at pressure P_1 and the intersection point of regions 2 and 3 forms the second break point at pressure P_2.

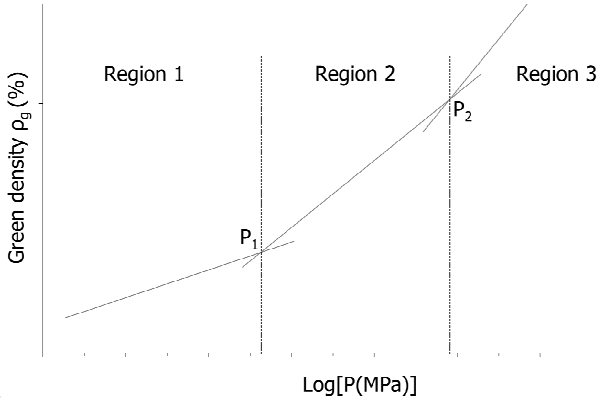

Figure 47: Typical compressibility curve of ceramic material.

The microstructure development of the powder after being pressed explains the presence of these three regions. Figure 48 shows a schematic representation of the microstructure of ceramic powder synthesized by wet chemical method [121; 122]. The microstructure of powder directly after synthesis is different from the one after drying. As synthesized powder is composed of small and strong aggregates of primary particles, whereas dried powder is composed of weak and highly porous agglomerates of aggregates.

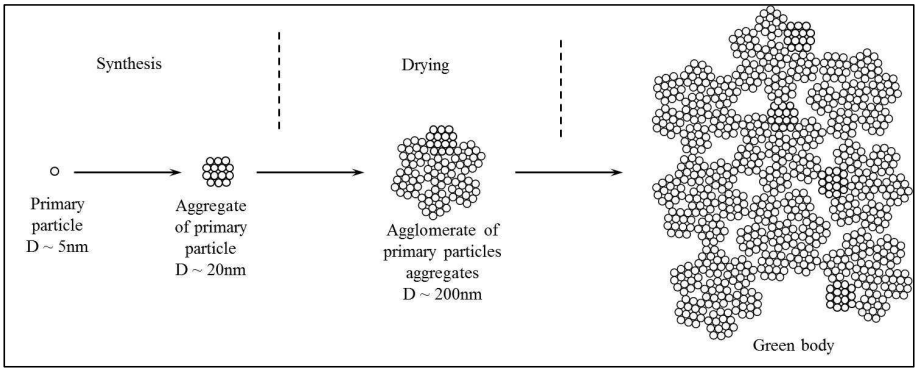

Figure 48: Schematic representation of the microstructural elements (primary particles. aggregates and agglomerates) of ceramic powder (as synthesized sample and after drying) synthesized by wet chemical method. Average size *D* is given for each elements [123].

When powder is pressed into compact pellets, the microstructure of dried powder is damaged. At low pressure ($P < P_1$), the pellet is compacted by partial fragmentation and

reorganization of the agglomerates. At higher pressure ($P_1 < P < P_2$), agglomerates fragment and rearrange themselves. At high pressure ($P_2 < P$), as the agglomerates already cracked, the aggregates fragment and reorganize. Pressure P_1 corresponds to the average compression strength of the agglomerates, whereas the pressure at the second break point (P_2) corresponds to the average compression strength of the aggregates.

The compressibility and the sinterability were investigated on the same samples, in order to determine the maximal sintering density achievable. Here, the results are compared for pellets made of powder calcined at 350 °C (T_2), 500 °C (T_3) and 950 °C (T_4). Figure 49 to Figure 51 show the green densities (ρ_g) and the sintering density (ρ_s) versus the applied pressure (P) of La-monazite pellets. The relative green density that corresponds to each of the three temperatures shows a similar behavior as on Figure 47.

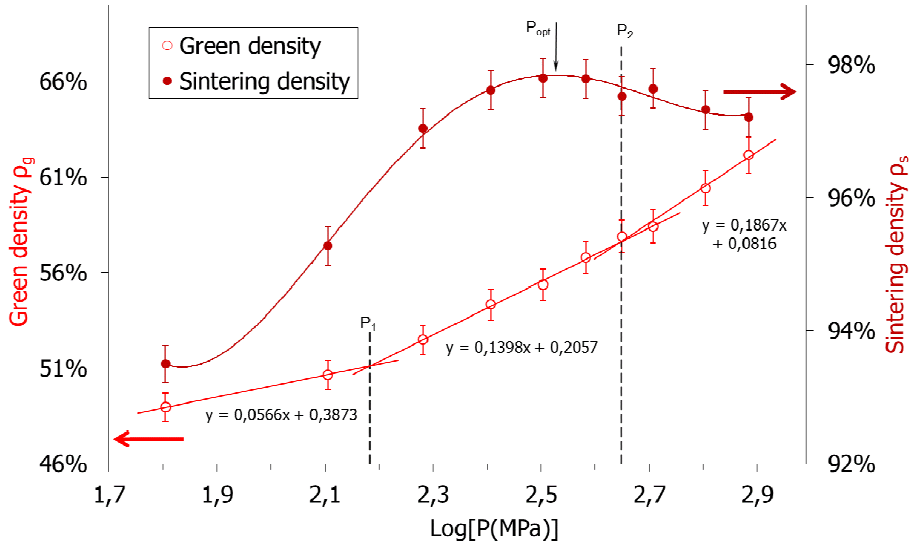

Figure 49: Green density (ρ_g) and sintering density (ρ_s) of pellets pressed with La-monazite powder after calcination at T_2 = 350 °C.

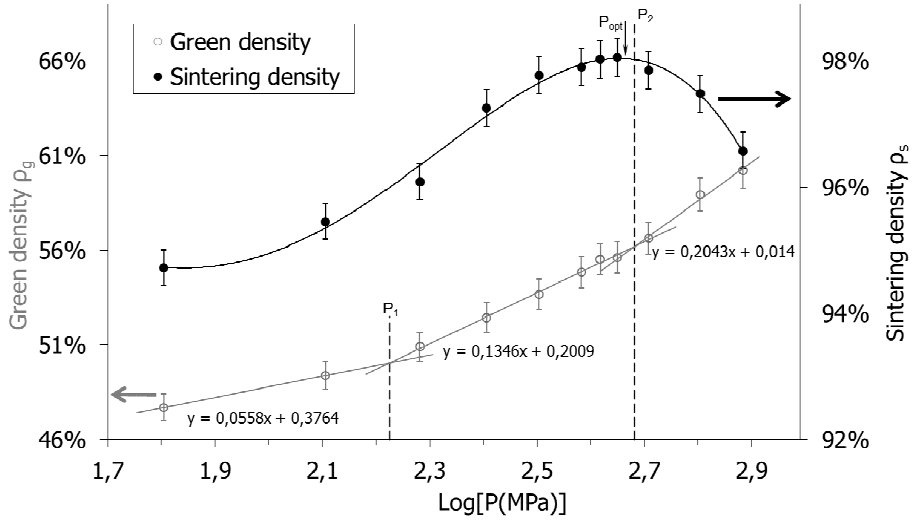

Figure 50 : Green density (ρ_g) and sintering density (ρ_s) of pellets pressed with La-monazite powder after calcination at T_3 = 500 °C.

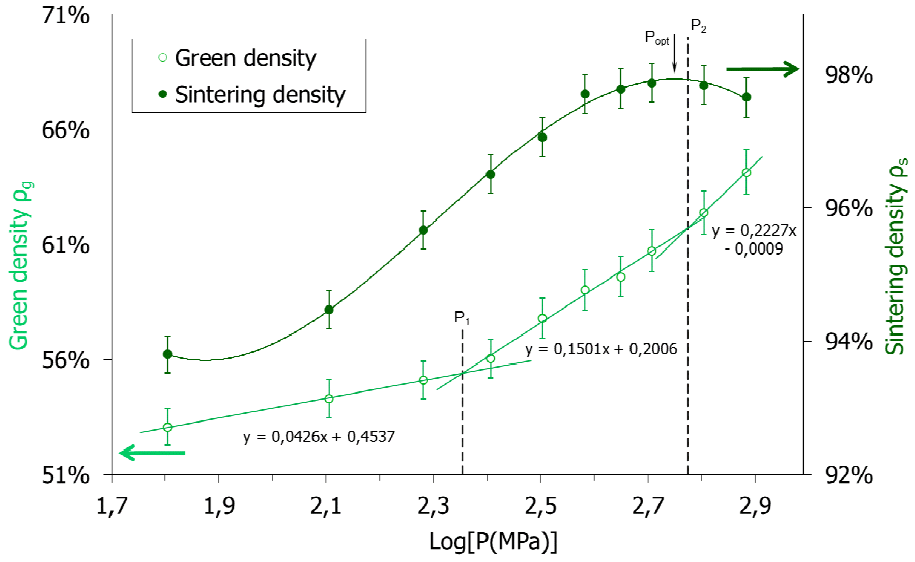

Figure 51 : Green density (ρ_g) and sintering density (ρ_s) of pellets pressed with La-monazite powder after calcination at T_4 = 950 °C.

After three hours of sintering at 1400 °C, the relative sintering density of the pellets was determined by hydrostatic weighing in water (see sub-section 3.1.4.1). The values of ρ_s at each calcination temperature show a well defined maximum, which corresponds to the optimal compaction pressure (P_{opt}). For uniaxial pressing, a maximal pressure is always observed, above which delamination of the pellet takes place. This delamination phenomenon induces the separation of the pellet into horizontal layers after unloading [124].

Figure 52, the values of P_{opt} as well as the corresponding relative sintering density ρ_s are plotted together with P_1 and P_2, in relation with the calcination temperature. The values of P_1 and P_2 respectively follow a simple linear regression. At T_3 and T_4, the value of P_{opt} is slightly lower than P_2. The maximal relative sintering density is of 98.0 % and is achieved for pellets made of powder calcined at 500 °C and pressed at 472 MPa. Pellets used for dissolution tests and radiation tolerance tests are synthesized at these optimal parameters.

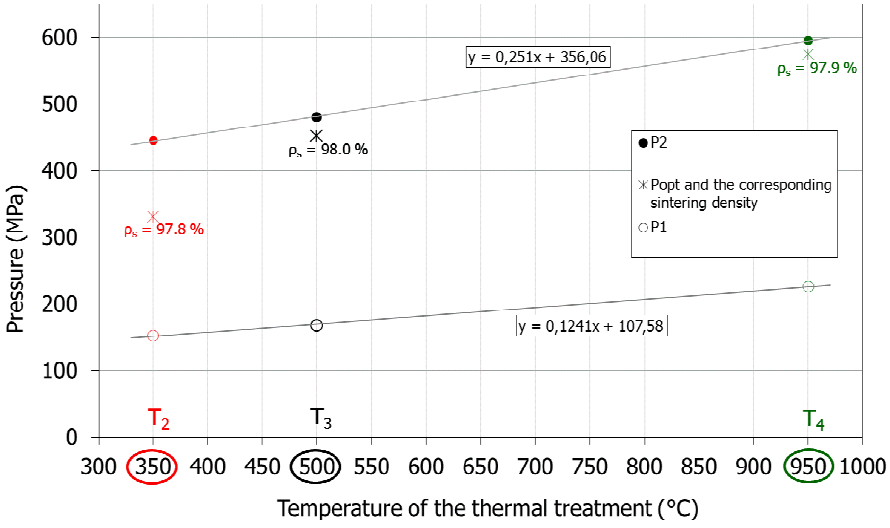

Figure 52 : Summation of the pressures P_2, P_{opt}, P_1 obtained for T = 350 °C, 500 °C and 950 °C.

4.2.4. Vickers microhardness and fracture toughness of La-monazite

The mechanical properties of La-monazite pellets were investigated in terms of Vickers microhardness (H_v) and fracture toughness (K_{IC}). Both values are measured on the same samples. The indents formed during the microhardness measurement are the source of the cracks used to determine the fracture toughness, which is the property of a cracked sample to avoid fracture. Figure 53 is a picture of a typical Vickers indenter on a La-monazite pellet. The red arrow shows a crack induced by the diamond Vickers indenter.

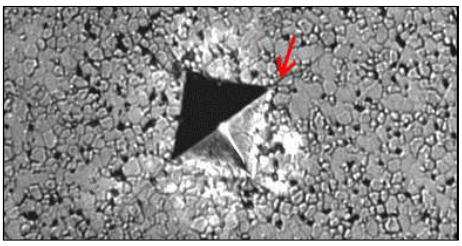

Figure 53: Indent and cracks on a La-monazite pellet due to the Vickers microhardness measurements.

Table 18 summarizes reference data and average values obtained for La-monazite pellets synthesized in this work. The two values of H_v are in good agreement (5.7 ± 0.1 GPa and 5.6 ± 0.4 GPa). The average fracture toughness calculated here is compared to a reference data obtained by a different method. The value gained by the Anstis equation (1.25 ± 0.14 MPa·$m^{0.5}$) is slightly higher than the reference data (1.0 ± 0.1 MPa·$m^{0.5}$). However, the value are similar within the marge of error.

The fracture toughness of La-monazite is comparable to porcelain, which is about 1.0 to 1.3 MPa·$m^{0.5}$ [125]. Compared to other ceramic materials like alumina (2.5 to 3.5 MPa·$m^{0.5}$) and silicon carbide (2.6 to 2.8 MPa·$m^{0.5}$), the fracture toughness of La-monazite is low. Nevertheless, the value of borosilicate glass is about 0.75 to 0.82 MPa·$m^{0.5}$. Therefore, La-monazite crystal has a higher ability to resist fracturing than borosilicate glass [125].

Table 18: Comparison of average values of Vickers microhardness and fracture toughness, between La-monazite pellets synthesized in this work and reference data of La-monazite.

	H_v (GPa)	K_{IC} (MPa·m$^{0.5}$)	
		Anstis equation	***Chantikul equation***
This work	5.7 ± 0.1	1.25 ± 0.14	-
[92]	5.6 ± 0.4	-	1.0 ± 0.1

4.2.5. Dilatometric measurements on La-monazite calcined at different temperatures

As already mentioned (see section 4.2.1), the sintering process almost always induces densification of the material. Theoretically, this densification takes place in three stages [124]: the initial stage for $0.50 < \rho < 0.65$, the intermediate stage for $0.65 < \rho < 0.92$ and the final stage for $0.92 < \rho$. The beginning of the densification ($0.50 < \rho < 0.65$) is related to the reorganization of the particles, as well as their consolidation with formation of necks between grains. Then ($0.65 < \rho < 0.92$), the open porosity is eliminated and the grain growth starts slowly. Finally ($0.92 < \rho$), the densification corresponds to the elimination of the closed porosity. An important grain growth is often observed.

The sintering behavior of La-monazite calcined at T_2 (350 °C), T_3 (500 °C) and T_4 (950 °C) was investigated by dilatometry up to 1400 °C. Dilatometric measurements on similar samples are reported in the literature: $GdPO_4$ and $La_{0.5}Gd_{0.5}PO_4$ [42], as well as La-rhabdophane and La-monazite [110]. In this work, the relative density of pellets and the densification rate were calculated with the linear relative shrinkage using equation (9) [97]. Figure 54 shows the evolution of the relative density with the temperature of pellets made of powder calcined at T_2 (350 °C), T_3 (500 °C) and T_4 (950 °C). Figure 55 shows the derivative of the relative density as a function of the temperature. Characteristic densities and temperatures are plotted on the figures as dotted line. Both figures are complementary and are analyzed in parallel. Table 19 summarizes the characteristic T* and T** temperatures, as well as the corresponding relative densities.

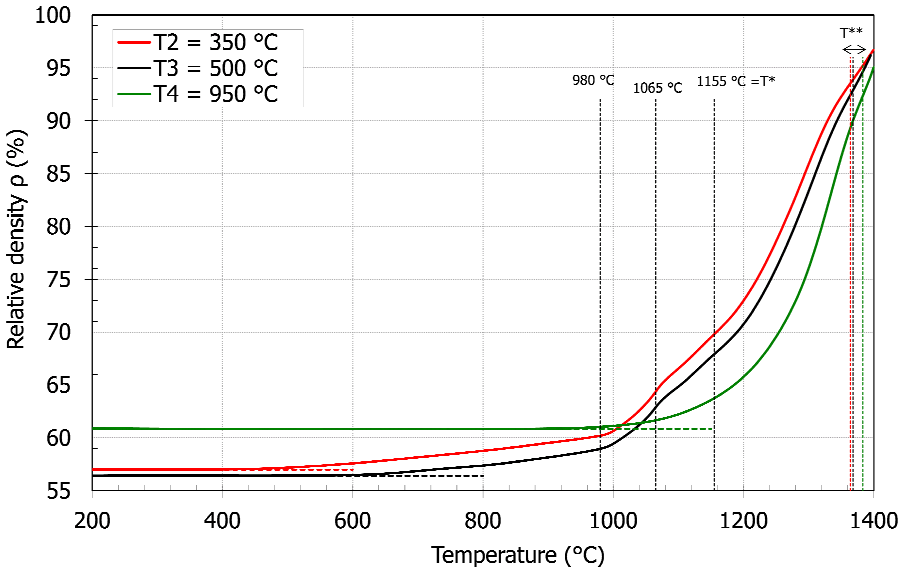

Figure 54 : Relative density versus the temperature of pellets made of powder calcined at 350 °C (red), 500 °C (black), and 950 °C (green), respectively.

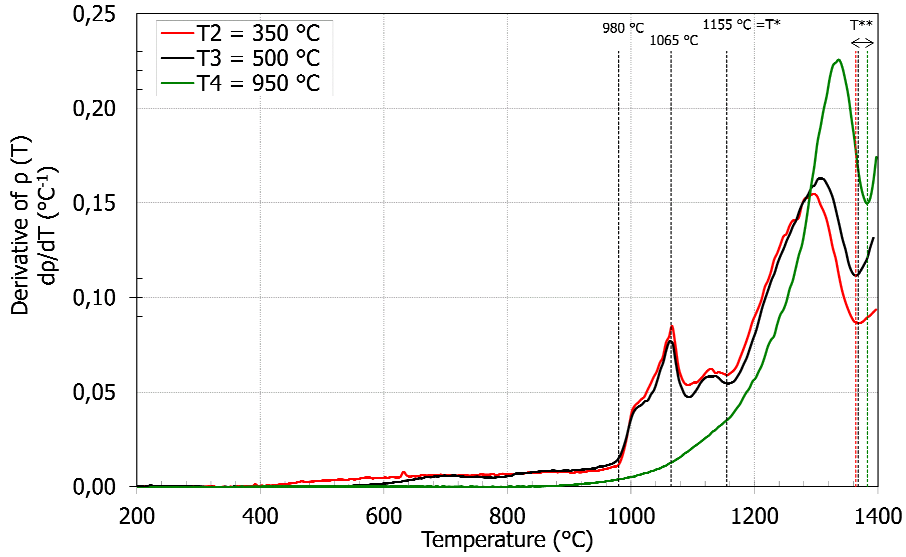

Figure 55 : Derivative of relative density versus the temperature of pellets made of powder calcined at 350 °C (red), 500 °C (black), and 950 °C (green), respectively.

The T_2 (red) and T_3 (black) curves show a similar initial behavior, while the T_4 curve (green) reveals a higher initial density. The density at 200 °C is 57 % (T_2), 56.5 % (T_3), and 61 % (T_4). This observation is likely to be related to differences in grain size (see Table 10). The grain size is comparable for T_2 and T_3 (about 20 nm), whereas the grain size of T_4 is more than ten times higher (about 250 nm). At 950 °C, the crystallization process has already started, and the powder shows consolidation and a growing uniformity. This morphology leads to a higher initial density of the sample. The increase of the density starts at 400 °C (T_2), 560 °C (T_3) and 900 °C (T_4), and it corresponds to the beginning of the sintering [77].

The first particular temperature (T = 980 °C), was determined with the second derivative of ρ (T) and corresponds to the beginning of the initial stage. It is also the beginning of an increase of the relative density. The slight densification recorded from room temperature up to 980 °C can be related to the mass loss observed by the thermogravimetric measurements (see section 4.1.1). This mass loss in the structure induces a contraction of the lattice [110]. The initial stage occurs from 980 to 1155 °C, as the density increases from 60 to ~67 %. At about 1065 °C, the derivative of the density of T_2 and T_3 shows a maximum. It corresponds to a density of ~ 65 % for both samples.

The intermediate stage takes place from 1155 °C (T*) to approx. 1370 °C (T**), as the density increases from 67 to 93 % (see Table 19). The T* temperature (1155 °C) corresponds to the end of a complex behavior (Figure 55) and was determined precisely from the secondary derivative of ρ (T). This complex behavior is related to the end of the elimination of residual OH-groups. The stable sintering starts at 1155 °C. At temperatures of 1292 °C, 1298 °C, and 1327 °C for T_2, T_3, and T_4 respectively, the densification rate is decreasing abruptly. This phenomenon is also observed in the work reported in [42], and the corresponding density is approx. 83 %.

The final stage takes place from T** to 1400 °C, as density increases from 93 % to the final density value. The derivative curve shows an increase. The final sintering density is approx. 96.69 %, 96.17 %, and 95.04 % for T_2, T_3, and T_4, respectively. These values are lower than the ones obtained from the density measurement after sintering at 1400 °C (97.8 %, 98.0 %, and 97.9 %, see Figure 52). This difference is due to the sintering dwell

time of 3 hours at 1400 °C, while the thermal treatment in dilatometric measurements has no dwell time at 1400 °C.

Table 19: Characteristic temperatures (T*, T) and the associated densities of pellets made of powder calcined at 350 °C, 500 °C, and 950 °C.**

	T_2 = 350 °C	**T_3 = 500 °C**	**T_4 = 950 °C**
T* (ρ (%))	1155 °C (69.8 %)	1155 °C (67.9 %)	1155 °C (63.7 %)
T** (ρ (%))	1368 °C (93.9 %)	1364 °C (92.4 %)	1383 °C (92.2 %)

4.3. Resistance to corrosion and to irradiation of monazite-type samples

4.3.1. Aqueous durability tests on monazite-type samples

Information on the long-term behavior of the matrices in final disposals is needed. The behavior of the host matrices during a worst-case scenario, i.e. water reaches and enters into nuclear waste containers, has to be investigated. An intrusion of liquid would be a cause for the radionuclides migration in the biosphere.

The interaction between the liquid and the ceramic in weathering conditions can be simulated with aqueous dissolution tests. The aim of these tests is to obtain quantitative dissolution rates of different elements within their crystal structure and to understand dissolution mechanisms.

4.3.1.1. Normalized weight loss and normalized dissolution rate of La in La-monazite

Analysis of the samples

The La-monazite used for the aqueous durability tests was synthesized with powder using a La:P molar ratio of 1:1. The experiments were realized on crushed pellets fractionated with 100 µm- and 180 µm-sieves (see flow chart on p. 47).

Figure 56 shows the crushed pellets before the durability tests. The size of the grains is not exclusively comprised between 100 µm and 180 µm, as the sieves are bi-dimensional whereas the grains are tri-dimensional. However, the grains show a regular size, above 100 µm and below 400 µm.

The XRD pattern of the sample is shown on Figure 57 together with the $LaPO_4$ reference (database PDF 2, n° 00-032-0493). The sample (black curve) matches with the indexed Bragg reflections of the reference (blue peaks). The sample is composed of $LaPO_4$ phase and is free of La_3PO_7 impurities.

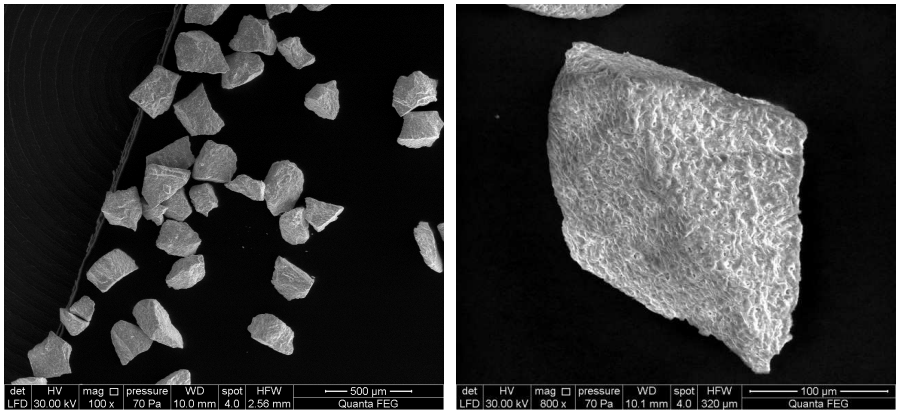

Figure 56: SEM photos of crushed $LaPO_4$ pellets fractionated with 100 µm- and 180 µm-sieves. Pictures are at a magnification of 100 (left) and 800 (right).

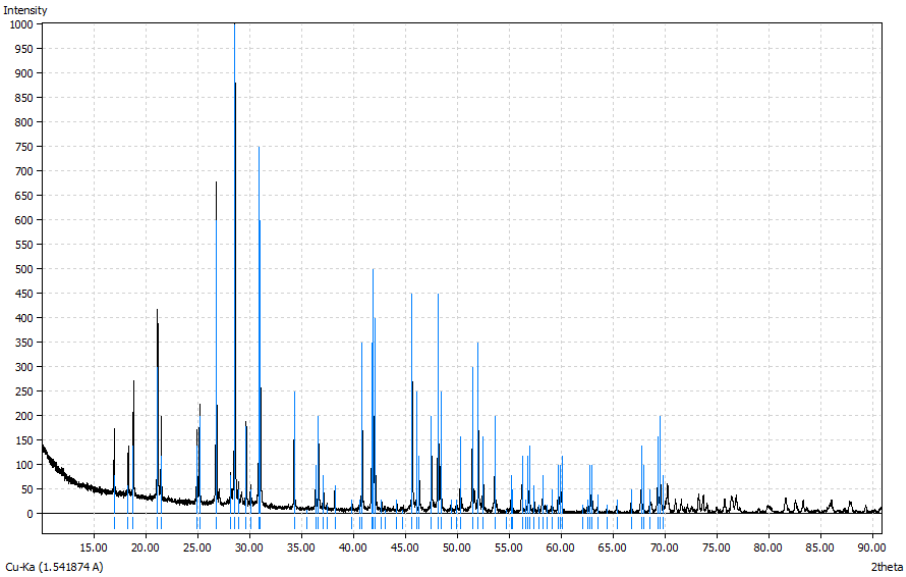

Figure 57: XRD pattern of $LaPO_4$ sample used for leaching tests (black) together with reference data of $LaPO_4$ (blue).

Interpretation of the results

La-monazite has a low solubility (see section 2.6.4). The evolution of the normalized weight loss of low soluble ceramics can be schematically represented as on Figure 58. The cases of an unwashed sample as well as a washed sample are shown here. An unwashed material will exhibit initial perturbations, due to surface heterogeneity (e.g. non-stoichiometry or presence of small particles at the surface) [39; 126]. The curves are then divided in a first part driven by kinetics and a second part essentially driven by thermodynamics. In the first part, the dissolution occurs far from the equilibrium and the normalized dissolution rate R_L is constant. R_L can be determined by the slope of the linear curve (see equation (11)) [39]. In the second part, the evolution of the dissolution decreases because the thermodynamic equilibrium was achieved in the leachate. The solution is saturated with the dissolute product and further dissolution cause the precipitation of a neoformed phase. The release of the elements in the leachate is due to diffusion processes [127]. The determination of the normalized dissolution rate is more complex near the equilibrium, than far from the equilibrium.

Figure 59 shows the normalized weight loss N_L versus time of La within a La-monazite sample. The experiment is described in section 3.1.12. Initial perturbations are observed during the first three days of the experiment. These perturbations are due to the washing of the samples with distilled water instead of acidic media. A washing at low pH could have discarded the irregularities at the surface and avoid this behavior of N_L. From day 3 up to day 28, the values of N_L show a linear behavior. The slope of the linear regression corresponds to the normalized dissolution rate R_L (La). Here, R_L (La) = $6.71 \cdot 10^{-5}$ g·m^{-2}·d^{-1}.

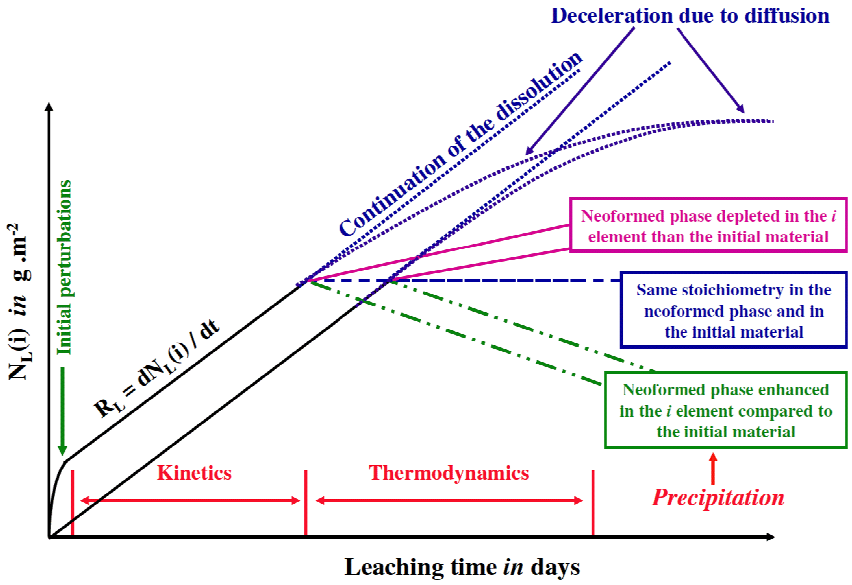

Figure 58: Schematic representation of the normalized weight loss ($N_L(i)$) of a low soluble sample. The cases of a sample either with or without initial perturbations are presented [39; 128].

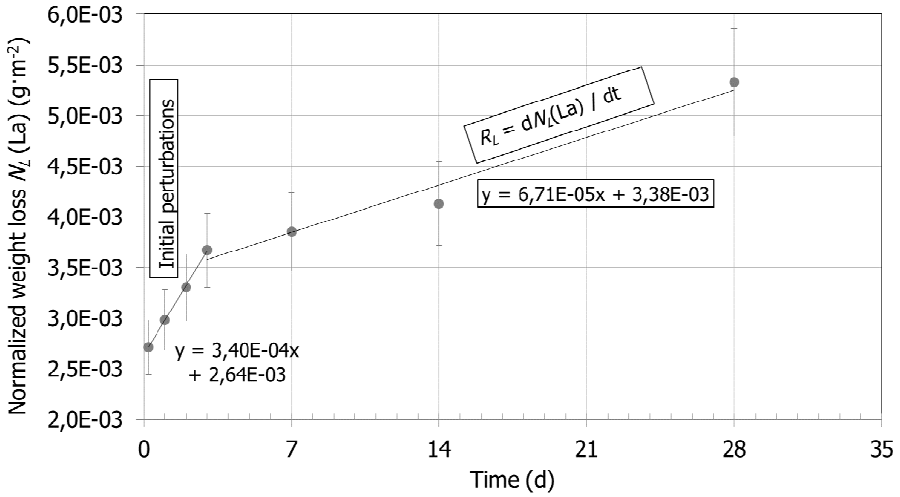

Figure 59: Normalized weight loss N_L (La) of unwashed La-monazite sample versus time.

4.3.1.2. Normalized dissolution rate of La and Eu in Eu-doped La-monazite

Aqueous dissolution tests on Eu-doped $LaPO_4$ were run in the same conditions as for $LaPO_4$. The results are reported in Table 20. Some N_L (Eu) values can not be taken into account, because the leachate is near the thermodynamic equilibrium. The concentration of Eu in the leachate is about $1.19 \cdot 10^{-5}$ mol·L^{-1} (see 3.1.12).

Table 20: Normalized weight loss $N_L(i)$ of La and Eu in $La_{(1-x)}Eu_xPO_4$ (with x = 0.0 to 1.0), after 0.2 to 28 days.

		Normalized weight loss $N_L(i)$ (g·m^{-2})						
x / i \ days		0.2	1	2	3	7	14	28
0.0	La	$2.71 \cdot 10^{-3}$	$2.98 \cdot 10^{-3}$	$3.30 \cdot 10^{-3}$	$3.67 \cdot 10^{-3}$	$3.86 \cdot 10^{-3}$	$4.13 \cdot 10^{-3}$	$5.33 \cdot 10^{-3}$
0.2	La	$1.50 \cdot 10^{-4}$	$3.78 \cdot 10^{-4}$	$5.13 \cdot 10^{-4}$	$5.58 \cdot 10^{-4}$	$1.22 \cdot 10^{-3}$	$1.62 \cdot 10^{-3}$	$1.57 \cdot 10^{-3}$
	Eu	$6.40 \cdot 10^{-4}$	$1.23 \cdot 10^{-3}$	$1.71 \cdot 10^{-3}$	$1.95 \cdot 10^{-3}$	$3.70 \cdot 10^{-3}$	$6.32 \cdot 10^{-3}$	$6.17 \cdot 10^{-3}$
0.5	La	$6.25 \cdot 10^{-4}$	$1.21 \cdot 10^{-3}$	$1.83 \cdot 10^{-3}$	$2.11 \cdot 10^{-3}$	-[a]	$2.84 \cdot 10^{-3}$	$3.30 \cdot 10^{-3}$
	Eu	$2.11 \cdot 10^{-3}$	$3.35 \cdot 10^{-3}$	$4.75 \cdot 10^{-3}$	$5.63 \cdot 10^{-3}$	-	-	-
0.8	La	$2.00 \cdot 10^{-3}$	$3.42 \cdot 10^{-3}$	$3.37 \cdot 10^{-3}$	$4.68 \cdot 10^{-3}$	$5.95 \cdot 10^{-3}$	$5.63 \cdot 10^{-3}$	$7.79 \cdot 10^{-3}$
	Eu	$5.14 \cdot 10^{-3}$	-	-	-	-	-	-
1.0	Eu	$5.30 \cdot 10^{-3}$	-	-	-	-	-	-

[a] not measured.

Figure 60 summarizes the values of normalized dissolution rates R_L of La and Eu obtained with Eu-doped $LaPO_4$ samples. The rates are calculated with the values of N_L from day 3 to day 28. R_L (La) varies between $3.40 \cdot 10^{-5}$ and $1.10 \cdot 10^{-4}$ g·m^{-2}·d^{-1}. It can be seen that the normalized dissolution rate is dependent of the composition of the (La, Eu)PO_4 solid solution. Within our experiments, a minimum dissolution rate was obtained for the $La_{0.8}Eu_{0.2}PO_4$ composition. With higher doping of Eu, the dissolution rate increases up to $1.10 \cdot 10^{-4}$ g·m^{-2}·d^{-1} for $La_{0.2}Eu_{0.8}PO_4$. Further aqueous dissolution tests would determine if a R_L minimum could be reached for a Eu content of 27 mol% (black arrow on Figure 60). This value is a typical actinide waste loading within monazite-type ceramics [8].

The rate for Eu within a $La_{0.8}Eu_{0.2}PO_4$ composition is $1.58 \cdot 10^{-4}$ g·m^{-2}·d^{-1}. The dissolution is called congruent if the elements of the matrix being dissolved have the same normalized dissolution rate. Within $La_{0.8}Eu_{0.2}PO_4$, Eu has definitely a higher dissolution rate than La. The ratio of R_L (Eu) over R_L (La) is 4.65 [39; 129]. As this value is superior to 1, the dissolution of Eu-doped $LaPO_4$ can be qualified as incongruent. In the work of Cetiner et al., the dissolution of La-monazite was also found to be incongruent [130].

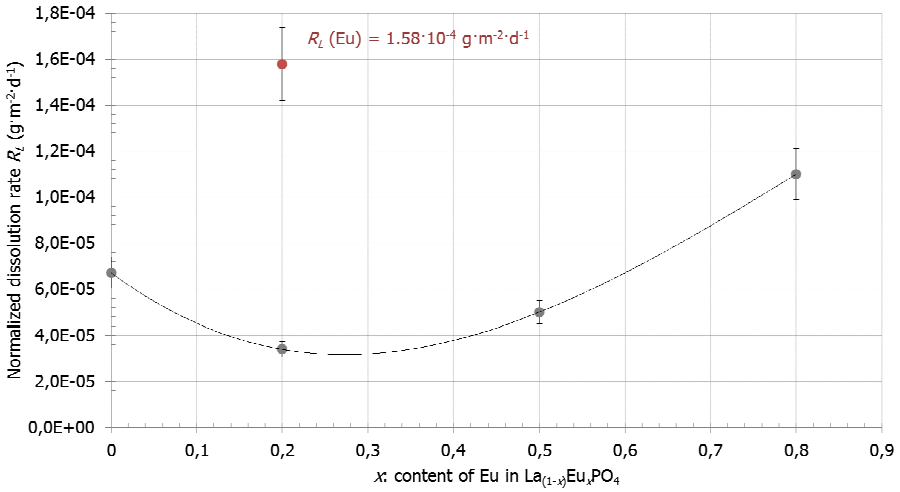

Figure 60: Normalized dissolution rate R_L (La (grey) and Eu (red)) of Eu-doped $LaPO_4$. R_L is calculated with N_L values between day 3 and day 28.

4.3.1.3. Comparison with the literature

The dissolution rates of Ce (43 mol%) within natural monazite obtained in acidic media (pH = 2) at different temperatures were shown above (Table 7, p. 37) [41]. The dissolution rate of Ce at 70 °C is $1.33 \cdot 10^{-5}$ g·m^{-2}·d^{-1}. Regarding the temperature of the media, the difference between this work and the work of Oelkers et al. is 20 °C. However, the dissolution rate is of the same order of magnitude than R_L(La) in a 50 mol% content of La in Eu-doped $LaPO_4$ (R_L(La) = $5.00 \cdot 10^{-5}$ g·m^{-2}·d^{-1}). The data measured here are in good agreement with the data found for natural analogues.

In the work of Terra et al. [42], normalized dissolution rate of $GdPO_4$ in acidic media is measured. At very low pH (pH = 1), R_L (Gd) is of $(3.8 \pm 0.8)\cdot 10^{-4}$ g·m^{-2}·d^{-1}. At higher pH (pH = 4), R_L (Gd) is of $(4.8 \pm 1.4)\cdot 10^{-6}$ g·m^{-2}·d^{-1}. If it is assumed that R_L (Gd) is proportional to pH between pH = 1 and pH = 4, R_L (Gd) at pH = 2 would be about $2.6\cdot 10^{-4}$ g·m^{-2}·d^{-1}. This value is of the same order of magnitude as R_L (Eu) ($1.58\cdot 10^{-4}$ g·m^{-2}·d^{-1} at pH = 2).

To conclude, R_L (La (Z = 57)) is of the same order of magnitude of the dissolution rate of Ce (Z = 58), and R_L (Eu (Z = 63)) is of the same order of magnitude of R_L (Gd (Z = 64)). Due to the lanthanide contraction, the size of La^{+3} is close to the size of Ce^{3+}, and the size of Eu^{+3} is close to the size of Gd^{3+}. The size of the ion could have an impact on its dissolution rate within the monazite host matrices. This assumption needs to be verified on the basis of further experiments.

Pierce et al. worked on the dissolution of LaBS glass [29]. The normalized release rate of B is $1.22 \pm 0.14\cdot 10^{-3}$ g·m^{-2}·d^{-1}, which is one order of magnitude higher than Eu and even two orders of magnitude higher than La in Eu-doped La-monazite. Table 21 shows the normalized dissolution rate of Na, Cs and Sr in phosphate and borosilicate glasses, measured in deionized water at room temperature [131].

The average value of R_L in borosilicate glass is $0.5\cdot 10^{-2}$ g·m^{-2}·d^{-1}, and it is of $0.8\cdot 10^{-2}$ g·m^{-2}·d^{-1} in phosphate glass. The normalized dissolution rates of Eu and La are two and three orders of magnitude respectively lower than the values found by Lee for glasses [131].

Table 21: Normalized dissolution rate (R_L) of borosilicate and phosphate glasses [131].

	Normalized dissolution rate R_L (i) (g·m^{-2}·d^{-1})		
i / **Glass type**	**Na**	**Cs**	**Sr**
Borosilicate	$0.9\cdot 10^{-2}$	$0.3\cdot 10^{-2}$	$0.2\cdot 10^{-2}$
Phosphate	$0.8\cdot 10^{-2}$	$1.1\cdot 10^{-2}$	$0.4\cdot 10^{-2}$

The normalized dissolution rates of the lanthanides within La-monazite found here are lower than the ones of B, Na, Cs and Sr in glasses. Therefore, the synthetic monazite as a host phase can be considered superior to amorphous material such as borosilicate and phosphate glasses due to its low aqueous dissolution rate.

4.3.2. Radiation tolerance tests on La-monazite pellets by means of ion implantation

Host matrices for MA have to resist to self-irradiation. The structural damages created by the self-irradiation are mainly due to the alpha recoil. In order to recreate the damages at a laboratory scale, the inner irradiation is simulated by means of external bombardment of the matrix with ions. Here, the recoil of the alpha particle is simulated with implantation of Kr^{2+} ions.

4.3.2.1. Raman spectroscopy of La-monazite pellets before ion implantation

The Raman measurement is represented with intensity (counts) versus Raman shift (cm^{-1}). Figure 61 shows the fitted spectrum obtained for a $LaPO_4$ pellet. Thirty different Raman frequencies are observed on the plot. The positions of the single peaks are given in Table 22, together with values found in the literature for $LaPO_4$ samples. The data measured in this work matches with the literature. Furthermore, peaks at frequencies 143 cm^{-1}, 194 cm^{-1}, 560 cm^{-1}, 931 cm^{-1}, 947 cm^{-1} and 965 cm^{-1} were observed for the first time, due to the high-quality of the measurement.

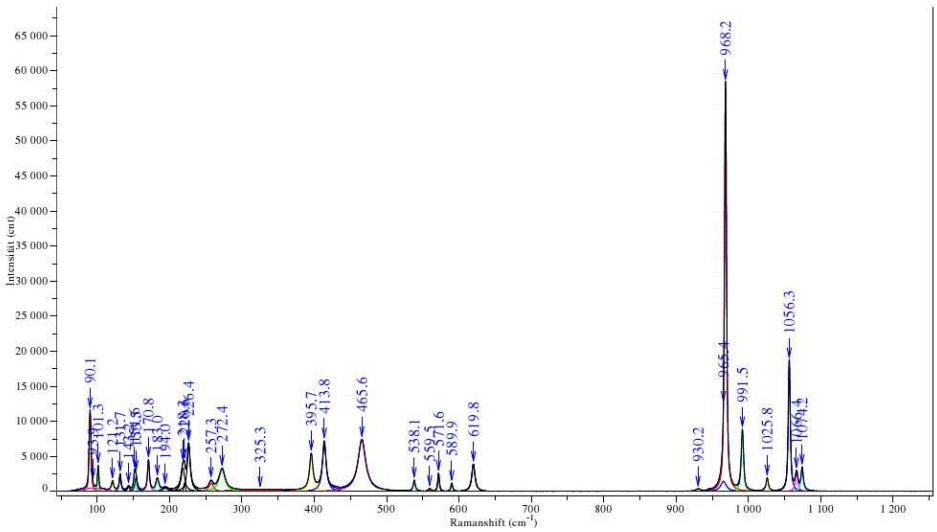

Figure 61: Raman spectrum of a $LaPO_4$ pellet with the corresponding fit and the peak positions (blue).

Table 22: Raman frequencies of a $LaPO_4$ pellet compared with values found in the literature.

This work	[132]	[133]	[134]	Assignment [132]
90	90	90	90 (1.6)	Lattice
101	100	100	100 (0.6)	Lattice
121	-	120	120 (0.2)	Lattice
132	-	131	131 (0.4)	Lattice
143	-	-	-	Lattice
151	151	151	151 (0.5)	Lattice
-	157	-	-	Lattice
171	170	170	170 (0.5)	Lattice
183	184	183	183 (0.3)	Lattice
194	-	-	-	Lattice
220	219	220	220 (1.0)	Lattice
226	226	227	227 (1.1)	Lattice
258	258	255	255 (0.4)	Lattice
272	275	271	271 (1.0)	Lattice
396	396		394 (0.9)	Lattice
414	413	414	414 (1.5)	Lattice
466	466	465	465 (1.7)	ν_2
538	534	537	537 (0.4)	-
560	-	-	-	-
572	567	572	57 2 (0.5)	-
590	587	589	589 (0.3)	-
620	620	619	619 (0.8)	ν_4
931	-	-	-	-
947	-	-	-	-
965	-	-	-	-
968	968	967	967 (10.0)	ν_1
992	987	991	991 (1.7)	-
1026	1021	1025	1025 (0.4)	-
1056	1054	1055	1055 (2.9)	ν_3
1066	-	1065	1065 (0.4)	-
1074	1070	1073	1073 (0.8)	-

According to Silva [132], the Raman shift between 90 cm^{-1} and 414 cm^{-1} is attributed to lattice vibrations. Figure 62 shows the ν_1 to ν_4 modes of vibration of a [PO_4] tetrahedron. The Raman shift ascribed to ν_2 and ν_4 (at 466 cm^{-1} and 620 cm^{-1}) show symmetrical and anti-symmetrical bending vibrations of the [PO_4] tetrahedron respectively [132]. The frequencies ν_1 and ν_3 corresponds to symmetrical and anti-symmetrical stretching vibrations of the [PO_4] tetrahedra [132]. The frequencies, at which bands are not assigned, are essentially due to vibrations of [LnO_9] polyhedra.

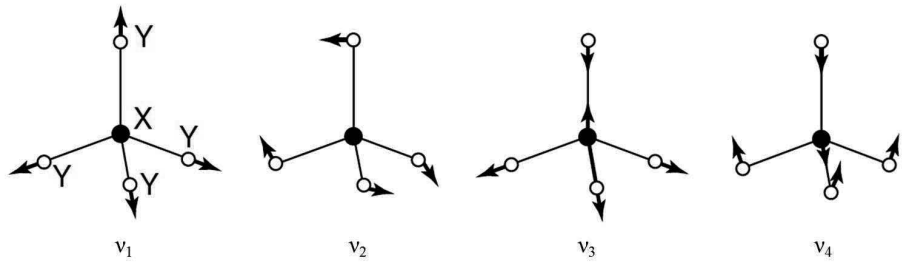

Figure 62: Normal modes of vibration (ν_1 to ν_4) of tetrahedral XY_4 molecules like PO_4 [135].

4.3.2.2. Raman spectroscopy of La-monazite pellets after Kr^{2+} implantation

The radiation damage is induced by external irradiation. The ion bombardment on La-monazite-type pellets was performed with an ion implanter. Three pellets have been bombarded with Kr^{2+} ions (400 keV) at a fluence of 10^{12} to 10^{14} ions·cm^{-2}. The effects of the damage were analyzed by Raman spectroscopy.

Figure 63 shows the intensity versus the Raman shift measured on the pellets after the ion bombardment at different fluences. The measurement shows no difference between the un-irradiated sample and the sample irradiated at a fluence of 10^{12} ions·cm^{-2}. The 10^{13} and 10^{14} ions·cm^{-2} samples show new Raman shifts. In particular between 275 and 375 cm^{-1}, 425 and 450 cm^{-1}, and between 900 and 931 cm^{-1} (black arrows). However, no amorphization, which should involve a clear peak broadening, is observed. This radiation tolerance tests confirmed that $LaPO_4$ is not metamict under these experimental conditions.

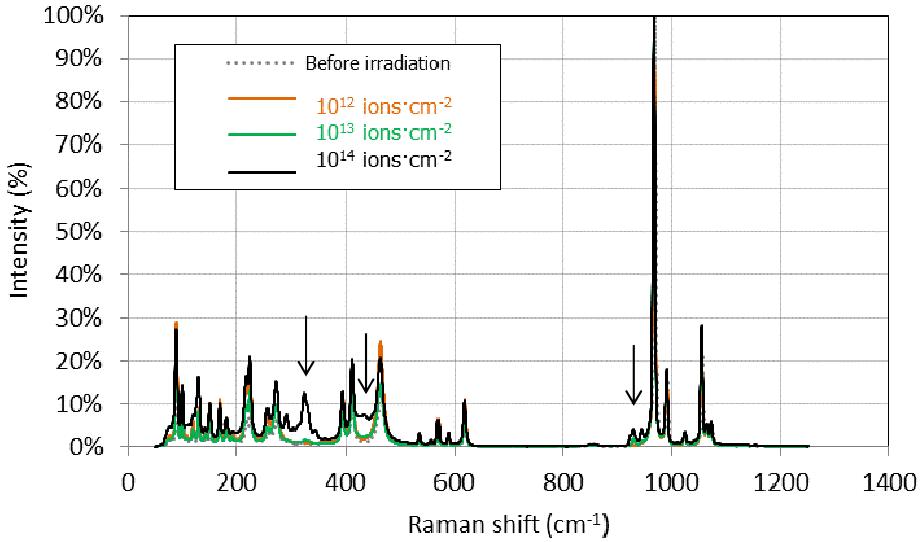

Figure 63: Intensity versus Raman shift of $LaPO_4$ pellets before and after ion bombardment.

5. Conclusion and outlook

The issue of nuclear waste disposal is of general importance as it concerns not only the countries that decided to expand the use of the nuclear power, but also the countries that approach the phase-out of nuclear power generation. The current strategies followed in Europe are the direct disposal of spent nuclear fuel and the disposal of vitrified waste (after reprocessing). However, ceramic waste forms seem to offer several properties related to the long-term safety, such as resistance to radiation damage and aqueous durability, which are superiors to these strategies.

This PhD work contributes to the research in the field of the improvement of the long-term safety of nuclear waste disposals. The aim was to define the ability of the La-monazite-type ceramics as host matrix for minor actinides (MA), which are mainly responsible for the long-term radiotoxicity. The main material properties required for this purpose are the incorporation of the long-lived elements on regular atomic positions within their crystal structure, and the stability of the doped ceramic material in terms of aqueous durability and resistance to irradiation. An integral approach was followed, including an adequate ceramic synthesis procedure, a material characterization, aqueous alteration experiments under repository conditions, and tests of stability against radiation damage.

In the first chapter (sections 4.1.1 and 4.1.2), the thermal behavior (TG-DSC), the morphology (SEM), and the crystal structure (XRD) of La-monazite powder synthesized by hydrothermal route (at 200 °C) were analyzed. Thermogravimetric analyses define characteristic temperatures during a thermal treatment up to 1300 °C: at 350 °C adsorbed water and NH_4NO_3-impurities are eliminated, between 500 °C and 800 °C the La-rhabdophane phase ($LaPO_4 \cdot H_2O$) is transformed into La-monazite, and above 1120 °C the last OH-groups are eliminated leading to the ending of the sample weight loss. The monoclinic structure of the La-monazite phase was confirmed by XRD analyses.
SEM investigations on 95 °C-dried powder showed that the nanoparticles (25 nm) tend to form aggregates of approx. 100 nm. Further measurements via the BET and the Hall-Williamson methods concluded that after a thermal treatment at 1400 °C, particles have a

size of approx. 400 nm and consists of nanocrystallites of approx. 70 nm. At high temperature, the crystallization of the ceramic reduces the lattice distortion to approximately zero.

Furthermore, seven compositions of Eu-doped $LaPO_4$ samples were synthesized and their lattice parameters (*a*, *b*, *c*, *β*) as well as the unit cell volume (*V*) were evaluated for the first time. The decreasing of the lattice parameters *a*, *b*, *c*, and *V* is likely to be related to the progressive replacement of La by Eu in the crystal structure. It suggests the existence of a regular solid solution (La, Eu)PO_4 between the end members $LaPO_4$ and $EuPO_4$. The incorporation of dopants in the lattice structure of La-monazite was then investigated in details by spectroscopic methods (TRLFS and EXAFS) and was presented in the next sections (4.1.3 and 4.1.4). TRLFS was used to explore the local structural environment of Eu (III) and Cm (III) within the monazite crystal structure. Several authors reported about the luminescent properties of synthetic monazite when it is doped with Eu, but there is no data about Cm-doped $LaPO_4$ so far. In Eu-doped $LaPO_4$, a major species is identified at 578.4 nm and a minor species at 577.5 nm. After the thermal treatment of the sample, the major species is still seen at 578.4 nm, whereas the minor species changes from 577.5 to 578.9 nm. Nevertheless, the spectra before and after thermal treatment show the same shape and no significant change. Eu is situated on the La site in both cases, even after synthesis at low temperature (200 °C). The major Eu species shows a long fluorescence lifetime before as well as after thermal treatment at 1000 °C (5.2 ms and 3.6 ms respectively). The Horrocks equation indicates that no water is found in the first coordination sphere. The minor Eu species shows a shorter fluorescence lifetime than the major Eu species with values before and after thermal treatement of 0.95 ms and 1.4 ms respectively. These lifetimes indicate that 0.5 and 0.1 waters are present in the first coordination sphere of Eu. The presence of a hydroxide interstitial is assumed.

Before thermal treatment, the data obtained from fluorescence lifetime measurements on Cm-doped $LaPO_4$ show a long fluorescence lifetime of 1.7 ms for the major species, which corresponds to an absence of water in the first coordination sphere of Cm, as in the case of Eu-doped $LaPO_4$. Through a comparison with the case of Eu-doped $LaPO_4$, the major Cm species is supposed to be on a La site of $LaPO_4$. The minor Cm species has a lifetime of 0.52 ms, and shows the presence of 0.4 waters in the first coordination sphere

of Cm. This is a similar value as for the minor Eu species. After thermal treatment, Cm within the Cm-doped $LaPO_4$ structure has a single Cm site, but shows four species, each one showing a four-fold splitting. The Cm environment of each four satellites is almost identical: similar degree of splitting, ratio of peak heights, proximity to each other, and an unique lifetime. As the unit cell of $LaPO_4$ is composed of four La atoms, the hypothesis suggested in this work is that a difference in the four La sites within a $LaPO_4$ unit cell exists. This would be a deviation from the ideal structure of La-monazite, which is shown by the four satellites of Cm.

The environment of Eu (III) within Eu-doped $LaPO_4$ sample was also analyzed with EXAFS. The first coordination sphere was modeled as three oxygen shells (N_{O1} = 4 at *r*(Eu-O1) = 2.37 Å, N_{O2} = 4 at *r*(Eu-O2) = 2.53 Å, and N_{O3} = 1.5 at *r*(Eu-O3) = 2.83 Å). Thus, the fit suggests the presence of 9.5 oxygen atoms surrounding Eu (III). The distances between Eu and the oxygen atoms determined in this work are in good agreement with the La-O distances described in the literature. The 9.5 oxygen atoms in the first coordination sphere are within the measurement uncertainties similar to 9.0. Europium is 9-fold coordinated by oxygen atoms, thus showing that Eu is incorporated in the La-monazite matrix at a La site. This result is consistent with the conclusion gained from the TRLFS measurements, i.e. that the Eu species incorporate on the La site.

In the second chapter (4.2), physical and thermal properties of monazite pellets were described, such as green and sintering densities, Vickers microhardness, fracture toughness, and dilatometric behavior. The optimal pressure (P_{opt}) corresponds to the maximal density achieved and is obtained via the study of compressibility and sinterability. The maximal relative sintering density is 98.0 % and it is reached for pellets made of powder calcined at 500 °C and pressed at 472 MPa. The average fracture toughness values are between 1.25 and 1.38 $MPa \cdot m^{0.5}$, while it is approx. 0.75 to 0.82 $MPa \cdot m^{0.5}$ for borosilicate glasses. Therefore, the crystalline phase La-monazite has a higher ability to resist to fracture than borosilicate glass, which is currently used as matrix for fission products. Dilatometric measurements enabled to analyze the sintering behavior of pellets made of powder calcined at 350 °C, 500 °C, and 950 °C. The initial, intermediate, and final stages of the densification takes place at 980-1155 °C, 1155-

1370 °C, and 1370-1400 °C, with an increase of the density of 60-67 %, 67-93 %, and 93-96 % respectively. The intermediate stage corresponds to the end of the residual OH-groups elimination and to the start of a stable sintering.

In the third chapter (4.3), the resistance to corrosion and to irradiation of sintered monazite-type samples was tested. New static aqueous durability experiments on five compositions of Eu-doped $LaPO_4$ were realized in an acidic media at 90 °C (section 4.3.1). The normalized dissolution rates determined in this work are in good agreement with values of synthetic and natural monazites of different compositions described in the literature. The normalized dissolution rate R_L (La) ($5.00 \cdot 10^{-5}$ g·m^{-2}·d^{-1}) is of the same order of magnitude of R_L (Ce) ($1.33 \cdot 10^{-5}$ g·m^{-2}·d^{-1}) in natural monazite, taking into account that the experiments of the natural analogue were realized at slightly lower temperature (70 °C). R_L (Eu) ($1.58 \cdot 10^{-4}$ g·m^{-2}·d^{-1}) is of the same order of magnitude of the approximated value R_L (Gd) ($2.6 \cdot 10^{-4}$ g·m^{-2}·d^{-1}), both values were measured in the same conditions. The ion radius might have an impact on its dissolution rate within the monazite host matrices. This assumption requires to be verified with further experiments. Furthermore, the normalized dissolution rates of La and Eu within monazite-type ceramics are lower than that of B, Na, Cs and Sr in glasses (approx. $4 \cdot 10^{-3}$ g·m^{-2}·d^{-1}), although the experimental conditions were weaker since the experiment was realized in deionized water at room temperature. Therefore synthetic monazite can be considered as a host phase superior to amorphous material such as borosilicate and phosphate glasses, due to its low aqueous dissolution rate. The realization of dynamic tests instead of static tests would inhibit the achievement of the thermodynamic equilibrium. This could permit the achievement of normalized dissolution rate for Eu within Eu-doped $LaPO_4$ for an Eu content above 20 mol%.

Host matrices for MA must also resist to self-irradiation. The structural damages created by the self-irradiation are mainly due to the alpha recoil. In order to recreate the damages at a laboratory scale, the inner irradiation is simulated by means of external bombardment of the matrix with ions. In this experiment, the recoil of the alpha particle is simulated with implantation of Kr^{2+} ions (section 4.3.2). Three La-monazite pellets were bombarded with Kr^{2+} ions (400 keV) at a fluence of 10^{12} to 10^{14} ions·cm^{-2}, and were

measured by Raman before and after the implantation. No amorphization was observed after the irradiation, thus confirming that $LaPO_4$ is not metamict under these experimental conditions.

Natural lanthanide orthophosphates ($REPO_4$) show the properties that are required for an excellent MA host matrix. These minerals are chemically durable regarding to aqueous alteration processes, and are chemically flexible. Furthermore, they can incorporate an important percentage of actinides, and they are resistant to radiation damage. These promising characteristics were found again in the La-monazite-type ceramics doped with actinide surrogates that were synthesized in this work, thus proving the potential of this candidate as host phase for the conditioning of MA. It confirms that the “monazite route” can be trusted, and further experiments should now be realized on monazite-type ceramics doped with a higher percentage of actinides.

References

[1] J. P. Holdren, "World Energy Council", Blog of "Women in science and engineering", Carleton University (11.2010).

[2] J.-M. Montel, "Minerals and design of new waste forms for conditioning nuclear waste" *Comptes Rendus Geoscience*, **343**[2-3] 230-36 (2011).

[3] W. J. Weber, A. Navrotsky, S. Stefanovsky, E. R. Vance, and E. Vernaz, "Materials Science of High-Level Nuclear Waste Immobilization" *Mrs Bulletin*, **34**[1] 46-53 (2009).

[4] B. I. Omel'yanenko, T. S. Livshits, S. V. Yudintsev, and B. S. Nikonov, "Natural and artificial minerals as matrices for immobilization of actinides" *Geol. Ore Depos.*, **49**[3] 173-93 (2007).

[5] World Nuclear Association, "Radioactive Waste Management - Public Information Service" www.world-nuclear.org/info/inf04.html (2011).

[6] Umweltbundesamt für Mensch und Umwelt, "Behandlung radioaktiver Abfälle und abgebrannter Brennelemente" www.umweltbundesamt-daten-zur-umwelt.de/umweltdaten/public/theme.do?nodeIdent=2316 (Juli 2011).

[7] M. Volkmer, "Kernenergie Basiswissen", I. Kernenergie, (2007)

[8] G. R. Lumpkin, "Ceramic waste forms for actinides" *Elements*, **2**[6] 365-72 (2006).

[9] E. H. Oelkers, and J. M. Montel, "Phosphates and nuclear waste storage" *Elements*, **4**[2] 113-16 (2008).

[10] O. Terra, N. Dacheux, F. Audubert, and R. Podor, "Immobilization of tetravalent actinides in phosphate ceramics" *Journal of Nuclear Materials*, **352**[1-3] 224-32 (2006).

[11] N. Dacheux, N. Clavier, A. C. Robisson, O. Terra, F. Audubert, J. E. Lartigue, and C. Guy, "Immobilisation of actinides in phosphate matrices" *C. R. Chim.*, **7**[12] 1141-52 (2004).

[12] IAEA, "Nuclear Fuel Cycle", IAEA Topical Booklets and Overviews, Science & Technology (2011).

[13] D. Barrier, "Characterisation and fabrication of zirconia and thoria based ceramics for nuclear applications", Fakultät für Georessourcen und Materialtechnik, Rheinisch -Westfälischen Technischen Hochschule Aachen (2005).

[14] I. Hore-Lacy, "Nuclear Energy in the 21st Century" (2006).

[15] NEA, "Nuclear Energy Outlook 2008" (2008).

[16] OECD NEA, "Actinide and Fission Product Partitioning and Transmutation, Annex E", (1999).

[17] G. Modolo, "Actinide(III) Recovery from High Active Waste Solutions Using Innovative Partitioning Processes" pp. 89-105. in Nuclear Energy and the Environment, **Vol. 1046.** *ACS Symposium Series.* Edited by C. M. Wai and B. J. Mincher. Amer Chemical Soc, Washington (2010).

[18] G. R. Choppin, "Solvent extraction processes in the nuclear fuel cycle" *Solvent Extraction Research and Development-Japan*, **12** 1-10 (2005).

[19] H. H. Anderson, and L. B. Asprey, "Solvent extraction process for plutonium" United States Patent Office, Edited by United States Atomic Energy Commission, USA (1960).

[20] B. Christiansen, C. Apostolidis, R. Carlos, O. Courson, J. P. Glatz, R. Malmbeck, G. Pagliosa, K. Romer, and D. Serrano-Purroy, "Advanced aqueous reprocessing in P&T strategies: Process demonstrations on genuine fuels and targets" *Radiochimica Acta*, **92**[8] 475-80 (2004).
[21] J. Magill, V. Berthou, D. Haas, J. Galy, R. Schenkel, H.-W. Wiese, G. Heusener, J. Tommasi, and G. Youinou, *Nuclear Energy*, **42**[5, Oct.] 263–77 (2003).
[22] B. Thomauske, R. Nabbi, P. Bourauel, K. Biß, N. Shetty, J. Kettler, S. Backus, M. Heuters, M. Hünefeld, M. Rossbach, G. Modolo, E. Mauerhofer, K. Bongardt, R. Maier, F. Esser, J. Wolters, S. Hamzic, N. Kolev, A. Wank, H. Koopman, B. Mertkaya, S. Ionova, M. Meister, H. Cura, A. Zimmer, R. Nies, B. Heidowitzsch, I. Mishustin, I. Pshenichnov, and W. Greiner, "Concept for an Advanced Gas-Cooled Accelerator-Driven Transmutation Experiment – AGATE", J. Kettler and M. Heuters (2012).
[23] IAEA, "Implications of Partitioning and Transmutation in Radioactive Waste Management", Technical Reports Series No.435 (2004).
[24] D. Bosbach, "Preface" *Journal of Contaminant Hydrology*, **102**[3–4] 173 (2008).
[25] OECD NEA, "Post-closure safety case for geological repositories", Radioactive waste management (2004).
[26] Ö. Yildiz, G. Modolo, and R. Telle, "Compactibility and sintering behavior of nanocrystalline $(Th_{1-x}Ce_x)O_2$ powders synthesized by co-precipitation process" *Journal of Nuclear Materials*, **377**[2] 396-400 (2008).
[27] X. Deschanels, V. Picot, B. Glorieux, F. Jorion, S. Peuget, D. Roudil, C. Jégou, V. Broudic, J. N. Cachia, T. Advocat, C. Den Auwer, C. Fillet, J. P. Coutures, C. Hennig, and A. Scheinost, "Plutonium incorporation in phosphate and titanate ceramics for minor actinide containment" *Journal of Nuclear Materials*, **352**[1-3] 233-40 (2006).
[28] R. C. Ewing, "Ceramic matrices for plutonium disposition" *Progress in Nuclear Energy*, **49**[8] 635-43 (2007).
[29] E. M. Pierce, B. P. McGrail, P. F. Martin, J. Marra, B. W. Arey, and K. N. Geiszler, "Accelerated weathering of high-level and plutonium-bearing lanthanide borosilicate waste glasses under hydraulically unsaturated conditions" *Appl. Geochem.*, **22**[9] 1841-59 (2007).
[30] W. J. Weber, R. C. Ewing, C. R. A. Catlow, T. D. de la Rubia, L. W. Hobbs, C. Kinoshita, H. Matzke, A. T. Motta, M. Nastasi, E. K. H. Salje, E. R. Vance, and S. J. Zinkle, "Radiation effects in crystalline ceramics for the immobilization of high-level nuclear waste and plutonium" *J. Mater. Res.*, **13**[6] 1434-84 (1998).
[31] Y. J. Zhang, and E. R. Vance, "Plutonium in monazite and brabantite: Diffuse reflectance spectroscopy study" *Journal of Nuclear Materials*, **375**[3] 311-14 (2008).
[32] I. W. Donald, B. L. Metcalfe, and R. N. J. Taylor, "The immobilization of high level radioactive wastes using ceramics and glasses" *Journal of Materials Science*, **32**[22] 5851-87 (1997).
[33] C. Lopez, X. Deschanels, J. M. Bart, J. M. Boubals, C. Den Auwer, and E. Simoni, "Solubility of actinide surrogates in nuclear glasses" *Journal of Nuclear Materials*, **312**[1] 76-80 (2003).

[34] K. Joseph, R. Asuvathraman, R. Raja Madhavan, H. Jena, K. V. Govindan Kutty, and P. R. Vasudeva Rao, "Studies on novel matrices for high level waste from fast reactor fuel reprocessing," pp. 518-24. **Vol. 7**, *2nd International Conference on Asian Nuclear Prospects, ANUP 2010*.

[35] B. Glorieux, M. Matecki, F. Fayon, J. P. Coutures, S. Palau, A. Douy, and G. Peraudeau, "Study of lanthanum orthophosphates polymorphism, in view of actinide conditioning" *Journal of Nuclear Materials*, **326**[2-3] 156-62 (2004).

[36] G. R. Lumpkin, K. L. Smith, R. Gieré, and C. T. Williams, "Geochemical behaviour of host phases for actinides and fission products in crystalline ceramic nuclear waste forms" *Geological Society, London, Special Publications*, **236**[1] 89-111 (2004).

[37] J.-M. Montel, B. Glorieux, A.-M. Seydoux-Guillaume, and R. Wirth, "Synthesis and sintering of a monazite-brabantite solid solution ceramic for nuclear waste storage" *Journal of Physics and Chemistry of Solids*, **67**[12] 2489-500 (2006).

[38] D. M. Strachan, R. D. Scheele, E. C. Buck, J. P. Icenhower, A. E. Kozelisky, R. L. Sell, R. J. Elovich, and W. C. Buchmiller, "Radiation damage effects in candidate titanates for Pu disposition: Pyrochlore" *Journal of Nuclear Materials*, **345**[2-3] 109-35 (2005).

[39] N. Dacheux, N. Clavier, and J. Ritt, "Behavior of thorium-uranium(IV) phosphate-diphosphate sintered samples during leaching tests. Part I - Kinetic study" *Journal of Nuclear Materials*, **349**[3] 291-303 (2006).

[40] ASTM International, "C1220-98 Standard test method for static leaching of monolithic waste forms for disposal of radioactive waste" (2004).

[41] E. H. Oelkers, and F. Poitrasson, "An experimental study of the dissolution stoichiometry and rates of a natural monazite as a function of temperature from 50 to 230 °C and pH from 1.5 to 10" *Chemical Geology*, **191**[1-3] 73-87 (2002).

[42] O. Terra, N. Clavier, N. Dacheux, and R. Podor, "Preparation and characterization of lanthanum-gadolinium monazites as ceramics for radioactive waste storage" *New Journal of Chemistry*, **27**[6] 957-67 (2003).

[43] B. E. Burakov, M. A. Yagovkina, V. M. Garbuzov, A. A. Kitsay, and V. A. Zirlin, "Self-irradiation of monazite ceramics: Contrasting behavior of $PuPO_4$ and $(La,Pu)PO_4$ doped with Pu-238" pp. 219-24. in Scientific Basis for Nuclear Waste Management XXVIII, **Vol. 824.** *Materials Research Society Symposium Proceedings.* Edited by J. M. Hanchar, S. StroesGascoyne, andL. Browning. Materials Research Society, Warrendale (2004).

[44] L. Nasdala, R. Grotzschel, S. Probst, and B. Bleisteiner, "Irradiation damage in monazite-(Ce): an example to establish the limits of Raman confocality and depth resolution" *Canadian Mineralogist*, **48**[2] 351-59 (2010).

[45] V. Picot, X. Deschanels, S. Peuget, B. Glorieux, A. M. Seydoux-Guillaume, and R. Wirth, "Ion beam radiation effects in monazite" *Journal of Nuclear Materials*, **381**[3] 290-96 (2008).

[46] A. Meldrum, L. A. Boatner, and R. C. Ewing, "A comparison of radiation effects in crystalline ABO(4)-type phosphates and silicates" *Mineralogical Magazine*, **64**[2] 185-94 (2000).

[47] A. Meldrum, L. A. Boatner, W. J. Weber, and R. C. Ewing, "Radiation damage in zircon and monazite" *Geochimica et Cosmochimica Acta*, **62**[14] 2509-20 (1998).

[48] F. G. Karioris, K. A. Gowda, and L. Cartz, "Heavy-ion bombardment of monoclinic $ThSiO_4$, ThO_2 and monazite" *Radiation Effects Letters*, **58**[1-2] 1-3 (1981).
[49] I. Farnan, H. Cho, and W. J. Weber, "Quantification of actinide alpha-radiation damage in minerals and ceramics" *Nature*, **445**[7124] 190-93 (2007).
[50] A. Meldrum, L. A. Boatner, and R. C. Ewing, "Displacive radiation effects in the monazite- and zircon-structure orthophosphates" *Physical Review B*, **56**[21] 13805-14 (1997).
[51] J. Lian, S. V. Yudintsev, S. V. Stefanovsky, L. M. Wang, and R. C. Ewing, "Ion beam irradiation of U-, Th- and Ce-doped pyrochlores" *Journal of Alloys and Compounds*, **444** 429-33 (2007).
[52] F. H. Spedding, "Historical Introduction to the Rare Earths". in The Rare Earths**.** Edited by F. H. Spedding and A. H. Daane. John Wiley & Sons, Inc., USA (1961).
[53] A. F. Holleman, and N. Wiberg, "Lehrbuch der Anorganischen Chemie" (1995).
[54] E. Riedel, "Anorganische Chemie" 6. Auflage ed. Walter de Gruyter GmbH & Co. (2004).
[55] F. H. Spedding, "The Chemistry of Rare Earths". in The Rare Earths**.** Edited by F. H. Spedding and A. H. Daane. John Wiley & Sons, Inc., USA (1961).
[56] Y. Q. Jia, "Crystal radii and effective ionic radii of the rare earth ions" *Journal of Solid State Chemistry*, **95** 184-87 (1991).
[57] P. Belli, R. Bernabei, F. Cappella, R. Cerulli, C. J. Dai, F. A. Danevich, A. d'Angelo, A. Incicchitti, V. V. Kobychev, S. S. Nagorny, S. Nisi, F. Nozzoli, D. Prosperi, V. I. Tretyak, and S. S. Yurchenko, "Search for α decay of natural Europium" *Nuclear Physics A*, **789**[1-4] 15-29 (2007).
[58] Gregg J. Lumetta, Major C. Thompson, Robert A. Penneman, and P. G. Eller, "The chemistry of the actinide and transactinide elements - Curium″ Third ed. Vol. 3 (2006).
[59] G. R. Choppin, and D. R. Peterman, "Applications of lanthanide luminescence spectroscopy to solution studies of coordination chemistry" *Coordination Chemistry Reviews*, **174**[1] 283-99 (1998).
[60] M. Schmidt, "Untersuchungen zum Einbaumechanismus von Actiniden und Lanthaniden in Calcium-haltige Sekundärphasen", Naturwissenschaftlich-Mathematischen Gesamtfakultät, Ruprecht-Karls-Universität, Heidelberg (2009).
[61] J. R. Lakowicz, "Principles of Fluorescence Spectroscopy″ Vol. 2. Kluwer Academic / Plenum Publishers: New York, NY, USA (1999).
[62] M. d. S. Marques Fernandes, "Spektroskopische Untersuchungen (TRLFS und XAFS) zur Wechselwirkung von dreiwertigen Lanthaniden und Actiniden mit der Mineralphase Calcit", Naturwissenschaftlich-Mathematischen Gesamtfakultät, Ruprecht-Karls-Universität, Heidelberg (2006).
[63] J. R. Albani, "Principles and Applications of Fluorescence Spectroscopy″: Oxford, UK (2007).
[64] L. Nasdala, J. Götze, J. M. Hanchar, M. Gaft, and M. R. Krbetschek, "Luminescence techniques in Earth Sciences". in Spectroscopic Methods in Mineralogy, **Vol. 6.** Edited by A. Beran and E. Libowitzky, Budapest, Hungary (2004).

[65] N. M. Edelstein, R. Klenze, T. Fanghanel, and S. Hubert, "Optical properties of Cm(III) in crystals and solutions and their application to Cm(III) speciation" *Coordination Chemistry Reviews*, **250**[7-8] 948-73 (2006).
[66] T. Stumpf, "Möglichkeiten zur Anwendung der TRLFS bei geochemischen Fragestellungen", KIT, Institut für Nukleare Entsorgung, Karlsruhe (2008).
[67] T. Stumpf, and T. Fanghanel, "A time-resolved laser fluorescence spectroscopy (TRLFS) study of the interaction of trivalent actinides (Cm(Ill)) with calcite" *Journal of Colloid and Interface Science*, **249**[1] 119-22 (2002).
[68] J.-C. G. Beunzli, and G. R. Choppin, "Lanthanide probes in life, chemical, and earth sciences ". Elsevier: Amsterdam, New York (1989).
[69] W. D. Horrocks, and D. R. Sudnick, "Lanthanide ion probes of structure in biology - laser-induced luminescence decay constants provide a direct measure of the number of metal-coordinated water-molecules" *Journal of the American Chemical Society*, **101**[2] 334-40 (1979).
[70] T. Kimura, and G. Choppin, "Luminescence study on determination of the hydration number of Cm (III)" *Journal of Alloys and Compounds*, **213** 313-17 (1994).
[71] A. Breithaupt, "Neue krystallographische Bestimmung und mineralogische Charakteristik verschiedener Mineralspecien, pp 296-306". in Journal für Chemie und Physik**.** Edited by D. F. W. Schweigger-Seidel, (1829).
[72] S. Jaulmes, "Affinement de la structure $LaPO_4$" *Bulletin de la Société française de minéralogie et de cristallographie*, **95**[1] 42 (1972).
[73] C. M. Gramaccioli, and T. V. Segalstad, "Uranium-rich and thorium-rich monazite from a south-alpine pegmatite at Piona, Italy" *Am. Miner.*, **63**[7-8] 757-61 (1978).
[74] C. Klein, and B. Dutrow, "Manual of mineral science" 23rd ed.: New York, NY, USA (2008).
[75] J. Kropiwnicka, and T. Znamierowska, "Phase-equilibria in the system La_2O_3-Na_2O-P_2O_5: 1. Side system La_2O_3-P_2O_5" *Pol. J. Chem.*, **62**[7-12] 587-94 (1988).
[76] Y. Hikichi, and T. Nomura, "Melting temperatures of monazite and xenotime" *Journal of the American Ceramic Society*, **70**[10] C252-C53 (1987).
[77] P. Boch, "Matériaux et processus céramiques" (2001).
[78] K. Toyoura, N. Hatada, Y. Nose, T. Uda, and I. Tanaka, "First-principles thermodynamics of La_2O_3-P_2O_5 pseudobinary system" *Physical Review B*, **84**[18] (2011).
[79] J. Nriagu, P. Moore, and F. Betts, "Phosphate minerals". Springer: Berlin, NY, USA (1984).
[80] A. Kaiser, M. Lobert, and R. Telle, "Thermal stability of zircon ($ZrSiO_4$)" *Journal of the European Ceramic Society*, **28**[11] 2199-211 (2008).
[81] D. Bregiroux, F. Audubert, T. Charpentier, D. Sakellariou, and D. Bernache-Assollant, "Solid-state synthesis of monazite-type compounds LnPO(4) (Ln = La to Gd)" *Solid State Sciences*, **9**[5] 432-39 (2007).
[82] H. Meyssamy, K. Riwotzki, A. Kornowski, S. Naused, and M. Haase, "Wet-chemical synthesis of doped colloidal nanomaterials: Particles and fibers of $LaPO_4$: Eu, $LaPO_4$: Ce, and $LaPO_4$: Ce,Tb" *Advanced Materials*, **11**[10] 840 (1999).

[83] E. E. Boakye, P. Mogilevsky, and R. S. Hay, "Synthesis of nanosized spherical rhabdophane particles" *Journal of the American Ceramic Society,* **88**[10] 2740-46 (2005).
[84] Y. Guo, P. Woznicki, A. Barkatt, E. E. Saad, and I. G. Talmy, "Sol-gel snthesis of microcrystalline rare earth orthophosphates" *Journal of Material Research,* **11** (1996).
[85] D. Bregiroux, O. Terra, F. Audubert, N. Dacheux, V. Serin, R. Podor, and D. Bernache-Assollant, "Solid-state synthesis of monazite-type compounds containing tetravalent elements" *Inorganic Chemistry,* **46** 10372-82 (2007).
[86] C. Babelot, A. Guignard, M. Huger, C. Gault, T. Chotard, T. Ota, and N. Adachi, "Preparation and thermomechanical characterisation of aluminum titanate flexible ceramics" *Journal of Materials Science,* **46**[5] 1211-19 (2011).
[87] L. Eadie, and T. K. Ghosh, "Biomimicry in textiles: past, present and potential. An overview" *J. R. Soc. Interface,* **8**[59] 761-75 (2011).
[88] F. A. Scorza, and E. A. Cavalheiro, "Biomimicry: Applying design for nature to solve problems in epilepsy research" *Epilepsy & Behavior,* **18**[3] 327-28 (2010).
[89] A. M. Seydoux-Guillaume, R. Wirth, L. Nasdala, M. Gottschalk, J. M. Montel, and W. Heinrich, "An XRD, TEM and Raman study of experimentally annealed natural monazite" *Phys. Chem. Miner.,* **29**[4] 240-53 (2002).
[90] B. Rasmussen, I. R. Fletcher, and J. R. Muhling, "In situ U–Pb dating and element mapping of three generations of monazite: Unravelling cryptic tectonothermal events in low-grade terranes" *Geochimica et Cosmochimica Acta,* **71**[3] 670-90 (2007).
[91] D. Munz, and T. Fett, "Ceramics: mechanical properties, failure behaviour, materials selection". Springer: Heidelberg, Germany (1999).
[92] P. E. D. Morgan, and D. B. Marshall, "Ceramic composites of Monazite and Alumina" *Journal of the American Ceramic Society,* **78**[9] 2574-74 (1995).
[93] Alan A. Coelho, "Topas Academic", version 4.1, Brisbane, Australia (2007).
[94] J.-F. Bérar, and P. Lelann, "E.S.D.'s and Estimated Probable Error Obtained in Rietveld Refinements with Local Correlations" *J. Appl. Cryst.,* **24** (1991).
[95] G. K. Williamson, and W. H. Hall, "X-ray line broadening from filed aluminium and wolfram" *Acta Metallurgica,* **1**[1] 22-31 (1953).
[96] Princeton Instruments, "Raman Spectroscopy Basics" www.piacton.com.
[97] D. Lance, F. Valdivieso, and P. Goeuriot, "Correlation between densification rate and microstructural evolution for pure alpha alumina" *Journal of the European Ceramic Society,* **24**[9] 2749-61 (2004).
[98] K. Rozov, Personal communication, Forschungszentrum Jülich GmbH (2011).
[99] E. Osthols, and M. Malmstrom, "Dissolution kinetics of ThO_2 in acid and carbonate media" *Radiochimica Acta,* **68**[2] 113-19 (1995).
[100] N. Dacheux, E. Du Fou de Kerdaniel, N. Clavier, R. Podor, J. Aupiais, and S. Szenknect, "Kinetics of dissolution of thorium and uranium doped britholite ceramics" *Journal of Nuclear Materials,* **404**[1] 33-43 (2010).
[101] E. Hillen-Maske, "Römpp Chemie Lexikon, 9. Auflage". Georg Thieme Verlag (1990).

[102] L. Galoisy, "X-ray absorption spectroscopy in geosciences: Information from the EXAFS region". in Spectroscopic Methods in Mineralogy, **Vol. 6.** Edited by A. Beran and E. Libowitzky, Budapest, Hungary (2004).
[103] Synchrotron facility ANKA at the Karlsruhe Institute of Technology (KIT), Hermann-von-Helmholtz-Platz 1, 76344 Eggenstein-Leopoldshafen (Germany).
[104] European Synchrotron Radiation Facility (ESRF), 6 rue Jules Horowitz, BP 220, 38043 Grenoble Cedex 9 (France).
[105] K. Dardenne, B. Brendebach, M. A. Denecke, X. Liu, J. Rothe, and T. Vitova, "New developments at the INE-Beamline for Actinide Research at ANKA". in 14th International Conference on X-Ray Absorption Fine Structure, **Vol. 190.** *Journal of Physics Conference Series.* Edited by A. DiCicco and A. Filipponi. Iop Publishing Ltd, Bristol (2009).
[106] B. Ravel, and M. Newville, "Athena, Artemis, Hephaestus: data analysis for X-ray absorption spectroscopy using IFEFFIT" *J. Synchrotron Rad.* , **12** 537-41 (2005).
[107] A. L. Ankudinov, B. Ravel, J. J. Rehr, and S. D. Conradson, "Real-space multiple-scattering calculation and interpretation of x-ray-absorption near-edge structure" *Physical Review B,* **58**[12] 7565-76 (1998).
[108] R. G. Jonasson, and E. R. Vance, "DTA study of the rhabdophane to monazite transformation in rare-earth (La-Dy) phosphates" *Thermochimica Acta,* **108** 65-72 (1986).
[109] S. Lucas, E. Champion, C. Penot, G. Leroy, and D. Bernache-Assollant, "Synthesis and characterization of rare earth phosphate powders" *Euro Ceramics Vii, Pt 1-3,* **206-2** 47-50 (2002).
[110] S. Lucas, E. Champion, D. Bernache-Assollant, and G. Leroy, "Rare earth phosphate powders $RePO_4 \cdot nH_2O$ (Re = La, Ce or Y) II. Thermal behavior" *Journal of Solid State Chemistry,* **177**[4-5] 1312-20 (2004).
[111] I. Brusset, F. Leveau, P. Spinat, A. Trani, and J. Verollet, "Le nitrate d'ammonium, description, production, utilisations et précautions d'usage", M. Delmas and J.-L. Lacout, (2002)
[112] H. D. Park, and E. R. Kreidler, "Phase-equilibria in the system La_2O_3-P_2O_5" *Journal of the American Ceramic Society,* **67**[1] 23-26 (1984).
[113] Y. X. Ni, J. M. Hughes, and A. N. Mariano, "Crystal-chemistry of the monazite and xenotime structures" *Am. Miner.,* **80**[1-2] 21-26 (1995).
[114] N. Niu, P. Yang, Y. Wang, W. Wang, F. He, S. Gai, and D. Wang, "$LaPO_4$:Eu^{3+}, $LaPO_4$:Ce^{3+}, and $LaPO_4$:Ce^{3+},Tb^{3+} nanocrystals: Oleic acid assisted solvothermal synthesis, characterization, and luminescent properties" *Journal of Alloys and Compounds,* **509**[6] 3096-102 (2011).
[115] K. S. Holliday, C. Babelot, C. Walther, S. Neumeier, D. Bosbach, and T. Stumpf, "Site-selective time resolved laser fluorescence spectroscopy of Eu and Cm doped $LaPO_4$" *Radiochimica Acta,* **100**[3] 189-95 (2012).
[116] C. Görller-Walrand, and K. Binnemans, "Rationalization of crystal-field parametrization". in Handbook on the physics and chemistry of rare earths, **Vol. 23.** Edited by K. A. Gschneider Jr. and L. Eyring (1996).
[117] K. M. Murdoch, N. M. Edelstein, L. A. Boatner, and M. M. Abraham, "Excited state absorption and fluorescence in narrowing studies of Cm^{3+} in $LuPO_4$" *Journal of Chemical Physics,* **105**[7] 2539-46 (1996).

[118] D. Bregiroux, S. Lucas, E. Champion, F. Audubert, and D. Bernache-Assollant, "Sintering and microstructure of rare earth phosphate ceramics $REPO_4$ with RE = La, Ce or Y" *Journal of the European Ceramic Society,* **26**[3] 279-87 (2006).
[119] E. E. Underwood, A. R. Colcord, and R. C. Waugh, "Quantitative Relationships for Random Microstructures". in Ceramic Microstructures**.** Edited by R. M. Fulrath and J. A. Pask. John Wiley & Sons, Berkeley (1966).
[120] J. M. Zheng, W. B. Carlson, and J. S. Reed, "Dependence of compaction efficiency in dry pressing on the particle-size distribution" *Journal of the American Ceramic Society,* **78**[9] 2527-33 (1995).
[121] A. A. Bukaemskiy, D. Barrier, and G. Modolo, "Compressibility and sinterability of CeO_2-8YSZ powders synthesized by a wet chemical method" *Journal of the European Ceramic Society,* **29**[10] 1947-54 (2009).
[122] M. A. C. G. Van de Graaf, J. H. H. Ter Maat, and A. J. Burggraaf, "Microstructure and sintering kientics of highly reactive ZrO_2-$Y2O_3$ ceramics" *Journal of Materials Science,* **20** 1407-18 (1985).
[123] A. A. Bukaemskiy, Forschungszentrum Jülich GmbH, Germany.
[124] D. Bregiroux, « Synthèse par voie solide et frittage de céramiques à structure monazite - Application au conditionnement des actinides mineurs », Ecole Doctorale « Science, Technologie et Santé » ED n°258, Université de Limoges, Limoges (2005).
[125] M. Huger, « Propriétés mécaniques des céramiques », ENSCI, Limoges (2006).
[126] A. C. Thomas, N. Dacheux, P. Le Coustumer, V. Brandel, and M. Genet, "Kinetic and thermodynamic study of the thorium phosphate–diphosphate dissolution" *Journal of Nuclear Materials,* **281**[2–3] 91-105 (2000).
[127] N. Clavier, E. D. de Kerdaniel, N. Dacheux, P. Le Coustumer, R. Drot, J. Ravaux, and E. Simoni, "Behavior of thorium-uranium(IV) phosphate-diphosphate sintered samples during leaching tests. Part II. Saturation processes" *Journal of Nuclear Materials,* **349**[3] 304-16 (2006).
[128] N. Clavier, "Elaboration de Phosphate - Diphosphate de Thorium et d'Uranium (β-PDTU) et de matériaux composites β-PDTU/Monazite à partir de précurseurs cristallisés – Etudes du frittage et de la durabilité chimique", Université Paris XI Orsay, (2005).
[129] C. Tamain, N. Dacheux, F. Garrido, A. Habert, N. Barré, A. Özgümüs, and L. Thomé, "Consequences of the ion beam irradiation on the chemical durability of thorium phosphate diphosphate – kinetics study" *Journal of Nuclear Materials,* **358**[2-3] 190-201 (2006).
[130] Z. S. Cetiner, and Y. L. Xiong, "Chemical controls on the solubility, speciation and mobility of lanthanum at near surface conditions: A geochemical modeling study" *Appl. Geochem.,* **23**[8] 2301-15 (2008).
[131] W. E. Lee, M. I. Ojovan, M. C. Stennett, and N. C. Hyatt, "Immobilisation of radioactive waste in glasses, glass composite materials and ceramics" *Advances in Applied Ceramics* **105**[1] (2006).
[132] E. N. Silva, A. P. Ayala, I. Guedes, C. W. A. Paschoal, R. L. Moreira, C. K. Loong, and L. A. Boatner, "Vibrational spectra of monazite-type rare-earth orthophosphates" *Optical Materials,* **29**[2-3] 224-30 (2006).

[133] M. E. Poloznikova, and V. V. Fomichev, "The vibrational spectra and characteristic features of the orthophosphates of Group I-III elements" *Russ. Chem. Rev.*, **63** [5] (1994).
[134] G. M. Begun, G. W. Beall, L. A. Boatner, and W. J. Gregor, "Raman spectra of the rare earth orthophosphates" *Journal of Raman Spectroscopy*, **11**[4] 273-78 (1981).
[135] K. Nakamoto, "Infrared and Raman Spectra of Inorganic and Coordination Compounds". in Handbook of Vibrational Spectroscopy**.** John Wiley & Sons, Ltd, (2006).

Publications and presentations of this work

- Journal article

K. S. Holliday, **C. Babelot**, C. Walther, S. Neumeier, D. Bosbach, and T. Stumpf, "Site-selective time resolved laser fluorescence spectroscopy of Eu and Cm doped LaPO4," *Radiochimica Acta*, **100**[3] 189-95 (2012).

- Conference proceeding

C. Babelot, S. Neumeier, A. Bukaemskiy, G. Modolo, H. Schlenz and D. Bosbach, Conditioning of Minor Actinides in Monazite-type Ceramics, Actinide reCycling by SEParation and Transmutation, 1st International Workshop, Portugal, 2010.

- Poster presentations at conferences

C. Babelot, S. Neumeier, A. Bukaemskiy, G. Modolo, H. Schlenz and D. Bosbach, Conditioning of Minor Actinides in Monazite-type Ceramics, Actinide reCycling by SEParation and Transmutation, 1st International Workshop, Portugal, 2010.

C. Babelot, S. Neumeier, A. Bukaemskiy, G. Modolo and D. Bosbach, Conditioning of Minor Actinides in Monazite-type Ceramics, CIMTEC, 5th Forum on New Materials, Italy, 2010.

C. Babelot, A. Bukaemskiy, S. Neumeier, G. Modolo, D. Bosbach, K. Holliday and T. Stumpf, Conditioning of Minor Actinides in La-Monazite-type Ceramics, 494. WE-Heraeus-Seminar, "Innovative Nuclear Power in a Closed Fuel Cycle Scenario", Germany, 2011. Best poster award (2^{nd} place).

H. Schlenz, J. Heuser, St. Schmitz, **C. Babelot**, Raman spectra of Synthetic Orthophosphates used for Nuclear Waste Management, International Union of Crystallography, XXII Congress and General Assembly, Spain, 2011.

H. Schlenz, J. Heuser, St. Schmitz, **C. Babelot**, Raman spectra of Synthetic Orthophosphates used for Nuclear Waste Management, Crystals, Minerals and Materials, Austria, 2011.

- Oral presentation at conferences

C. Babelot, S. Neumeier, A. Bukaemskiy, G. Modolo, H. Schlenz, D. Bosbach, K. Holliday and T. Stumpf, Conditioning of Minor Actinides in La-Monazite-type Ceramics, Spring Meeting of the European Material Research Society, France, 2011.

S. Neumeier, **C. Babelot**, S. Finkeldei, T. Schuppik, A.A. Bukaemskiy, F. Brandt, H. Schlenz, G. Modolo and D. Bosbach, Conditioning of Minor Actinides in Monazite- and Pyrochlore-type Ceramics, Spring Meeting of the European Material Research Society, France, 2012.

Acknowledgements

This work is supported by the *Ministerium für Innovation, Wissenschaft, Forschung und Technologie (MIWFT) des Landes Nordrhein-Westfalen* (reference number: 323-005-0911-0129).

I would like to express my gratitude to Prof. Dr. Dirk Bosbach who gave me the opportunity to pursue my PhD at the Institute for Energy and Climate Research, Safety Research and Reactor Technology (IEK-6), at Forschungszentrum Jülich. Thank you for the supervision of my work and the numerous advices. I am grateful to Prof. Dr. Rainer Telle who accepted to evaluate my thesis and provided pertinent comments about my work. I am thankful to Prof. Dr. Georg Roth who was the president of the doctoral commission and who encouraged me not to be too stressed out before the D-Day.

Many thanks go to Dr. Giuseppe Modolo who welcomed me in his work group and guided me through my PhD thesis with many recommendations, especially during the long time of writing. I am indebted to Dr. Andrey Bukaemskiy who spent so many hours discussing results with me and worked with me in the laboratory. Thank you to Dr. Stefan Neumeier for enriching discussions.

During my PhD, I spent a lot of time in the lab, and got help from a lot of IEK-6 members. Special thanks go to Fabian Sadowski and Christian Schreinemachers for the ICP-MS mesasurements, Murat Güngör for the BET measurements, Tim Schuppik and Dr. Stefan Neumeier regarding the hydrothermal synthesis and the dissolution tests, Julia Heuser, Stephan Schmitz and Dr. Andreas Neumann for the X-ray diffraction measurements, Ralf König, Dr. Martina Klinkenberg for the time spent at the SEM, Dr. Andrey Bukaemskiy for the time he worked on the pellets, Dr. Giuseppe Modolo for the TG-DSC and dilatometry measurements, and Dr. Hartmut Schlenz for the Raman measurements.

The ion implantation of La-monazite samples was realized at the PGI-9 Institute. I want to thank Andre Dahmen, Dr. Bernd Holländer, and Dr. Dan Mihai Buca for their help and the nice cooperation.

I would like to thank Prof. Dr. Dirk Bosbach for encouraging me to spend several weeks at the Institute for Nuclear Waste Disposal (INE) in Karlsruhe in order to perform TRLFS and EXAFS measurements. Thank you very much to Dr. Kiel Holliday, Dr. Thorsten Stumpf, Dr. Kathy Dardenne, and Dr. Nicolas Finck for the friendly collaboration and the good work atmosphere. I hope to see you again!

I want to thank my office colleagues Dr. Andreas Neumann and Dr. Konstantin Rozov for their advices, their kindness, and their good mood. I shared my daily work with so many colleagues and I want to thank them for their help, their attention and/or for having proof-read my PhD thesis: Sarah Finkeldei, Jana Assenmacher, Julia Heuser, Fabian Sadowski, Christian Schreinemachers, Tim Schuppik, Steve Lange, Mark Weidenfeld, Elena Ebert, Sanela Omanovic, Karin Nöldgen, Yulia Arinicheva, Clemens Listner, Thomas Krings, Dr. Henrik Daniels, Dr. Michal Sypula, and Dr. Andreas Wilden.
Thank you to my friends from Studium Universale and from the Rurtalbahn. It was a lot of fun to talk with you, to have lunch together, and to meet you after work!

I would like to show my gratitude to my family, my in-laws, and my close friends for their continuous support during my studies. I especially thank my parents, Jean-François and Marie-Claude Babelot, as well as my brother and my sister who have always been there for me. All my thanks and love to my husband Dr. Alexandre Guignard who showed great listening faculties during these three years. Thank you to our son Matthieu who was already with me during the PhD defense. We hope that you are proud of us!

Extended abstract

The minor actinides (MA) neptunium, americium, and curium are mainly responsible for the long-term radiotoxicity of the High Active Waste (HAW) generated during the nuclear power operation. If these long-lived radionuclides are removed from the HAW by partitioning and converted by neutron fission (transmutation) into shorter-lived or stable elements, the remaining waste loses most of its long-term radiotoxicity. Thus, partitioning and transmutation (P&T) are considered as attractive options for reducing the burden on geological disposals. As an alternative, these separated MA can also be conditioned (P&C strategy) in specifically adapted ceramics to ensure their safe final disposal over long periods. At the moment, spent fuel elements are foreseen either for direct disposal in deep geological repositories or for reprocessing. The highly active liquid waste that is produced during reprocessing is conditioned industrially using a vitrification process before final disposal. Although the widely used borosilicate glasses meet most of the specifications needed, ceramic host matrices appear to be even more suitable in terms of resistance to corrosion. The development of new materials based on tailor-made highly specific ceramics with extremely stable behavior would make it possible to improve the final storage of long-lived high-level radiotoxic waste.

In the framework of this PhD research project, monazite-type ceramics were chosen as promising host matrices for the conditioning of trivalent actinides. The focus on the monazite-type ceramics is justified by their properties such as high chemical durability. *RE*PO_4 ceramics are named monazite for *RE* = La - Gd (monoclinic symmetry) and xenotime for *RE* = Tb - Lu and Y (tetragonal symmetry). The objective of this study is to contribute to the understanding of the alteration behavior of such ceramics under the repository conditions.

REPO_4 (with *RE* = La, Eu) is prepared by hydrothermal synthesis at 200°C. Structural and morphological characteristics (using X-ray diffraction (XRD) and scanning electron microscope (SEM)) combined with physical and thermal properties of samples (using thermogravimetry, differential scanning calorimetry (TG-DSC) and dilatometry) are realized in order to study the behavior of monazite-type powder and pellets.

The access to short-range-order spectroscopy (time resolved laser fluorescence spectroscopy (TRLFS) and extended X-ray absorption fine structure (EXAFS)) permits to

understand the structure of ceramic waste forms at the molecular level. La-monazite matrices being doped with Eu (III) (as a non-radioactive chemical homologue for Am (III)) and Cm (III), TRLFS is used to explore the local structural environment of Eu and Cm within the monazite crystal structure. Eu (III) and Cm (III) are substituted on the La site of $LaPO_4$. The single site of Cm (III) is found in four slightly different environments which is assumed to be due to a difference in the four La sites within a $LaPO_4$ unit cell. Structural parameters of the Eu (III) species were also analyzed by EXAFS. The nearest neighbors of Eu (III) are modeled as 9.5 oxygen atoms ($N_{O1} = 4$ at r(Eu-O1) = 2.37 Å, $N_{O2} = 4$ at r(Eu-O2) = 2.53 Å, and $N_{O3} = 1.5$ at r(Eu-O3) = 2.83 Å).

An essential parameter that describes the stability of the host phases is their dissolution rate obtained under conditions of relevance for final repositories. In this context, a set-up is developed and tested on crushed pellets. Normalized weight losses of lanthanum-phosphates and europium-doped lanthanum-phosphates, measured in acidic media at 90 °C, are interpreted and compared against the previous findings from the literature. The normalized dissolution rate for La and Eu within (La, Eu)PO_4 is between $1 \cdot 10^{-5}$ and $1 \cdot 10^{-4}$ $g \cdot m^{-2} \cdot d^{-1}$, whereas the rate of Na, Cs and Sr in phosphate glass at room temperature in deionized water is about $1 \cdot 10^{-2}$ $g \cdot m^{-2} \cdot d^{-1}$. Another essential parameter is their resistance to radiation. The damage created by the recoils accompanying alpha-decay can be simulated on ceramic matrices. Preliminary experiments are realized by means of ion bombardment. Kr^{2+} ions are implanted in La-monazite-type pellets, and the effects on the $LaPO_4$ structure resulting from the Raman spectroscopy are poor.

On a laboratory scale, the promising characteristics of the monazite mineral are found again in the synthetic phosphate. In particular, the doping of actinide surrogates is successful and the corrosion tests under repository conditions show a good resistance of the samples. The results achieved in this work confirm that among other favorable ceramics (e.g. pyrochlore) the “monazite-route” has to be further pursued regarding the research on the conditioning of MA.

Zusammenfassung

Für die langfristige Radiotoxizität der hochradioaktiven Abfälle (HAW), die bei der Nutzung der Kernenergie anfallen, sind hauptsächlich die minoren Actinoiden (MA) Neptunium, Americium und Curium verantwortlich. Durch Partitionierung können diese langlebigen Radionuklide abgetrennt werden und durch neutroneninduzierte Kernspaltung (Transmutation) in kurzlebige oder stabile Elemente umgewandelt werden. Dies führt zu einer signifikanten Abnahme der Langzeitradiotoxizität des verbleibenden Abfalls. Partitionierung und Transmutation (P&T) wird als attraktives Konzept gesehen, um die Belastung der geologischen Endlagerung zu verringern. Alternativ können die abgetrennten MA auch in speziell angepassten Keramiken konditioniert werden (P&C Strategie), um deren sichere Endlagerung über lange Zeiträume zu gewährleisten. Vom momentanen Standpunkt aus können die abgetrennten Brennelemente entweder in der Wiederaufarbeitung eingesetzt werden oder in tiefen geologischen Formationen endlagert werden. Der bei der Wiederaufbereitung entstehende hochradioaktive flüssige Abfall, wird mit Hilfe eines Verglasungsprozesses vor der endgültigen Entsorgung industriell aufbereitet. Obwohl die weit verbreiteten Borosilikatgläser die meisten der erforderlichen Spezifikationen für die Endlagerung erfüllen, erscheinen keramische Matrizen im Hinblick auf die Beständigkeit gegen Korrosion besser geeignet zu sein. Die Entwicklung neuer Materialien basierend auf maßgeschneiderten hochspezifischen Keramiken mit extrem stabilen Eigenschaften würde es ermöglichen, die Endlagerung des langlebigen hochradiotoxischen Abfalls zu verbessern.

Im Rahmen dieser Doktorarbeit wurden Keramiken mit der Monazit-Struktur als vielversprechende Wirtsphase für die Konditionierung von dreiwertigen Actinoiden gewählt. Die Fokussierung auf die Keramik des Monazit-Typs ist auf Grund ihrer Eigenschaften wie der hohen chemischen Beständigkeit gerechtfertigt. *RE*PO_4 Keramiken mit *RE* = La - Gd werden als Monazite (monokline Symmetrie) bezeichnet, wohingegen Systeme mit *RE* = Tb - Lu und Y als Xenotim (tetragonale Symmetrie) bezeichnet werden. Das Ziel dieser Arbeit ist es, einen Beitrag zum Verständnis der Veränderung dieser Keramiken unter endlagerrelevanten Bedingungen zu leisten.

REPO_4 (mit *RE* = La, Eu) wird bei 200 °C über eine Hydrothermalsynthese hergestellt. Strukturelle und morphologische Eigenschaften (mit Röntgenbeugung und

Rasterelektronenmikroskop (REM)) kombiniert mit physikalischen und thermischen Eigenschaften der Proben (Thermogravimetrie, dynamische Differenzkalorimetrie und Dilatometrie) werden untersucht, um das Verhalten der Monazitstruktur an Pulvern und Pellets zu analysieren.

Der Zugang zu Verfahren der Nahordnungsspektroskopie (zeitaufgelöste Laser-Fluoreszenzspektroskopie (TRLFS) und EXAFS-Spektroskopie (Extended X-ray Absorption Fine Structure)) ermöglicht eine Charakterisierung der keramischen Entsorgungsmatrizen auf einer molekularen Ebene. TRLFS wird verwendet, um die lokale strukturelle Umgebung von Eu (III) (als nicht-radioaktives chemisches Homolog zu Am (III)) und Cm (III) in der Kristallstruktur von dotierten La-Monazit Matrizen zu untersuchen. Eu (III) und Cm (III) substituieren La (III) in $LaPO_4$. Die einzige „Site“ von Cm (III) wird in vier leicht unterschiedlichen Umgebungen gefunden, was vermutlich durch vier verschiedene Positionen der La-„Sites“ innerhalb einer $LaPO_4$ Elementarzelle verursacht wird. Strukturparameter der Eu (III)-Spezies wurden durch EXAFS analysiert. Die nächsten Nachbarn von Eu (III) werden als 9,5 Sauerstoffatome modelliert ($N_{O1} = 4$ bei r(Eu-O1) = 2,37 Å, $N_{O2} = 4$ bei r(Eu-O2) = 2,53 Å und $N_{O3} = 1,5$ bei r(Eu-O3) = 2,83 Å).

Ein wesentlicher Parameter, der die Stabilität der Wirtsphase beschreibt, ist ihre Auflösungsgeschwindigkeit unter Endlager-Bedingungen. In diesem Zusammenhang wird ein Versuchsaufbau für Experimente an gemörserten Pellets entwickelt. Normalisierte Gewichtsverluste von Lanthan-Phosphaten und Europium-dotierten Lanthan-Phosphaten in saurem Medium bei 90 °C werden interpretiert und mit Ergebnissen aus der Literatur verglichen. Die normalisierte Auslaugrate für La und Eu innerhalb (La, Eu)PO_4 liegt zwischen $1 \cdot 10^{-5}$ und $1 \cdot 10^{-4}$ $g \cdot m^{-2} \cdot d^{-1}$, während die Rate von Na, Cs und Sr in Phosphat-Glas bei Raumtemperatur in deionisiertem Wasser etwa bei $1 \cdot 10^{-2}$ $g \cdot m^{-2} \cdot d^{-1}$ liegt. Ein weiterer essentieller Parameter ist ihre Resistenz gegenüber ionisierender Strahlung. Die Schäden, die durch einen den Alpha-Zerfall begleiteten Rückstoß entstehen, können für keramische Matrizen simuliert werden. Dazu werden vorläufige Experimente mittels Ionenbeschuss realisiert. Kr^{2+}-Ionen werden dabei in La-Monazit Pellets eingebettet. Anhand der Raman-Spektroskopie werden nur schwache Auswirkungen auf die $LaPO_4$ Struktur beobachtet.

Die vielversprechenden Eigenschaften des Minerals Monazit finden sich in dem synthetischen Phosphat wieder. Insbesondere ist die Dotierung der Keramiken mit Actinoiden Surrogaten erfolgreich durchgeführt worden und die Korrosionsprüfungen unter Endlager-Bedingungen zeigen eine gute Beständigkeit der Proben. Die Ergebnisse dieser Arbeit bestätigen, dass neben anderen geeigneten Keramiken (z.B.: Pyrochlor) die "Monazit-Route" in Bezug auf die Forschung über die Konditionierung von MA weiter verfolgt werden sollte.

Band / Volume 168
An analysis of the global atmospheric methane budget under different climates
A. Basu (2013), v, 110 pp
ISBN: 978-3-89336-859-4

Band / Volume 169
Experimental determination of the partitioning coefficient of nopinone as a marker substance in organic aerosol
B. Steitz (2013), 132 pp
ISBN: 978-3-89336-862-4

Band / Volume 170
Ion Beam Treatment of Functional Layers in Thin-Film Silicon Solar Cells
W. Zhang (2013), xi, 191 pp
ISBN: 978-3-89336-864-8

Band / Volume 171
Pulvermetallurgische Herstellung von porösem Titan und von NiTi-Legierungen für biomedizinische Anwendungen
M. Bram (2013), X, 238 pp
ISBN: 978-3-89336-866-2

Band / Volume 172
IEK-3 Report 2013. Langlebige Elektrochemische Verfahrenstechnik
(2013), ca. 185 pp
ISBN: 978-3-89336-868-6

Band / Volume 173
Combined Steady State and High Cycle Transient Heat Load Simulation with the Electron Beam Facility JUDITH 2
Th. Loewenhoff (2013), XVI, 108 pp
ISBN: 978-3-89336-869-3

Band / Volume 174
High-Quality Thorium TRISO Fuel Performance in HTGRs
K. Verfondern, H. Nabielek, M.J. Kania, H.-J. Allelein (2013), viii, 109 pp
ISBN: 978-3-89336-873-0

Band / Volume 175
Characterization of effective hydraulic properties of unsaturated porous media using spectral induced polarization (SIP)
K. Breede (2013), xiv, 72 pp
ISBN: 978-3-89336-875-4

Band / Volume 176
Zur Mikrostruktur siliziumbasierter Dünnschichten für die Photovoltaik
F. Köhler (2013), i, 100 pp
ISBN: 978-3-89336-876-1

Band / Volume 177
Grundlagen für die Transformation von Energiesystemen
Texte und Ergebnisse der Cadenabbia-Tagung 2012
der Konrad-Adenauer-Stiftung und des Forschungszentrum Jülich GmbH
L. Gruber, J.-F. Hake (Eds.) (2013), VI, 114 pp
ISBN: 978-3-89336-877-8

Band / Volume 178
Thermo - mechanical investigations and predictions
for oxygen transport membrane materials
G. Pećanac (2013), 143 pp
ISBN: 978-3-89336-878-5

Band / Volume 179
Thermomechanische Charakterisierung neu entwickelter Feuerfestwerkstoffe
E. Skiera (2013), III, 133 pp
ISBN: 978-3-89336-885-3

Band / Volume 180
Entwicklung und Herstellung von metallgestützten Festelektrolyt-Brennstoffzellen mit Hilfe des Hohlkathoden-Gasflusssputterns
M. Haydn (2013), XVI, 174 pp
ISBN: 978-3-89336-886-0

Band / Volume 181
Characterization and stability investigation of water dispersible colloids (WDCs) in natural soils
C. Jiang (2013), X, 102 pp
ISBN: 978-3-89336-887-7

Band / Volume 182
Monazite-type Ceramics for Conditioning of Minor Actinides: Structural Characterization and Properties
C. Babelot (2013), x, 129 pp
ISBN: 978-3-89336-889-1

Weitere ***Schriften des Verlags im Forschungszentrum Jülich*** unter
http://wwwzb1.fz-juelich.de/verlagextern1/index.asp

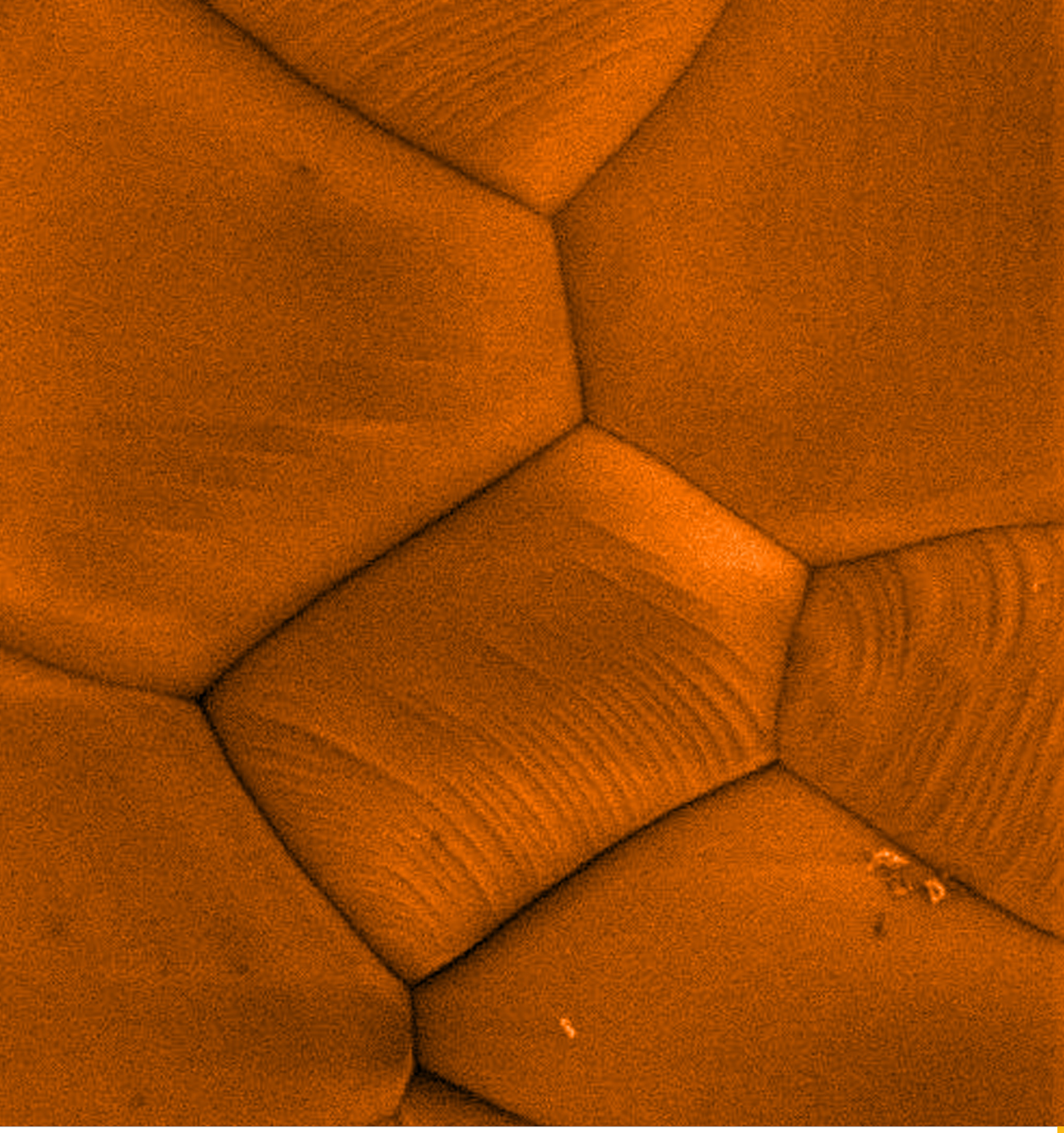

Energie & Umwelt / Energy & Environment
Band / Volume 182
ISBN 978-3-89336-889-1

JÜLICH
FORSCHUNGSZENTRUM